LLE Review

Quarterly Report

UR
LLE

UV pulses

— Simulated
--- Measured
····· UV template

Power (GW)

Time (ns)

Beamline near fields

Measured　　　　Simulated　　　(J/cm²)

UV

y (cm)

x (cm)　　　　x (cm)

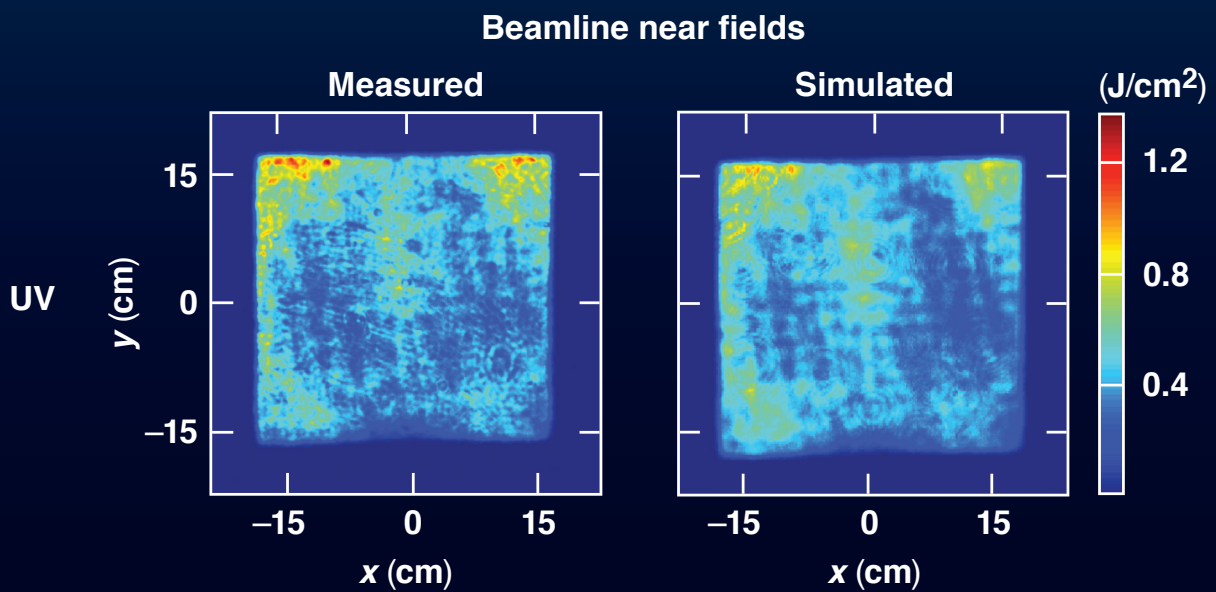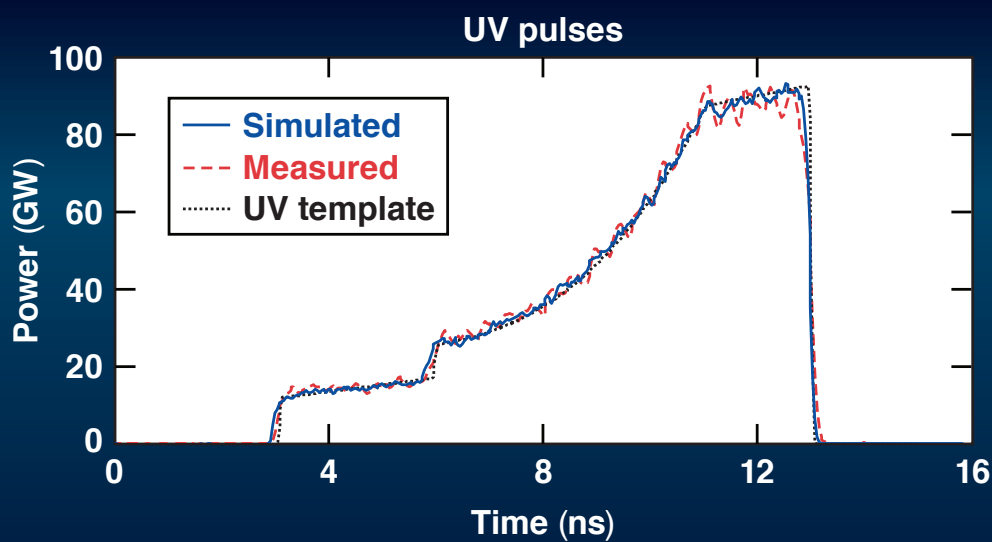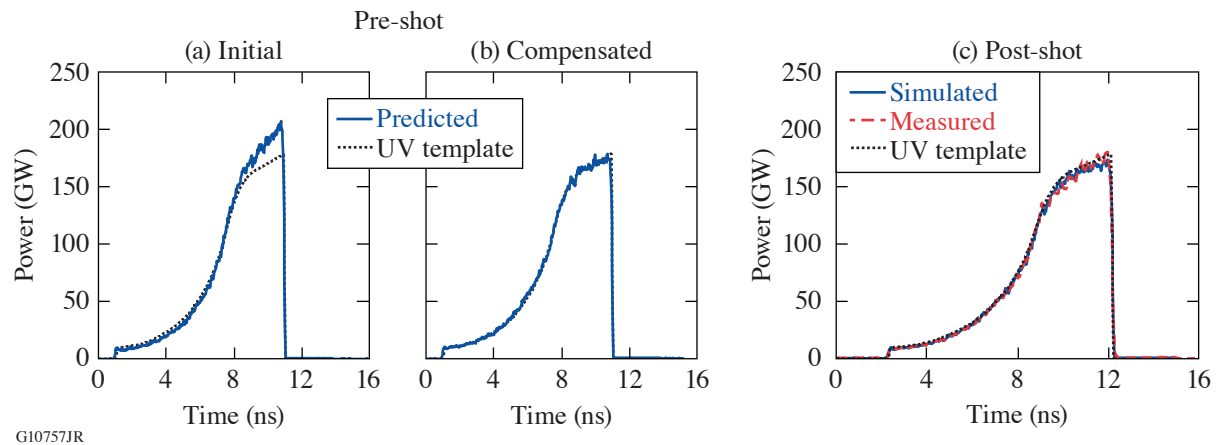## About the Cover:

The cover depicts a new predictive capability for the OMEGA EP Laser System. This is made possible by *PSOPS*, a MATLAB-based semi-analytic model, which takes as inputs numerous measurements along the amplifier chain and has enabled enhancements to the system as well as experimental flexibility to users (see p. 211). The top plot shows a *PSOPS*-simulated temporal pulse shape compared to the corresponding on-shot measured pulse and requested UV template shape. As well as predicting the temporal pulse shape, *PSOPS* also simulates the UV near-field spatial beam profile, which is shown on the bottom of the cover compared to the measured near-field profile. Both the temporal and spatial on-shot measurements are in excellent agreement with predictions by the *PSOPS* model. Overall, this enhanced predictive capability allows operations to account for system drifts and better deliver requested pulse shapes for valuable user experiments.

The figure below shows how *PSOPS* is used during shot preparations to adjust a pulse shape to match the requested UV shape. Drifts in system performance can lead to noticeable deviations between simulated and achieved pulse shapes. Panel (a) shows a shot day *PSOPS* pre-shot prediction that departs from the ideal shape near the end of the pulse. Based on this prediction, the input pulse shape was modified to provide the compensated pre-shot prediction shown in panel (b). The post-shot UV simulation showed excellent agreement with the measurement [panel (c)].

G10757JR

LLE Review

Quarterly Report

UR *
LLE

Contents

Pulsed-Power Systems

Education and Outreach

Laser Facility Report

Publications and Conference Presentations

In Brief

This volume of LLE Review 160, covering the period July–September 2019, is sectioned among research areas at LLE and external users of the Omega Laser Facility. Articles appearing in this volume are the principal summarized results of long-form research articles. Readers seeking a more-detailed account of research activities are invited to seek out the primary materials appearing in print, detailed in the publications and presentations section at the end of this volume.

Highlights of research presented in this volume include the following:

- A. R. Christopherson *et al*. derive an ignition criterion for inertial fusion implosions based on yield amplification from alpha-particle heating (p. 187). They also show that the criterion holds when compared to simulations that include hot-spot perturbations.

- L. Ceurvorst *et al*. present a hybrid target design that incorporates elements of both direct- and indirect-drive target designs for mitigating the Rayleigh–Taylor instability (p. 190). A planar experiment was completed to show that forming a pre-plasma with a thin, Au-lined CH that is offset from a thicker, CH planar target will reduce instabilities when the latter is shocked by a drive pulse.

- J. J. Ruby *et al*. describe two modifications to Guderley's solution to the converging shock problem to extend its utility: (1) the addition of an isentropic release wave and (2) fluid partitioning between an electron fluid and an ion fluid (p. 193). A comparison of the modified solution to *LILAC* simulations shows agreement over a broad range of solid CH sphere implosions.

- A. V. Maximov, J. G. Shaw, and J. P. Palastro detail a dynamic instability saturation mechanism, allowing for laser light to transmit through coronal plasma despite surpassing the threshold conditions for stimulated Raman scattering (SRS), as observed in planar experiments at the National Ignition Facility (NIF) (p. 195). This resulting enhanced transmission explains why models with no absolute SRS are able to reproduce inferred temperatures in ignition-scale experiments on the NIF.

- A. A. Solodov *et al*. describe an experimental platform fielded on the NIF for investigating hot-electron production from laser–plasma instabilities at direct-drive ignition-relevant conditions (p. 198). Hot-electron conversion efficiencies between 0.5% and 5% were inferred when quarter-critical intensities were varied from ∼4 to 15×10^{14} W/cm^2.

- H. Wen *et al*. use 3-D particle-in-cell (PIC) simulations to investigate the interplay between two-plasmon decay and SRS in conditions relevant to inertial confinement fusion experiments (p. 200). In comparison to 2-D PIC simulations, this results in a fast-electron fraction level much closer to experimental measurements.

- Y. Zhao and W. R. Donaldson detail the fabrication of aluminum–gallium–nitride photodetectors with micrometer-scale metal–semiconductor–metal structures (p. 205). The diagnostic was tested with ultrafast UV laser pulses.

- C. Dorrer, E. M. Hill, and J. D. Zuegel demonstrate efficient parametric amplification of broadband spectrally incoherent pulses (p. 208). These results will be applied to the development of a 1% fractional bandwidth laser that promises smoother profiles and improved performance in direct-drive implosions.

- M. J. Guardalben *et al*. describe *PSOPS*, a MATLAB-based semi-analytic model for the OMEGA EP Laser System to predict system performance (p. 211). The model has reaped the benefits of real-time optimization of the laser system configuration and enabled several enhancements to the laser system performance.

- H. Huang *et al.* present a method for calculating the Raman fluency at the surface of an arbitrary crystal and pump polarization configurations for the purpose of better understanding laser power level limitations in transverse Raman generation and amplification in KDP/DKDP crystals (p. 218). A code using this method is able to provide estimates of maximum laser intensity that will not damage the amplification medium.

- T. Z. Kosc *et al.* investigate the damage resistance of liquid crystals for laser excitation conditions, including those relevant to OMEGA (p. 220). The data suggest a complex interplay of both multiphoton absorption and excited-state absorption are key components in laser-induced–damage mechanisms.

- S. MacNally *et al.* study multilayer glancing-angle deposition on a silica substrate for reducing light scattering on film (p. 222). Applying this technique gave measured persistently low-scatter loss compared to single-layer coating runs.

- J. B. Oliver, B. Charles, and J. Spaulding present an optical coating technique using radially nonuniform film deposition that was developed to mitigate deformations induced by high-compressive films and create a nominally flat coated surface (p. 225). Using this technique, surface deformations were reduced by nearly 90% relative to that of a coated surface without a graded corrective layer.

- E. Schiesser *et al.* describe details for a four-mirror image relay—the theoretical basis for the correction of a field-constant coma and field-constant astigmatism (p. 227). The alignment of the design in a test-bed setup is then presented.

- C. Smith, S. MacNally, and J. B. Oliver describe a process using ellipsometric measurement techniques along with a well-established optical coating design to create precise index models for improved coating design (p. 232). This is made possible by a complex optical coating using only a single material.

- R. B. Spielman and A. B. Sefkow describe the design of a variable-impedance, disk magnetically insulated transmission line (MITL) that allows for the reduction in inductance of disk MITL's (p. 234). Electron flow and losses are shown using 2-D electromagnetic PIC simulations.

R. S. Craxton summarizes the 31st LLE Summer High School Research Program. Fourteen students were invited from Rochester-area high schools to participate in the lab's state-of-the-art research environment (p. 237).

J. Puth, M. Labuzeta, and D. Canning summarize operations of the Omega Laser Facility during the fourth quarter of FY19 (p. 239).

Duc Cao
Editor

Theory of Ignition and Burn Propagation
in Inertial Fusion Implosions

A. R. Christopherson,[1,2] R. Betti,[1,2,3] S. Miller,[1,2] V. Gopalaswamy,[1,2] O. M. Mannion,[1,3] and D. Cao[1]

[1]Laboratory for Laser Energetics, University of Rochester
[2]Department of Mechanical Engineering, University of Rochester
[3]Department of Physics & Astronomy, University of Rochester

A large effort is currently underway to demonstrate thermonuclear ignition in the laboratory via inertial confinement fusion (ICF).[1] ICF uses laser-driven implosions of a solid deuterium–tritium (DT) shell to achieve ignition conditions.[2,3] Ignition is a thermal instability of a DT plasma driven by the energy deposition of the alpha particles ("alpha heating") produced by the fusion reaction D + T = α(3.5 MeV) + n(14.1 MeV). Ignition has never been achieved in a laboratory plasma, and its demonstration is widely viewed as a major scientific achievement with important applications to fusion energy generation and to the stewardship of the nuclear stockpile. Unlike in steady-state plasmas, as those envisioned for magnetic confinement fusion,[4] assessing ignition in ICF is greatly complicated by the transient nature of implosions and the fact that ignition starts from the central hot region ("hot-spot ignition") and then propagates to the cold and dense surrounding fuel ("burn-wave propagation"). The fundamental mechanism at the basis of ignition is alpha heating of the DT fuel and its positive feedback on the fusion reaction rate.

Current experiments at the National Ignition Facility have demonstrated significant alpha heating, leading to amplifications of the fusion yield close to threefold.[5–7] Despite much work on assessing and measuring the degree of alpha heating, two crucial questions remain unanswered with regard to ignition: (1) What is ignition in inertial fusion; and (2) what fusion yields are required in ICF to claim that ignition has taken place. In the past, common metrics for ignition have related the fusion yield to the incident laser energy on target. The so-called *target gain* = 1 condition has been widely used as the ultimate indicator of ignition.[8] Here, target gain is the ratio of the fusion energy output to the laser energy on target. Such a metric is not rooted in the burning-plasma physics of DT fuel and is unrelated to the onset of ignition. It is motivated only by its implications to fusion energy, where an energy output greater than the input is required for any viable fusion scheme. This metric is not an indicator of the onset of the thermonuclear instability and therefore cannot be used to measure the ignition point.

In this work, we provide a physical definition of hot-spot ignition in ICF, which is of general validity for laser fusion. This definition of ignition identifies the onset of the thermal runaway within the hot spot of an ICF implosion just prior to the burn propagation in the dense fuel. To identify the ignition point, we first search for qualitative features distinguishing runaway burn in the entire fuel volume from sub-ignition alpha heating. The first distinctive feature is related to the different behavior of the yield amplification for implosions in the alpha-heating regime versus implosions with propagating burn. Here the yield amplification = $Y_\alpha / Y_{no\,\alpha}$, where Y_α is the fusion yield measured in an experiment and $Y_{no\,\alpha}$ is the estimated yield without accounting for alpha-particle energy deposition. It was shown in Ref. 9 that in the alpha-heating regime, the yield amplification depends uniquely on the dimensionless parameter f_α given by

$$f_\alpha \equiv \frac{1}{2}\frac{\theta_\alpha E_\alpha}{E_{hs}},\tag{1}$$

where E_α is the total alpha-particle energy, θ_α is the fraction of alpha particles deposited into the hot spot, and E_{hs} is the hot-spot internal energy at bang time (when the neutron-production rate is maximized). The parameter f_α is designed to compare the

deposited alpha energy to the hot-spot internal energy at bang time. In the numerator, $E_\alpha = \varepsilon_\alpha \cdot$ Yield, where $\varepsilon_\alpha = 3.5$ MeV and Yield is the neutron yield. The factor 1/2 accounts for the fact that approximately one half of all of the fusion alphas produced have deposited their energy into the hot spot at bang time. In defining E_{hs}, the hot-spot radius is the point where the neutron-production rate drops to 17% of its maximum value. The Lagrangian trajectory of this hot spot is then back calculated in time to determine the fraction of alpha particles absorbed in the hot spot, as was done in Refs. 10 and 11.

In Fig. 1, the yield amplification resulting from alpha heating is plotted as a function of f_α, where the yield amplification curves for many different targets are shown to overlap up to a critical value of $f_\alpha = 1.4$. The simulation ensemble shown here contains implosion velocities between 200 km/s and 600 km/s, laser energies between 30 kJ and 10 MJ, and adiabats between 1 and 6, where the adiabat[12] is given for DT by $\alpha = P/2.2\rho^{5/3}$, with the shell pressure P in megabars and the plasma density in g/cm^3. The database was generated by creating many ignited implosions with a variety of different target gains and then degrading them by reducing the implosion velocity, increasing the adiabat, or by applying density modulations to the inner shell surface. Ignition occurs at the critical value $f_\alpha = 1.4$ corresponding to a yield amplification due to alpha heating of about 15× to 25×. For $f_\alpha < 1.4$, alpha heating is mostly confined to the hot spot, while for $f_\alpha > 1.4$, the ablation of shell mass into the neutron-producing region significantly increases the fusion output.
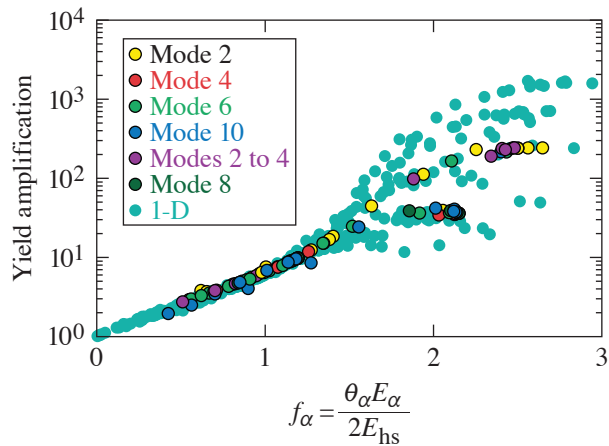
TC14995JR

Figure 1
The yield amplification is plotted as a function of f_α for the ensemble of 1-D *LILAC*[13] and 2-D *DRACO*[14] simulations. In the alpha-heating regime ($f_\alpha < 1.4$), the yield amplification depends uniquely on f_α regardless of the target mass, areal density, and temperature. After $f_\alpha = 1.4$, shell mass and burnup fraction determine the maximum fusion yield.

1. J. Nuckolls *et al.*, Nature **239**, 139 (1972).

2. S. Atzeni and J. Meyer-ter-Vehn, *The Physics of Inertial Fusion: Beam Plasma Interaction, Hydrodynamics, Hot Dense Matter*, 1st ed., International Series of Monographs on Physics, Vol. 125 (Oxford University Press, Oxford, 2004); J. D. Lindl, *Inertial Confinement Fusion: The Quest for Ignition and Energy Gain Using Indirect Drive* (Springer-Verlag, New York, 1998).

3. J. D. Lawson, Proc. Phys. Soc. Lond. B **70**, 6 (1957).

4. J. Ongena *et al.*, Nat. Phys. **12**, 398 (2016); **12**, 717(E) (2016).

5. S. Le Pape *et al.*, Phys. Rev. Lett. **120**, 245003 (2018).

6. T. Döppner *et al.*, Phys. Rev. Lett. **115**, 055001 (2015).

7. O. A. Hurricane *et al.*, Nature **506**, 343 (2014).

8. Committee on the Prospects for Inertial Confinement Fusion Energy Systems National Research Council (NRC), *An Assessment of the Prospects for Inertial Fusion Energy* (The National Academies Press, Washington, DC, 2013).

9. A. R. Christopherson *et al.*, Phys. Plasmas **25**, 072704 (2018).

10. A. R. Christopherson *et al.*, Phys. Plasmas **25**, 012703 (2018).

11. A. R. Christopherson and R. Betti, Phys. Rev. Lett. **99**, 021201(R) (2019).

12. M. C. Herrmann, M. Tabak, and J. D. Lindl, Nucl. Fusion **41**, 99 (2001).

13. J. Delettrez *et al.*, Phys. Rev. A **36**, 3926 (1987).

14. P. B. Radha *et al.*, Phys. Plasmas **12**, 056307 (2005).

Hybrid Target Design for Imprint Mitigation in Direct-Drive Inertial Confinement Fusion

L. Ceurvorst,[1] R. Betti,[2] A. Casner,[1] V. Gopalaswamy,[2] A. Bose,[2] S. X. Hu,[2] E. M. Campbell,[2] S. P. Regan,[2] C. A. McCoy,[3] M. Karasik,[4] J. Peebles,[2] M. Tabak,[5] and W. Theobald[2]

[1]Université de Bordeaux-CNRS-CEA, CELIA
[2]Laboratory for Laser Energetics, University of Rochester
[3]Sandia National Laboratories
[4]Plasma Physics Division, Naval Research Laboratory
[5]Lawrence Livermore National Laboratory

We propose a novel target design, called the hybrid direct-drive target design, for mitigating the Rayleigh–Taylor instability (RTI) in high-energy-density and direct-drive inertial confinement fusion experiments.[1] Figure 1 shows a schematic of the design in both (a) spherical and (b) planar geometries. The target is surrounded by a thin (less than 1-μm) CH membrane that is externally coated with a tens-of-nm-thick layer of Au. The membrane is offset by several hundred microns from the target's surface. A high-intensity laser picket pulse is incident on the membrane, producing smooth x-ray radiation that serves as the initial seed on the target surface and drives the first shock through the target. After giving the target time to develop its conduction zone, between a few hundred ps to ~1 ns, the main pulse propagates through the underdense plasma from the exploded membrane and drives the target itself. A proof-of-concept experiment in planar-target geometry on the OMEGA EP laser explored the performance of
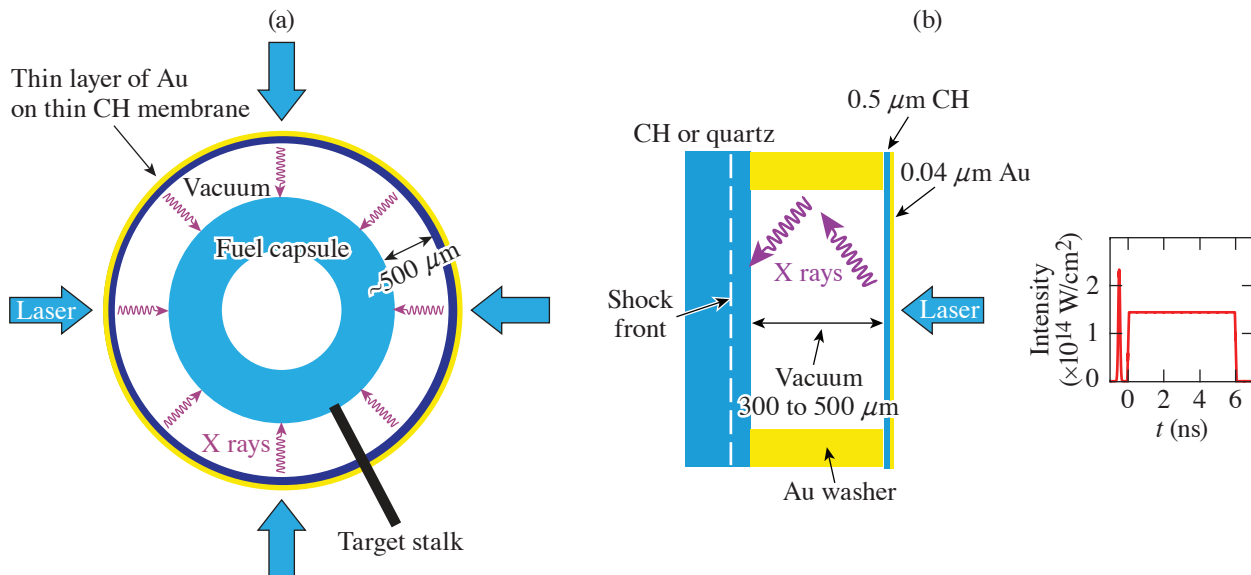
E28623JR

Figure 1
Schematic of (a) the spherical hybrid direct-drive target design and (b) the planar target design that was tested in the experiment.

this newly proposed concept for the first time. The experiment provided the pressure of the x-ray–driven shock wave and tested the target's imprint-mitigation capabilities. Figure 1(b) shows the design of the planar target.

A 1.5-mm-OD Au washer with a 20-μm-thick wall and a height of 300 μm or 500 μm was glued on planar quartz or polystyrene foils. The height of the washer determines the standoff distance of a 0.5-μm-thick CH membrane from the target plane. Depending on this height, the targets will be referred to as the "Hybrid300" or "Hybrid500" targets, respectively. The membrane was coated with an ~40-nm layer of Au. The space between the planar target and the membrane was held at vacuum. The Au side was irradiated with one UV beam equipped with an SG8-750 distributed phase plate. The pressure measurements used 140-μm-thick polystyrene and quartz foils. A short picket pulse (no main pulse) with a 150-ps duration and an intensity of 1 to 2×10^{14} W/cm^2 interacted with the Au coating to generate the x-ray pulse that created the shock wave that was observed from the target back side with a velocity interferometer system for any reflector (VISAR) diagnostic and a streaked optical pyrometer (SOP). The diagnostics measured the propagation velocity and the emission temperature, which made it possible to infer the pressure of the decaying shock wave. The Hybrid300 target obtained a pressure of ~8 Mbar at ~0.5 ns after the start of the laser pulse, while about half of the pressure was obtained at this time with the Hybrid500 target. The imprint shots applied a standard platform of time-gated face-on x-ray radiography but used a thinner 30-μm-thick planar polystyrene foil to be able to accelerate the target with a 6-ns square pulse and to amplify the seeds by RTI. No smoothing by spectral dispersion was used, causing the beam speckle pattern to serve as 3-D, multimode imprint seeds for ablative RTI. The evolution of ablative RTI was observed through face-on x-ray radiography at different times. The performance of the hybrid targets was compared to a bare 30-μm-thick polystyrene foil without an Au washer. The picket intensity was increased by about a factor of 2 in the hybrid case so that the x rays created by the picket would generate an initial shock matching the 1-D performance of the bare targets. The 1-D simulations show that the behavior of both targets is identical across designs, yielding an acceleration of 35 μm/ns^2.

Azimuthally averaged Fourier spectra of the OD modulations at different times are shown in Figs. 2(a) and 2(b) for both the bare and hybrid targets. Modulation growth was significantly reduced in both hybrid targets. The bare target reached a peak amplitude of 4.1×10^{-2} OD after just 3.1 ns as opposed to Hybrid300 reaching a similar level of 2.6×10^{-2} OD after 4.2 ns. The Hybrid500 target did not exceed noise band. The experiments show a reduction of the RTI growth and a delay in the time of target perforation by ~40% in the Hybrid300 target compared to the bare CH target. In summary, the performance of the hybrid target design

E28626JR
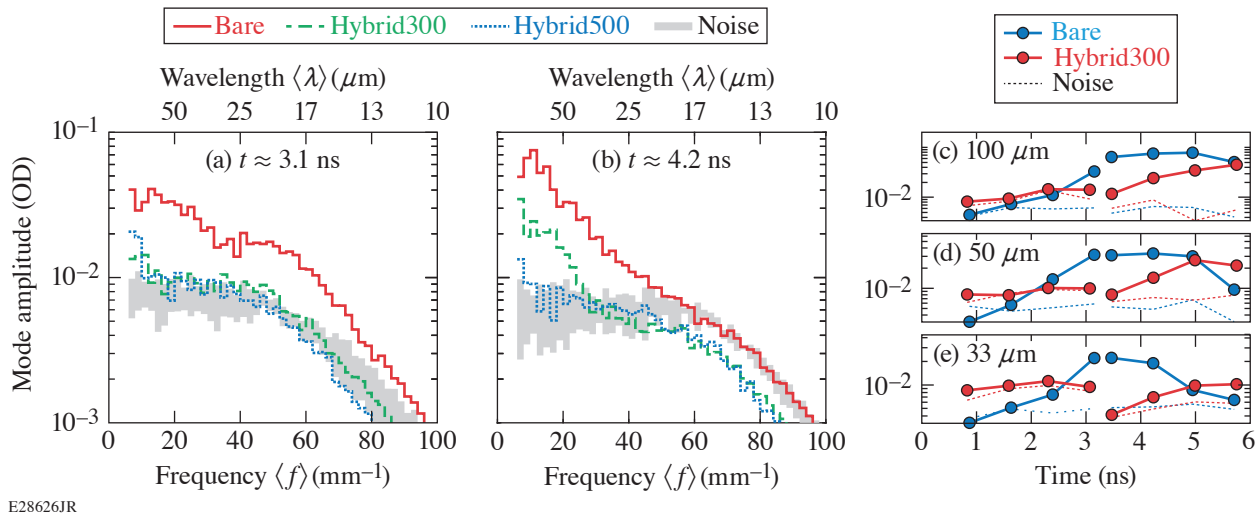
Figure 2

The azimuthally averaged Fourier spectra of the three targets and individual wavelength evolution. (a) Significant growth above noise has occurred by 3.1 ns for the bare target across the measurable spectrum. (b) The Hybrid300 target begins to exceed noise by 4.2 ns only at frequencies below ~30 mm^{-1}. [(c)–(e)] The evolution of specified wavelengths are compared between bare (blue) and Hybrid300 (red) targets. The dotted lines represent the noise levels of the corresponding target type.

has been measured for the first time through planar experiments performed on the OMEGA EP laser. Shocks were shown to be generated by the x-ray flashes with pressures that are in agreement with calculated pressures from 1-D radiation-hydrodynamic simulations using the code *LILAC*, and the growth of the ablative RTI was significantly reduced for the hybrid targets.

1. L. Ceurvorst *et al*., Phys. Rev. E **97**, 043208 (2018).

A Boundary Condition for Guderley's Converging Shock Problem

J. J. Ruby,[1,2] J. R. Rygg,[1,2,3] J. A. Gaffney,[4] B. Bachmann,[4] and G. W. Collins[1,2,3]

[1]Laboratory for Laser Energetics, University of Rochester
[2]Department of Physics and Astronomy, University of Rochester
[3]Department of Mechanical Engineering, University of Rochester
[4]Lawrence Livermore National Laboratory

The Guderley problem[1] consists of a 1-D radially converging shock wave supported to infinity. The solution consists of leveraging the group invariance of the flow equations, along with an ideal equation of state, to reduce the set of partial differential equations into a single ordinary differential equation. The result is a simplified self-similar model describing the collapse of spherical shock waves.

This model has been used for understanding the shocks in laser-driven implosions in the past.[2] In particular the model has been used to predict the neutron yield from spherical implosions.[2,3] This work sets out to make two modifications to the Guderley solution that extend its utility for understanding implosions.

The first of the modifications includes the addition of an isentropic release wave launched from some reference radius. This corresponds to the pressure no longer being supported, such as when the laser turns off in a laser-driven implosion. In this case the release wave will be launched from the ablation surface as the remaining solid density material releases into vacuum. This wave breaks the self-similarity of the solution and changes the density profile in the shocked region. The density profile of the release is

$$\rho(r) = \rho_R \left(\frac{R_{\text{out}} - r}{R_{\text{out}} - R_{\text{in}}} \right)^{\epsilon}, \tag{1}$$

with R_{out} and R_{in} referring to the inner and outer edges of the release wave, respectively. The inner edge trajectory of the release wave is known assuming it moves at the local sound speed of the material and is launched from a known location at a known time. The outer edge of the release wave is then solved for using the conservation of mass in the released region. The temperature and pressure in the released material are then solved for by using the adiabatic relationship and an ideal equation of state.

The second modification includes taking the single fluid temperature present in the Guderley solution and partitioning it between an electron fluid and an ion fluid based on their masses. Additionally, a scheme for the fluids equilibrating is introduced based on Spitzer. The temperatures are constrained to satisfy

$$T_i + \overline{Z} T_e = (1 + \overline{Z}) T_G, \tag{2}$$

where T_e and T_i are the electron and ion temperatures, respectively, and T_G is the single-fluid temperature. This leaves the single-fluid temperature unchanged, so the hydrodynamics are unperturbed. Finally, the temperatures equilibrate according to[4]

$$\frac{dT_e}{dt} = \frac{T_i - T_e}{\tau_{ei}}. \tag{3}$$

The results of the modified Guderley solution are compared to *LILAC* simulations of an 860-μm solid CH sphere driven by a 2-ns square pulse. In order to set the parameters of the Guderley solution, the initial shock pressure and the time of shock collapse were set to match the *LILAC* results. Figure 1(a) compares the trajectories from *LILAC* and the Guderley solution. The shock and release wave trajectories compare well between the two models. The shock trajectory after the release wave hits the outgoing shock is the most obvious difference between the two models. This is because the shock trajectory in the Guderley model is unchanged by the release.

Figure 1(b) compares the total x-ray yield from the shock collapse that escapes the sphere as a function of initial density of the target. As the density decreases, the release modification is less relevant because the material is much less efficient at absorbing x rays, and as the density increases, temperature equilibration is less important because the time scale for coupling is so short that the material is equilibrated instantaneously with respect to the emission time scale. Only the model that includes both modifications is able to reproduce the *LILAC* results over a broad range of the density space.

E28606JR
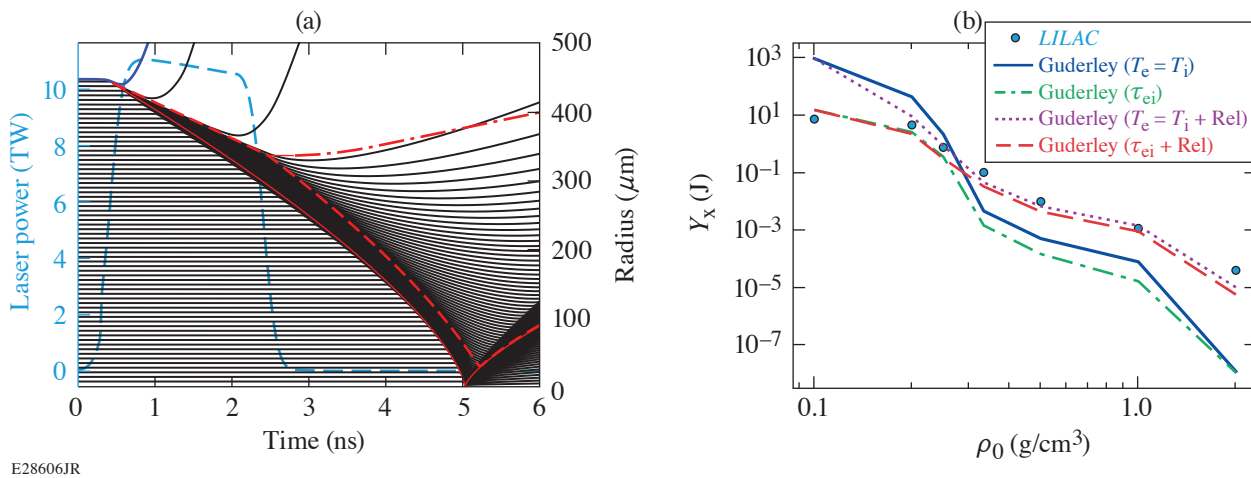
Figure 1

(a) A comparison of the wave trajectories for the modified Guderley solution (red curves) plotted over the particle trajectories from *LILAC* (black curves). The *LILAC* pulse shape is shown by blue curves. (b) A comparison of total x-ray yield in joules across different models: *LILAC* (solid circles), standard Guderley (solid blue curve), Guderley with temperature equilibration (dashed–dotted green curve), Guderley with release modification (dotted purple curve), and Guderley with release and temperature equilibration (dashed red curve). The simulations were run given the same conditions but with a scaled initial density to highlight regions where different physics played a key role.

The modified Guderley solution has proved capable of reproducing many results from *LILAC* with many fewer input parameters. This work was done with the ultimate goal of using both models to infer important physics information from spherical experiments through a Bayesian model-fitting procedure.

1. G. Guderley, Luftfahrtforschung **19**, 302 (1942).

2. J. R. Rygg, "Shock Convergence and Mix Dynamics in Inertial Confinement Fusion," Ph.D. Thesis, Massachusetts Istitute of Technology, 2006.

3. H. J. Haubold and R. W. John, Plasma Phys. **23**, 399 (1981).

4. L. Spitzer, *Physics of Fully Ionized Gases* (Interscience Publishers, New York, 1956).

Nonlinear Transmission of Laser Light Through Coronal Plasma due to Self-Induced Incoherence

A. V. Maximov, J. G. Shaw, and J. P. Palastro

Laboratory for Laser Energetics, University of Rochester

The success of direct laser-driven inertial confinement fusion (ICF) relies critically on the efficient coupling of laser light to plasma. At ignition scale, the absolute stimulated Raman scattering (SRS) instability can severely inhibit this coupling by redirecting and strongly depleting laser light. This summary describes a new dynamic saturation regime of the absolute SRS instability. The saturation occurs when spatiotemporal fluctuations in the ion-acoustic density detune the instability resonance. The dynamic saturation mitigates the strong depletion of laser light and enhances its transmission through the instability region, explaining the coupling of laser light to ICF targets at higher plasma densities.

While still in the research stage, controlled fusion could deliver an almost endless supply of power with relatively low environmental impact and a nearly inexhaustible reserve of fuel. As evidenced by active research programs throughout the world, the realization of such a technology would have lasting impact both geopolitically and for the health of our planet. In the direct-drive ICF approach, an ensemble of laser beams symmetrically illuminates a cryogenic target containing thermonuclear fuel.[1] The illumination ionizes and heats the outer shell of the target, creating a pressure that drives inward fuel compression and outward mass ejection. The mass ejection creates a region of low-density plasma, or corona, that plays a critical role in direct-drive ICF: coupling of laser light to the corona determines the strength of the ablation pressure and, ultimately, the implosion performance.[1]

Achieving efficient coupling of laser energy to the fusion target is arguably the most essential component of direct-drive ICF. A high ablation pressure requires the transmission of laser light to deep within the corona, where collisions can efficiently convert electromagnetic energy to plasma thermal energy. To get there, however, the laser light must propagate through the outer corona, where it can drive a number of parametric instabilities. In their nonlinear stage, these instabilities can redirect the incident light into unwanted directions and repartition the light energy into plasma waves. These waves can subsequently undergo local collisional damping, in which case the energy is deposited too far from the ablation surface, or collisionless damping, which creates nonthermal electrons that can preheat the fuel and reduce its compressibility.[1] In either case, the premature depletion of laser energy in this region presents a significant challenge for direct-drive ICF.

Within the U.S., the primary direct-drive program has been centered around LLE's OMEGA laser. Compared to the National Ignition Facility (NIF), the high repetition rate of OMEGA serves as an ideal platform for studying the underlying physics of direct drive. However, due to its limited laser pulse energy (30 kJ), the OMEGA laser cannot create the conditions required for a burning fusion plasma. As a result, the focus has turned to direct-drive implosions on the NIF. With its larger laser energy (>1 MJ), the NIF can drive larger capsules, which changes the characteristics of the plasma, e.g., the corona has a longer scale length and higher electron temperature. As a result, absolute SRS becomes the dominate instability[2] in contrast to OMEGA experiments in which two-plasmon decay (TPD) dominates.

In SRS, an incident laser light wave decays into a scattered Raman light wave and an electron plasma wave. In a region near the quarter-critical plasma density n_c, determined by the frequency of the laser, the SRS decay waves can grow exponentially in time as an absolute instability until they nonlinearly saturate. Recent planar-target experiments on the NIF that emulated the plasma corona of an ignition-scale direct-drive implosion showed a clear SRS feature originating from close to the quarter-critical

density and no clear evidence of TPD.[2] The observations confirmed theoretical estimates that, because of the large density scale lengths in the plasma corona (of the order of few hundred microns), the threshold for absolute SRS would be exceeded. Those same estimates also suggest that the instability would strongly deplete the laser light, preventing significant transmission deep into the corona. The hydrodynamic evolution of the target was consistent, however, with the efficient conversion of laser energy into plasma thermal energy.[2] As a result, a critical question emerges: How can the laser light propagate through the absolute instability region with a high transmission rate?

The discovery of a dynamic saturation regime of the absolute SRS instability due to self-induced incoherence answers this question. As the incident light propagates through the instability region, it drives a primary SRS decay that initially depletes the laser intensity. The electron plasma waves resulting from the SRS decay then undergo a secondary instability that drives a broad spectrum of low-frequency density perturbations. The instability saturates when the density perturbations reach a high enough level to detune the primary SRS resonance, establishing a dynamic balance between the transmitted and scattered laser light. This dynamic, incoherent saturation mitigates depletion and facilitates the transmission of the laser light through the instability region, explaining how light can penetrate deep into the corona to efficiently drive ICF implosions.

To investigate the saturation of absolute SRS in the regime relevant to direct-drive implosions at the NIF scale, the laser-plasma simulation environment (*LPSE*)[3] was employed. *LPSE* applies a fluid plasma model to describe the evolution of the four waves (light, Raman, electron plasma, and ion acoustic) and the couplings between them. The simulations were performed in two spatial dimensions with *s*-polarized light. The laser light was normally incident on a plasma with linear gradient $n = n_c\left(1 + x/L\right)/4$, where L is the density scale length at the quarter-critical density. The plasma parameters are as follows: laser wavelength = 0.351 μm; density scale length = 500 μm; electron temperature = 4 keV; ion temperature = 4 keV; ion charge $Z = 3.5$; ion atomic number = $2Z$; and density range from 0.21 to 0.265 n_c. At these conditions, the threshold for TPD is more than 3× higher than the threshold for absolute SRS.

Figure 1 illustrates the nonlinear saturation of absolute SRS for laser light with an incident intensity of 2×10^{14} W/cm^2 (approximately 3× greater than the theoretical instability threshold at these parameters, 6×10^{13} W/cm^2). Early in time, the laser light propagates through the plasma without scattering but undergoes a small amount of collisional absorption, about 2%; shortly thereafter, the absolute instability develops. By 5.4 ps, the instability has strongly depleted the pump [Fig. 1(a)], and the Raman light [Fig. 1(c)] has grown to an amplitude comparable to the laser light. This pump depletion stage quickly gives way, 3 ps later, to a dynamic saturation stage in which the amplitudes of both the laser and Raman light become nonstationary and spatially incoherent [Figs. 1(b) and 1(d), respectively].

Figure 2 displays the scaling of the transmission, in both the pump depletion (red circles) and dynamic saturation (blue circles) stages, as a function of laser intensity. At intensities below the absolute SRS threshold (6×10^{13} W/cm^2), the transmission is reduced by about 2% due to inverse bremsstrahlung absorption. Above the threshold, the dynamic saturation increases the transmission well above the levels determined by pump depletion alone.

The enhanced transmission explains why the temperature inferred in ignition-scale experiments agrees with radiation-hydrodynamic simulations that do not include a model for absolute SRS.[2] For example, if the intensity reaching the absorption surface was reduced by a factor of 2 due to pump depletion, radiation-hydrodynamic simulations would predict a 30% lower electron temperature.

1. R. S. Craxton *et al.*, Phys. Plasmas **22**, 110501 (2015).

2. M. J. Rosenberg *et al.*, Phys. Rev. Lett. **120**, 055001 (2018).

3. J. F. Myatt *et al.*, Phys. Plasmas **24**, 056308 (2017).
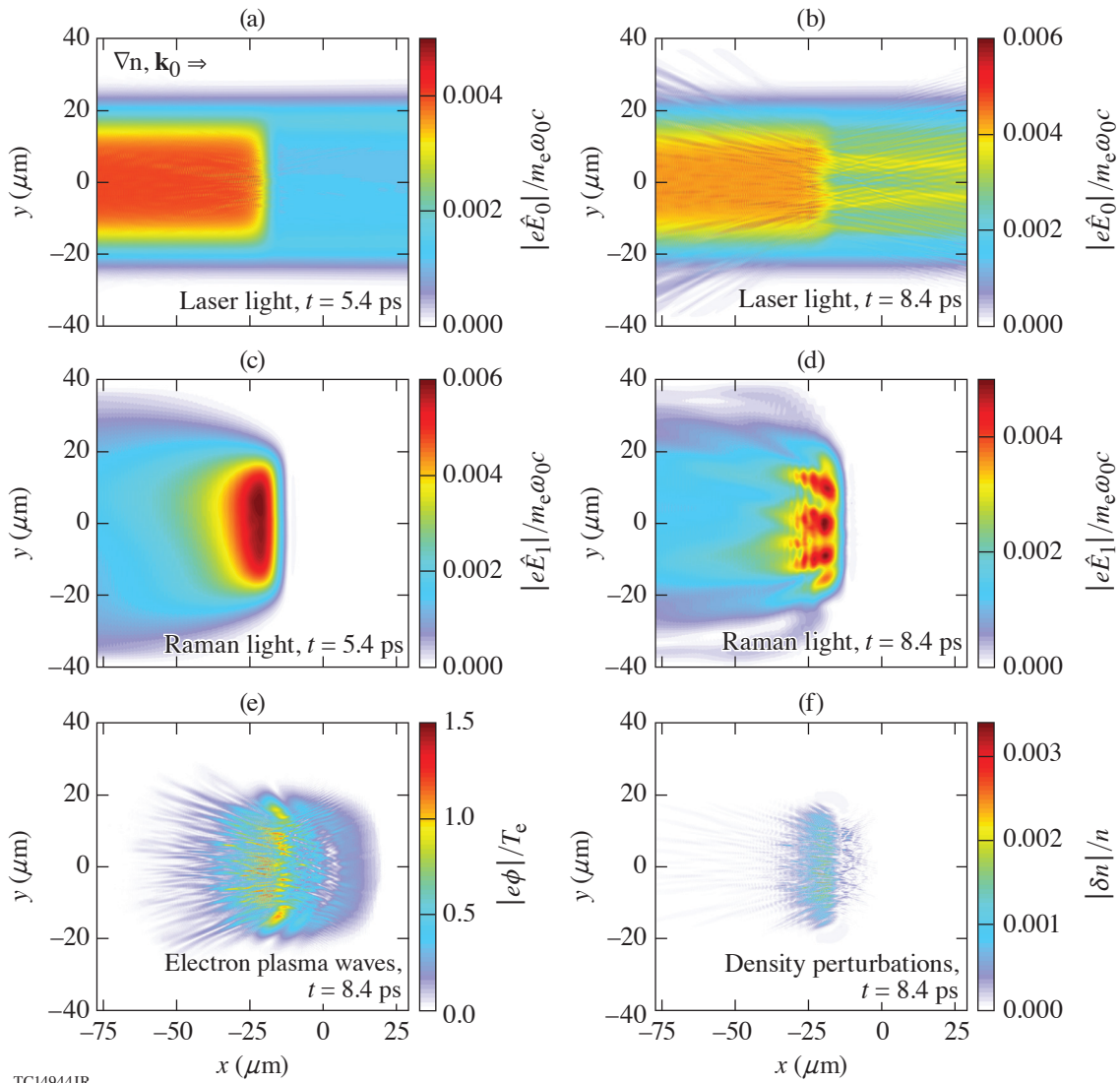
Figure 1
The amplitudes of laser and Raman light waves [(a) and (c), respectively] at 5.4 ps and [(b) and (d), respectively] 8.4 ps. (e) The amplitudes of plasma waves (in terms of wave potential energy normalized to temperature) and (f) low-frequency density perturbations at 8.4 ps.
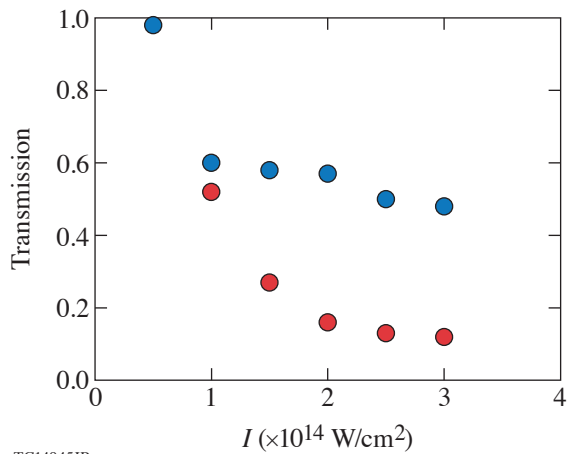
Figure 2
The scaling of light transmission at the end of the pump depletion stage (red circles) and during the dynamic saturation stage (blue circles) as a function of the incident laser intensity.

Hot-Electron Generation at Direct-Drive Ignition-Relevant Plasma Conditions at the National Ignition Facility

A. A. Solodov,[1] M. J. Rosenberg,[1] W. Seka,[1] J. F. Myatt,[2] M. Hohenberger,[3] R. Epstein,[1] C. Stoeckl,[1] R. W. Short,[1] S. P. Regan,[1] P. Michel,[3] T. Chapman,[3] J. D. Moody,[3] R. K. Follett,[1] J. P. Palastro,[1] D. H. Froula,[1] P. B. Radha,[1] and V. N. Goncharov[1]

[1]Laboratory for Laser Energetics, University of Rochester
[2]Department of Electrical and Computer Engineering, University of Alberta
[3]Lawrence Livermore National Laboratory

The direct-drive approach to laser fusion is vulnerable to hot-electron preheat as a result of the long scale length of plasma that exists near the quarter-critical density of the target [$n_{qc} = n_c/4$, where $n_c \approx 1.1 \times 10^{21} \lambda_0^{-2}$ cm^{-3} is the critical density and λ_0 (in μm) is the laser wavelength]. This plasma enables instabilities such as stimulated Raman scattering (SRS)[1] that generate electrostatic plasma waves capable of accelerating electrons. For full-scale, direct-drive–ignition experiments, it is estimated that the target adiabat and performance will be negatively affected if more than ~0.15% of the laser energy is coupled into the cold fuel in the form of hot electrons.[2]

An experimental platform has been fielded at the National Ignition Facility (NIF) to investigate hot-electron production from laser–plasma instabilities at direct-drive ignition-relevant conditions. Planar-target experiments, designed using the radiation-hydrodynamic code *DRACO*,[3] generate plasma and interaction conditions comparable to direct-drive–ignition designs: $I_L \sim 10^{15}$ W/cm^2, $T_e > 3$ keV, and density-gradient scale lengths of $L_n \sim 600$ μm in the quarter-critical density region. Planar targets are currently the only way to achieve direct-drive ignition-relevant plasma conditions on the NIF. A schematic of the experiment and the main diagnostics are shown in Fig. 1(a). All targets—CH or Si disks with a 4.4-mm diameter and thicknesses of 1.2 mm (CH) or 0.75 mm (Si)—were placed at the NIF target chamber center and irradiated from the southern (lower) hemisphere. NIF beams used standard indirect-drive phase plates at best focus and flattop power profiles with a 2-ns linear rise and a total duration of ~7.5 ns. This configuration allowed for the variation of laser–plasma interaction (LPI) conditions by changing the number of
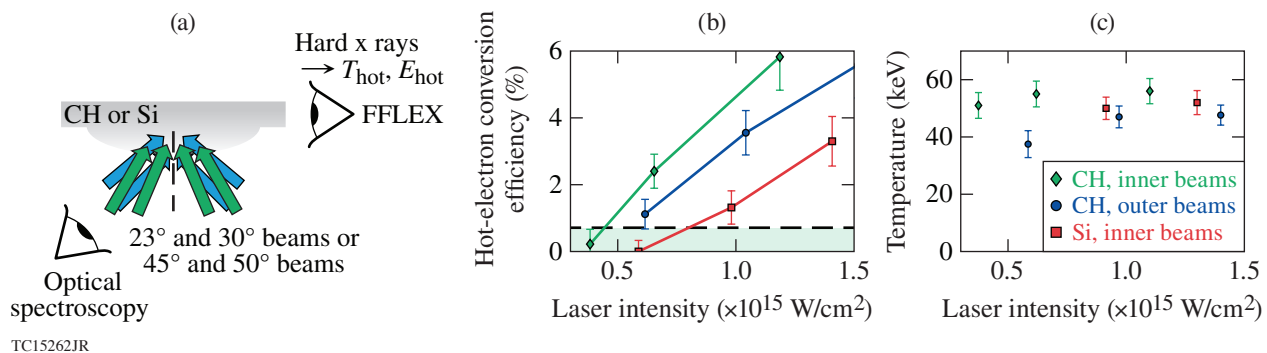
Figure 1
(a) A schematic of the experiment and the main diagnostics. (b) Laser-energy-to-hot-electron conversion efficiency and (c) hot-electron temperature versus laser intensity at the n_{qc}. The dashed horizontal line in (b) shows the hot-electron conversion efficiency of 0.7% considered to be the maximum-tolerable hot-electron preheat for divergent electron beams, as explained in the text. The preheat is tolerable in the light green region below the dashed line.

beams, single-beam intensities, and incidence angles of the beams by using beams in different cones. The higher-angle cones (45° and 50°) approximate irradiation conditions near the equator of a polar-direct-drive implosion, where the beams are incident from higher angles, while the lower-angle cones (23° and 30°) correspond to those near the poles. The use of planar targets reduces the level of cross-beam energy transfer (CBET) relative to spherical targets by excluding the outer parts of the beams, which can propagate around the target and seed CBET with beams from the opposite side.

Hot-electron production in the experiments was inferred by measuring the bremsstrahlung emission spectra using the NIF's ten-channel filter-fluorescer x-ray (FFLEX) diagnostic[4] located in the equatorial plane of the NIF chamber. The measured spectra are approximated well by the one-temperature exponential distributions. The Monte Carlo code EGSnrc[5] was used to relate the properties of hot electrons and measured hard x rays. In EGSnrc, hot electrons from 3-D Maxwellian distributions were injected from the location of the n_{qc} surface with temperatures close to the hard x-ray temperatures and with a full divergence angle of 2π toward the target.

Figure 1 shows (b) the laser-energy-to-hot-electron conversion efficiencies and (c) hot-electron temperatures inferred by comparing experiments and simulations versus the laser intensity at n_{qc} predicted by *DRACO*. The results are shown for CH targets illuminated either by inner beams (green diamonds) or outer beams (blue circles) and Si targets illuminated by inner beams (red squares). The dashed horizontal line in Fig. 1(b) shows the maximum-tolerable hot-electron conversion efficiency for divergent electron beams of 0.7%. It is obtained by estimating that with a near-2π angular divergence, only ~25% of the hot electrons will intersect the cold shell and result in preheat. Additionally, electrons at energies below ~50 keV will be stopped by the ablator. A large (near-2π) hot-electron divergence was demonstrated in previous spherical experiments on OMEGA and will be re-evaluated in the near-term implosion experiments on the NIF. Scattered-light spectrum measurements demonstrate that the most plausible mechanism of hot-electron generation in the NIF experiments is SRS.[6]

According to Figs. 1(b) and 1(c), in plastic ablators, hot-electron temperatures of ~40 keV to 60 keV and fractions of laser energy converted to hot electrons of ~0.5% to 5% were inferred when the laser intensity near the quarter-critical density increased from ~4 to 15×10^{14} W/cm^2. The intensity at n_{qc} is approximately 2× lower than the incident laser intensity due to inverse bremsstrahlung absorption. An acceptable hot-electron fraction of 0.7% of the laser energy (for divergent hot-electron beams) is exceeded if the overlapped intensity at the quarter-critical surface exceeds ~4×10^{14} W/cm^2 in plastic ablators.

Hot-electron preheat mitigation strategies are desired to extend the ignition design space to quarter-critical intensities above 4×10^{14} W/cm^2. Using mid-Z layers strategically placed in the plastic ablator materials was previously shown to suppress hot-electron generation by two-plasmon decay in smaller-scale implosions on OMEGA.[7] Our experiments using silicon planar targets demonstrate [Fig. 1(b)] that hot-electron production is also reduced in the longer-scale-length plasmas on the NIF, relevant to direct-drive ignition, in which SRS is the dominant LPI process. If the electron divergence is large, the direct-drive–ignition design space may potentially be extended to quarter-critical intensities up to ~8×10^{14} W/cm^2 by introducing silicon layers in the ablators.

1. W. Seka *et al*., Phys. Fluids **27**, 2181 (1984); H. Figueroa *et al*., Phys. Fluids **27**, 1887 (1984); C. S. Liu, M. N. Rosenbluth, and R. B. White, Phys. Fluids **17**, 1211 (1974).

2. J. A. Delettrez, T. J. B. Collins, and C. Ye, Phys. Plasmas **26**, 062705 (2019).

3. P. B. Radha *et al*., Phys. Plasmas **12**, 032702 (2005).

4. M. Hohenberger *et al*., Rev. Sci. Instrum. **85**, 11D501 (2014).

5. I. Kawrakow, Med. Phys. **27**, 485 (2000); I. Kawrakow *et al*., National Research Council Canada, Ottawa, Canada, NRCC Report PIRS-701 (May 2011).

6. M. J. Rosenberg *et al*., Phys. Rev. Lett. **120**, 055001 (2018).

7. R. K. Follett *et al*., Phys. Rev. Lett. **116**, 155002 (2016).

Three-Dimensional Particle-in-Cell Modeling of Parametric Instabilities Near the Quarter-Critical Density in Plasmas

H. Wen,[1,2] A. V. Maximov,[1,2] R. Yan,[1,2,*] J. Li,[1,2,†] C. Ren,[1,2,3] and F. S. Tsung[4]

[1]Laboratory for Laser Energetics, University of Rochester
[2]Department of Mechanical Engineering, University of Rochester
[3]Department of Physics and Astronomy, University of Rochester
[4]Department of Physics and Astronomy, University of California, Los Angeles
[*]Present Address: University of Science and Technology of China
[†]Present Address: University of California, San Diego

The interplay between two-plasmon decay (TPD) and stimulated Raman scattering (SRS) is studied using particle-in-cell (PIC) modeling in three dimensions. The TPD-related waves are mostly localized in the plane of polarization,[1] which is defined by the incident laser wave vector (in the x direction) and the laser electric-field vector (in the y direction). The SRS sidescattering develops mostly outside of the polarization plane, and its scattered-light wave vector is almost perpendicular to the incident laser wave vector.[2,3] Scattered-light waves can also propagate in the direction parallel or antiparallel to the laser wave vector (forward- and backscattering, respectively).[4] A 2-D simulation in the polarization plane (x–y) or in the perpendicular plane (x–z) will be referred to as p polarized (PP) or s polarized (SP), respectively. Two-dimensional simulations can model only the interaction where either TPD (in PP) or SRS (in SP) dominates, except for the high-frequency hybrid instability[5] case when the SRS-scattered light propagates in the backward direction and the SRS-related and TPD-related waves are in the same (x–y) plane. The 3-D simulations are required to study the interaction including both TPD and SRS. Here the results of several 3-D simulations for different plasma parameters and incident laser profiles are presented and compared with the respective 2-D simulations to illustrate that both TPD and SRS strongly influence the laser–plasma interaction near-quarter-critical density (1/4 n_c). In the 3-D modeling including both TPD and SRS, the fast-electron flux is reduced by up to an order of magnitude compared to 2-D TPD simulation results published earlier.[6]

Here we describe in detail a 3-D simulation for the parameters relevant to inertial confinement fusion (ICF) experiments.[7,8] A CH plasma is initialized with the electron temperature T_e = 2 keV and the temperatures for both ion species, T_i = 1 keV. The incident laser beam with intensity $I = 9 \times 10^{14}$ W/cm^2 propagates in the direction of density inhomogeneity (x). A linear density profile with the scale length $L = 100$ μm is assumed at the initial time. The size of the simulation box is 21 μm × 8.4 μm × 6.7 μm modeling the density range from 0.21 n_c to 0.26 n_c. Two 2-D simulations (PP and SP) with the same physical parameters were also performed. The TPD threshold parameter η (Ref. 1) is 1.9 ($\eta = 1$ at threshold), and the SRS backscattering threshold parameter N (Ref. 4) is 0.5 ($N = 0.26$ at threshold) for these simulations. The SRS sidescattering threshold[2,3] is close to the backscattering threshold. Both absolute TPD and absolute SRS instabilities are expected to grow. The threshold of the convective SRS[2] is not exceeded for the parameters described above.

The spectra of plasma waves $\left(\left|E_L\right|\right)$ obtained at a time interval between 0.3 ps and 1.0 ps in the 2-D PP and SP simulations are plotted in Figs. 1(a) and 1(b), respectively. From the 3-D simulation, the spectra of plasma waves at a time interval between 1.3 ps and 2.0 ps are plotted in Fig. 1(c) (close to the $k_z = 0$ plane, where TPD dominates) and in Fig. 1(d) (far away from the $k_z = 0$ plane, where SRS dominates). One can see from Figs. 1(c) and 1(d) that TPD and SRS coexist near 1/4 n_c. The spectra of the unstable modes for TPD and SRS are close to the linear theory results (see overlaid lines in Fig. 1).
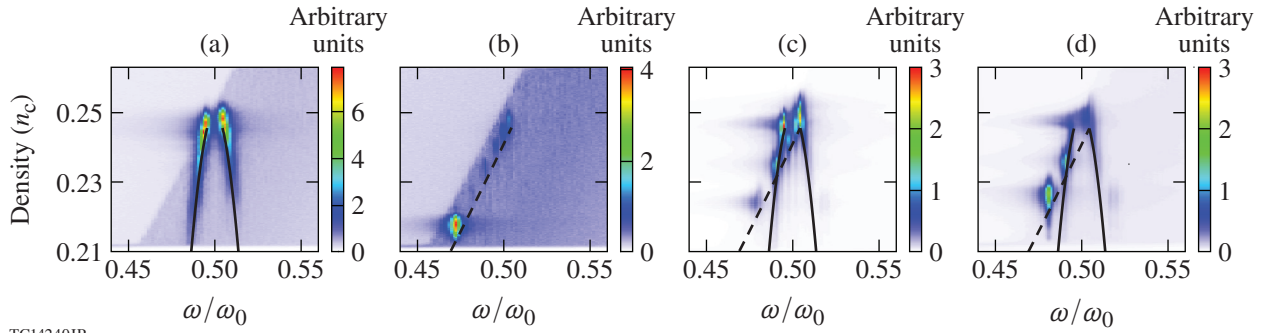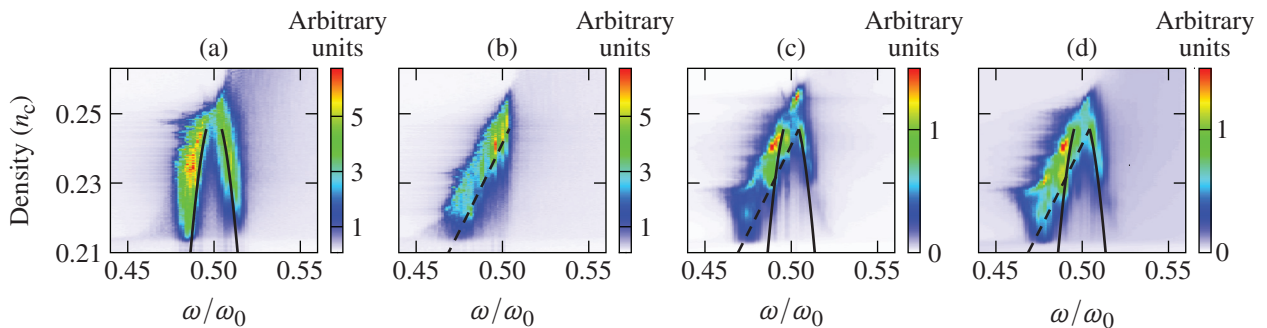
Figure 1

(a) Plasma-wave spectra in the linear instability stage as a function of plasma density and the wave frequency normalized to laser frequency in 2-D PP, (b) 2-D SP, and (c) 3-D simulation for modes with $0 \leq k_z/k_0 < 0.2$ and (d) $0.2 \leq k_z/k_0 < 3$. The overlaid solid black lines and the dashed black lines represent the dispersion relations satisfying the matching conditions for TPD and SRS, respectively.

As the instability evolves from the linear stage to the saturation stage, the frequency spectra shown in Fig. 1 evolve into the spectra shown in Fig. 2. One can see that the spectra in all these simulations are broader in the saturation stage compared to the linear stage. The density in Fig. 2 is calculated using the initial density profile. Compared to 2-D PP [Fig. 2(a)], the TPD is much weaker at densities lower than 0.23 n_c in the 3-D simulation [Fig. 2(c)]. The weakening of the TPD modes at these densities is also illustrated in Fig. 3(a) [and Fig. 3(b)], where the spectrum of plasma waves at densities below 0.23 n_c in the saturation stage is integrated over k_z (and k_y). There are no prominent modes along the TPD hyperbola[9] [solid black line in Fig. 3(a)] at $k_x > k_0$, which corresponds to the TPD daughter waves with larger wave vectors. Two types of low-frequency density fluctuations are identified in our simulations [see Fig. 3(c)]: one type is the ion-acoustic wave driven by the Langmuir-decay instability (LDI),[10,11] and the other type is driven with the beating of the same-frequency daughter waves of SRS and TPD. The LDI modes form a broad feature at $k_x \approx 1.7\, k_0$ (about 2× the laser wave vector in plasma) in the spectrum of the ion density fluctuations shown in Fig. 3(c). The beating of the SRS plasmons with wave vector $(k_x, k_y, k_z) = (0.87\, k_0, 0, \pm 0.2\, k_0)$ creates density perturbations $\langle \delta n \rangle$ with wave vector $(k_x, k_z) = (0, \pm 0.4\, k_0)$. The coupling between SRS plasmons and $\langle \delta n \rangle$ generates higher-order modes in the field at $k_z = \pm(0.2 + m0.4\, k_0)$, [$m = 1, 2 ...$, see Fig. 3(b)] and in the density perturbation at $(k_x, k_z) = [0, \pm(0.4 + m0.4\, k_0)]$ [see Fig. 3(c)].

Although SRS and TPD grow independently in the linear stage, in the nonlinear stage they interact through low-frequency density perturbations. TPD growth starts from the region near 1/4 n_c and spreads to lower densities.[6] Although the peak values of $\langle \delta n \rangle$ are similar in 2-D and 3-D simulations, the peaks are reached at different densities in different simulations: in 2-D PP (without SRS) $\langle \delta n \rangle$ peaks at densities where absolute TPD modes dominate (around 0.245 n_c); in 3-D (with both SRS and TPD)

Figure 2

Plasma-wave spectra in the saturation stage in the 2-D (from 3.3 ps to 4.1 ps) and 3-D (from 2.3 ps to 3.1 ps) simulations as a function of plasma density and wave frequency. Each panel displays the same quantity as in Fig. 1.
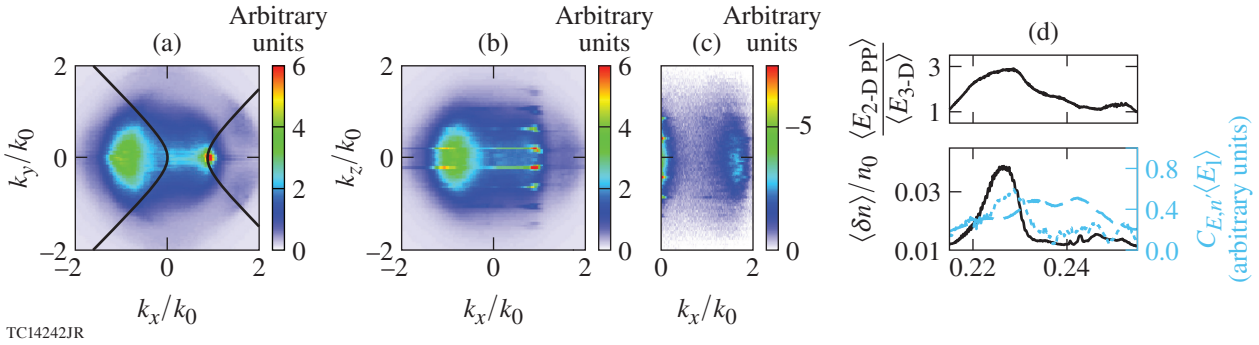
Figure 3

(a) The spectrum of plasmons in the saturation stage of 3-D simulation at densities lower than 0.23 n_c plotted in the $k_x–k_y$ plane and (b) the $k_x–k_z$ plane. (c) The spectrum of ion density fluctuation plotted in the $k_x–k_z$ plane on a logarithmic scale. (d) Lower panel: Ion density fluctuations rms (root-mean-square average over the transverse direction and time) normalized to background density (solid black line), longitudinal electric field rms (dashed blue line) and caviton correlator $C_{E,n}$ (dotted blue line). Upper panel: the ratio of the electric-field amplitude of the TPD plasmons with larger wave vector between 2-D PP and 3-D simulations.

$\langle \delta n \rangle$ peaks at densities where the frequencies of TPD and SRS plasmons are close. In this region where the dispersion lines for TPD and SRS plasmons intersect [near 0.23 n_c in our simulations; see Figs. 2(c) and 3(d)] multiple pairs of SRS and TPD daughter waves have close frequencies and can drive $\langle \delta n \rangle$ through the ponderomotive force to much higher levels compared to other density regions [see the black line in Fig. 3(d)]. The level of $\langle \delta n \rangle$ near 0.23 n_c is lower in 2-D PP than in 3-D simulations. In the 3-D simulation the growth of TPD plasmons at densities below 0.23 n_c, seeded by plasmons from above 0.23 n_c, is disrupted by these enhanced ion density perturbations, as illustrated by a decrease in the level of TPD-driven plasmons below 0.23 n_c in Fig. 2(c).

The correlation between the local plasmon intensity $\left| E_L \right|^2$ and the density fluctuations δn is captured using the caviton correlator[12]

$$C_{E,n} = \left\langle -\delta n \left| E_L \right|^2 \right\rangle \bigg/ \left[\left\langle (\delta n)^2 \right\rangle \left\langle E_L \right\rangle^2 \bigg/ 2 \right].$$

As shown in the lower panel of Fig. 3(d), the plasma waves and the density fluctuations are weakly correlated between 0.255 n_c and 0.235 n_c: $C_{E,n} = 0.1$ to 0.2 in spite of a significant level of plasmons in this density range. At densities close to 0.23 n_c, the lower panel of Fig. 3(d) shows the increase not only in the plasmon intensity and density fluctuations, but also in the correlation between them with $C_{E,n}$ reaching up to 0.6. The large caviton correlator indicates that the plasma waves are strongest in areas where density is depleted. The ponderomotive force of multiple pairs of SRS and TPD daughter waves with close frequencies is responsible for driving the enhanced density perturbations. The nonlinear coupling of TPD and SRS through ion perturbations leads to a lower TPD saturation level in the 3-D simulation compared to the 2-D PP simulation, which is illustrated in the upper panel of Fig. 3(d).

The fast-electron flux is defined as the energy flux carried by electrons with kinetic energy above 55 keV leaving the simulation box minus the energy flux carried by the thermal electrons injected into the simulation region from the thermal boundaries (in the x direction). Information about the hot electrons is collected during the saturation stage in each simulation for 0.5 ps. In the 3-D simulation, the fast-electron flux associated with the forward- and backward-going hot electrons was found to be 1.7% and 0.8%, respectively. The plasma-wave spectrum in the 3-D simulation corresponds to a smaller k-space domain than the spectrum in 2-D PP, which makes the staged acceleration mechanism less efficient in 3-D than in 2-D and explains a smaller number of hot electrons in the 3-D simulation compared to 2-D PP (6.6% and 3.4% in the forward and backward directions, respectively). The influence of wave breaking on the fast-electron generation is small because the maximal electric field amplitude (0.04 $m_e \omega_0 c/e$) is below the wave-breaking limit (0.1 $m_e \omega_0 c/e$) (Ref. 13).

The nonlinear regime including both TPD and SRS is also observed in simulations with the speckled laser beam[14,15] and electron–ion collision effects included. In PIC simulations with periodic boundary conditions, the limited-size simulation region

effectively represents a much larger volume of plasmas and the single speckle in the simulation region mirrors itself in the transverse directions. A series of simulations has been performed to study how the speckles affect the generation of hot electrons. All parameters are the same as the simulations described previously except for the temperatures of electrons and ions being 1.5× higher. The peak intensities in the laser speckles are 1.8×10^{15} W/cm^2 (twice the average intensities). A collision package (CP) is available for the PIC code *OSIRIS*.[16] The main physics processes are observed to be the same in simulations with plane-wave beams and speckled beams.

The fast-electron flux values in simulations are listed in Table I for different incident laser beams as well as with CP turned on and off. By comparing the left and right columns of Table I, one can see that adding collisions can reduce the fast-electron flux by about 50% and in the case of plane-wave 2-D PP simulation by almost 70%. Also note that the reduction of the fast-electron flux caused by collisions affects both the forward-going electrons and backward-going electrons since the collisional damping rate affects all the plasma waves. The fast-electron flux generated in 2-D SP is much smaller than the fast-electron flux generated in 2-D PP, which indicates that the plasma waves driven by TPD are the main source of the electron acceleration.

Table I: Fast-electron flux normalized to the incident laser energy flux.

Fast-electron flux	Forward/Backward	
Collision package	On	Off
Plane wave 2-D PP	1.6% / 1.3%	5.5% / 3.8%
Plane wave 2-D SP	$(< 0.1\%) / 0.2\%$	$(< 0.1\%) / 0.5\%$
Speckle 2-D PP	6.8% / 1.7%	9.4% / 3.8%
Speckle 2-D SP	$(< 0.1\%) / 0.3\%$	$(< 0.1\%) / 0.7\%$
Speckle 3-D	0.4% / 0.3%	0.8% / 0.5%

The hot-electron fraction observed in the ICF experiments on the OMEGA Laser System does not exceed a few percent.[8] At the same time, in the previous PIC simulations of TPD in 2-D, the hot-electron fraction was close to an order of magnitude larger than in the experiments. The 3-D PIC simulations presented here produce the results for the hot-electron fraction that are close to the experimental levels.

Laser–plasma interaction near 1/4 n_c determines the generation of fast electrons that are crucial for the performance of ICF targets. The fast-electron flux in simulations is found to be closely related to the plasma-wave spectra. The TPD-driven plasma waves with large wave vectors are very important for accelerating electrons. At the same time, the SRS-driven plasma waves are less effective in accelerating electrons. Therefore the modeling that includes the nonlinear coupling of TPD and SRS in 3-D is the only way to correctly describe the generation of fast electrons in laser-driven ICF.

Our 3-D PIC simulations have shown the large decrease (up to an order of magnitude) in the fast-electron flux compared to 2-D TPD modeling. The reason is the nonlinear coupling between SRS and TPD, which is especially pronounced at densities lower and around 0.23 n_c. In this region, plasma waves and growing density perturbations are localized in the same areas as illustrated by the caviton correlator. Enhanced density perturbations detune and weaken the TPD-driven plasmons effective in the fast-electron generation. In addition to the TPD suppression, the plasma-wave spectra in 3-D simulations are much more narrow compared to the spectra in 2-D TPD modeling. To conclude, 3-D PIC simulations presented in this summary fully model the laser–plasma interaction near 1/4 n_c, including SRS and TPD, and obtain the fast-electron fraction level close to experimental results, resolving the large discrepancy between ICF experiments and PIC simulations that have existed for many years.

1. A. Simon *et al*., Phys. Fluids **26**, 3107 (1983).

2. C. S. Liu, M. N. Rosenbluth, and R. B. White, Phys. Fluids **17**, 1211 (1974).

3. B. B. Afeyan and E. A. Williams, Phys. Plasmas **4**, 3803 (1997).

4. J. F. Drake and Y. C. Lee, Phys. Rev. Lett. **31**, 1197 (1973).

5. B. B. Afeyan and E. A. Williams, Phys. Plasmas **4**, 3845 (1997).

6. R. Yan *et al*., Phys. Rev. Lett. **108**, 175002 (2012).

7. W. Seka *et al*., Phys. Plasmas **16**, 052701 (2009).

8. D. T. Michel *et al*., Phys. Plasmas **20**, 055703 (2013).

9. J. Meyer and Y. Zhu, Phys. Rev. Lett. **71**, 2915 (1993).

10. D. F. DuBois and M. V. Goldman, Phys. Rev. **164**, 207 (1967).

11. D. F. DuBois, H. A. Rose, and D. A. Russell, Phys. Scr. **T63**, 16 (1996).

12. H. X. Vu *et al*., Phys. Plasmas **19**, 102708 (2012).

13. T. P. Coffey, Phys. Fluids **14**, 1402 (1971).

14. Y. Kato *et al*., Phys. Rev. Lett. **53**, 1057 (1984).

15. S. Skupsky *et al*., J. Appl. Phys. **66**, 3456 (1989).

16. R. A. Fonseca *et al*., in *Computational Science – ICCS 2002*, edited by P. M. A. Sloot *et al*., Lecture Notes in Computer Science, Vol. 2331 (Springer, Berlin, 2002), pp. 342–351.

An Ultrafast, Ultraviolet Metal–Semiconductor–Metal Photodetector Based on AlGaN with a Response Time Below 30 ps

Y. Zhao[1] and W. R. Donaldson[1,2]

[1]Laboratory for Laser Energetics, University of Rochester
[2]Department of Electrical and Computer Engineering, University of Rochester

Aluminum–gallium–nitride (AlGaN) photodetectors have been successfully fabricated with micrometer-scale metal–semiconductor–metal (MSM) structures and tested with ultrafast UV laser pulses. The measurements were taken with single-shot oscilloscopes. Pulse-broadening effects caused by the measurement system were systematically evaluated and reduced to resolve the intrinsic response time of the detector. The best-performing devices showed a response time of below 30 ps and dark currents below 10 pA. The devices showed linear response with the bias voltage and the laser energy.

The $Al_xGa_{(1-x)}N$ (where x denotes the fraction of substituted aluminum) ternary alloys are particularly interesting as UV detectors because of their high tolerance to extreme environments resulting from their thermal stability and radiation hardness.[1] The wide band gap of these materials comes with the unique feature of a tunable absorption edge. The wavelength of the band edge varies from 365 to 200 nm (Ref. 2) as the Al composition changes from 0% to 100%, which makes the device visible blind or even solar blind. One interesting application for the high-energy-density–physics and inertial confinement fusion (ICF) communities would be to detect Thomson scattering in a plasma, where the probe light must be at a frequency higher than the plasma frequency.[3] Currently UV probes at 263 nm and 210 nm are being considered for these applications but semiconducting detectors in this region of the spectrum are typically slow and inefficient.

MSM photodetectors based on AlGaN, however, have been commonly reported to have extremely long decay times and high dark currents[4,5] because of the poor material quality and high defect density. Recently, we successfully fabricated detectors on high-quality AlGaN wafers. The detectors had an ultrafast response time. To our knowledge, these are the fastest UV detectors fabricated on AlGaN thin films. To resolve the response time, the detectors were tested with single-shot, high-bandwidth oscilloscopes. This is the same configuration in which these devices would be used if they were employed in ICF experiments.

The intrinsic, n-type and p-type AlGaN wafers used to fabricate the devices were purchased from Kyma Technologies.[6] The ~330 nm-thick AlGaN thin films were grown on sapphire by metal–organic chemical vapor deposition (MOCVD). All of the wafers had an approximately 10% Al composition. A thin layer (~10 nm) of AlN was inserted between the substrate and the AlGaN. Acting as a buffer layer, the AlN thin film decreases the lattice constant mismatch between the AlGaN layer and the Al_2O_3 substrate, significantly reducing the density of defects and improving the quality of the materials.

The devices were designed with an interdigited finger-shaped structure. The finger width and spacing were set the same at 5 μm and the active area was 50×50 μm^2. In this work, the devices were fabricated in the Integrated Nanosystems Center (URnano) at the University of Rochester. A 120-nm-thick platinum layer was chosen for the metal contact because platinum has a high work function and has been reported to form good-quality Schottky contacts on AlGaN thin films.[7–9] A 10-nm-thick titanium layer was deposited before metallization to improve the adhesion between the platinum and semiconductor. The device fabrication involved a two-layer fabrication process and precise interlayer alignment. For some devices, the first-layer fabrication deposited a 10-nm insulating layer of SiO_2 within the compensation pad area (without covering the interdigited area). The purpose of the

insulation layer was to reduce the dark current leakage from the compensation pad to the AlGaN thin film. Then, for all devices, the fabrication process deposited a metal contact that covered both the compensation area and portions of the finger-shaped area.

An ORIGAMI femtosecond laser (λ = 1053 nm with 200-fs duration) from NKT Photonics served as the main oscillator for the laser system. A single pulse from the 80-MHz pulse train was selected at a 5-Hz repetition rate by an acoustic-optic modulator and injected into an in-house–built regenerative (regen) amplifier.[10] After the regen amplifier, ~1 mJ of IR light with a FWHM of 10 ps, caused by gain-bandwidth broadening in the regen amplifier, was converted to 263 nm using nonlinear beta-barium borate crystals. The 263-nm beam with a 10-ps duration and 5-Hz repetition rate was used to test the photodetectors. We used both a 45-GHz, single-shot LeCroy oscilloscope and a 12.5-GHz Tektronix oscilloscope. When the 45-GHz oscilloscope was available, it was used in single-channel mode to access the highest digitizing rate. Otherwise, both the signal and reference signal, derived by splitting off a portion of the light and illuminating a GaAs photodiode, were acquired on the 12.5-GHz oscilloscope. The slow GaAs photodiode was used to account for fluctuations in the laser intensity. For each acquired oscilloscope trace, a portion of the trace ~100 ps wide around the peak was fitted with a Gaussian function to determine the measured FWHM, τ_{measure}.

The measurement system, including the oscilloscope, cable, transmission line-mounting fixture, and the incident laser, can cause pulse broadening in the acquired signal. The FWHM that we measured is not the intrinsic response time of our MSM detector but instead is the quadrature sum of the laser pulse width, the intrinsic response of the detector, the response of the measurement system, and the broadening effect of the measurement cable, which can be expressed in the following equation:

$$\tau_{\text{measure}} = \sqrt{\tau_{\text{intrinsic}}^2 + \tau_{\text{oscilloscope}}^2 + \tau_{\text{cable}}^2 + \tau_{\text{laser}}^2 + \tau_{\text{circuit}}^2}. \tag{1}$$

For the LeCroy oscilloscope, $\tau_{\text{oscilloscope}}$ is 7.8 ps. The pulse width of the laser, τ_{laser}, is 10 ps. To evaluate the broadening effect caused by the measurement circuit, a *SPICE* simulation[11] was carried out on the circuit we used for the testing. The circuit produced a FWHM of 16.9 ps with a 10-ps pulse impulse response. Therefore, the pulse broadening that the circuit could cause, τ_{circuit}, is calculated to be 13.6 ps. The cable response τ_{cable} was measured to be 22.5 ps. The measured FWHM of the signal from the AlGaN detector, as shown in Fig. 1, is 36 ps. Based on these assumption and measurements listed above, the intrinsic response of these devices is 24 ps.

We further investigated the response behavior of the detectors under different bias voltages. We changed the bias voltage from –30 V to 30 V with a B&K Precision DC Power Supply 1635, and the detector illumination remained unchanged during the test. The peak voltages under different bias voltages are plotted in Fig. 2. Clearly the detector never reached saturation, where the peak voltage was independent of the applied bias. This is unexpected behavior and may be caused by the photogenerated carri-

Figure 1

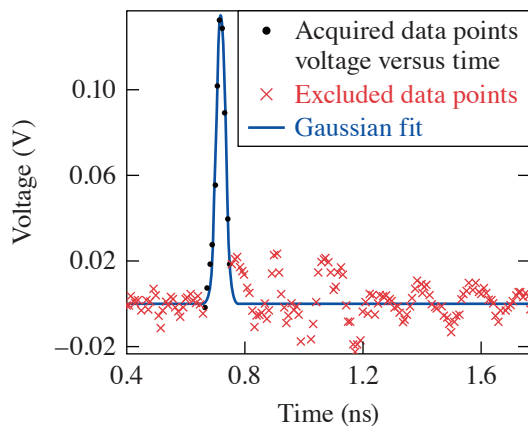The response curve of the device with platinum contact fabricated on an n-type doping wafer. The finger spacing and finger width of the device are both 5 μm and the SiO$_2$ insulating layer is 10 nm thick. The signal is taken at a bias voltage of 15 V and a pulse energy of 52 nJ. The Gaussian fit is also plotted, while the other data points marked by red ×'s are excluded from the fit.
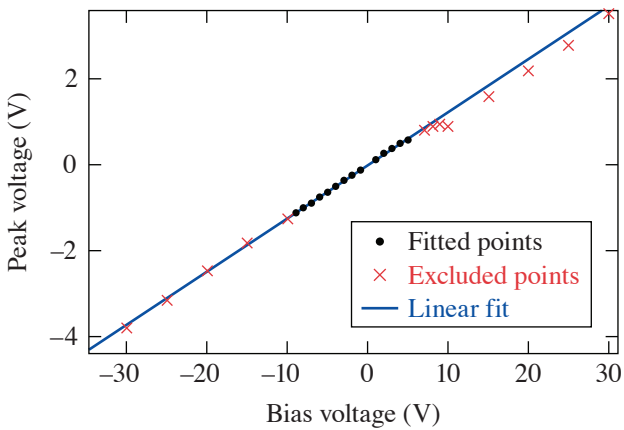
E28694JR

Figure 2

The peak voltage of the photodetector response under different bias voltages from –30 V to 30 V. A linear fit was made based on the data under lower biased voltage; the red ×'s points are the excluded high-voltage biased points.

E28696JR

ers recombining before being swept to the metal contact. As the electric field increases, the velocity of the carriers increases and more carriers reach the contact before recombining, thereby causing the peak voltage to continue to increase. Normally the peak signal is determined solely by the number of photogenerated carriers and is independent of the voltage. Since the photogenerated signal never reached the saturated regime, the responsivity could not be calculated. Further experiments are ongoing to determine the origin of the voltage dependence of the photo signal.

1. J. C. Carrano *et al*., Appl. Phys. Lett. **73**, 2405 (1998).

2. D. Walker *et al*., Appl. Phys. Lett. **74**, 762 (1999).

3. R. K. Follett *et al*., Rev. Sci. Instrum. **87**, 11E401 (2016).

4. Y. Zhao and W. R. Donaldson, J. Mater. Res. **33**, 2627 (2018).

5. Y. Zhao and W. R. Donaldson, IEEE Trans. Electron Devices **65**, 4441 (2018).

6. Kyma Technologies Inc., Raleigh, NC 27617.

7. P.-C. Chang *et al*., Thin Solid Films **498**, 133 (2006).

8. M. Brendel *et al*., Electron. Lett. **51**, 1598 (2015).

9. Y.-R. Jung *et al*., Jpn. J. Appl. Phys. **42**, 2349 (2003).

10. A. V. Okishev and J. D. Zuegel, Appl. Opt. **43**, 6180 (2004).

11. L. W. Nagel and D. O. Pederson, *SPICE (Simulation Program with Integrated Circuit Emphasis)*, EECS Department, University of California, Berkeley, Technical Report No. UCB/ERL M382 (1973).

High-Energy Parametric Amplification of Spectrally Incoherent Broadband Pulses

C. Dorrer, E. M. Hill, and J. D. Zuegel

Laboratory for Laser Energetics, University of Rochester

Large-aperture Nd:glass amplifiers that are the basis for solid-state, ignition-class laser drivers are intrinsically limited in terms of their amplification bandwidth.[1,2] Spectral gain narrowing typically reduces the optical bandwidth to a few nanometers at a central wavelength of 1053 nm (1ω), mere tenths of a percent in terms of fractional bandwidth $\Delta\omega/\omega_0$. This relatively narrow optical bandwidth limits the performance of beam-smoothing techniques used to generate a smooth, time-averaged focal spot on target. Larger fractional bandwidth of the order of 1% would decrease the asymptotic smoothing time and mitigate laser–plasma instabilities.[3] Simulations show that this bandwidth promises to vastly improve the performance of both direct- and indirect-drive inertial confinement fusion. A new broadband laser driver concept based on optical parametric amplifiers (OPA's) is being designed at LLE to deliver 3ω pulses with a fractional bandwidth greater than 1% and support experiments on the OMEGA laser. Concepts for broadband amplification and frequency conversion of spectrally incoherent pulses are being tested and compared to models.

Optical parametric amplifiers, based on a three-wave nonlinear interaction, can efficiently amplify signals over extremely large bandwidths when the wavelength-dependent phase mismatch between the high-energy pump pulse, signal to be amplified, and resulting idler wave remains small during propagation in the nonlinear crystal.[4] These amplifiers are typically used to amplify a spectrally coherent signal for which spectral components have a well-defined phase relationship, e.g., with a chirped signal in optical parametric chirped-pulse amplification (OPCPA).[5] Smoothing techniques are, however, more effective when the temporal variations of the instantaneous optical frequency are much faster than the overall pulse duration. This can be achieved, for example, with spectrally incoherent pulses originating from a random process such as amplified spontaneous emission. While these signals are effectively used in large-scale, high-energy excimer (gas) lasers,[6] demonstrating their broadband amplification in OPA's pumped by frequency-doubled lasers based on Nd-doped materials opens the path to a new generation of broadband, high-energy, ignition-class drivers based on existing solid-state laser technology and large-aperture nonlinear crystals.

We demonstrate, for the first time to our knowledge, efficient high-energy parametric amplification of broadband spectrally incoherent pulses. Because of the spatial coherence resulting from signal generation in a front end based on single-mode fibers, the amplification process is similar to what is observed with monochromatic signals. Experiments performed with the existing Multi-Terawatt laser's OPA stages, originally designed for OPCPA,[7] demonstrate the generation of spectrally incoherent waves around 1053 nm (1ω) with ~60-nm bandwidth at energies of several hundred millijoules. The large bandwidth and high conversion efficiency from the pump at 526.5 nm (2ω) to 1ω waves are the results of a collinear interaction geometry in the last OPA and generation of the seed signal at a central wavelength below 1053 nm by the fiber front end. In these conditions, the idler wave generated in the last OPA co-propagates with the signal wave and has a spectrum that is spectrally symmetric relative to the signal's spectrum with respect to 1053 nm, effectively increasing the available energy and optical bandwidth at 1ω.

Figure 1 displays the output 1ω energy after the power amplifier as a function of the 2ω pump energy. Similar amplification behavior is observed when the seed signal is a spectrally incoherent broadband signal, with the spectrum centered at 1030 nm, and a narrowband coherent signal at 1030 nm [Fig. 1(a)]. The energy in the combined signal and idler waves resulting from power-
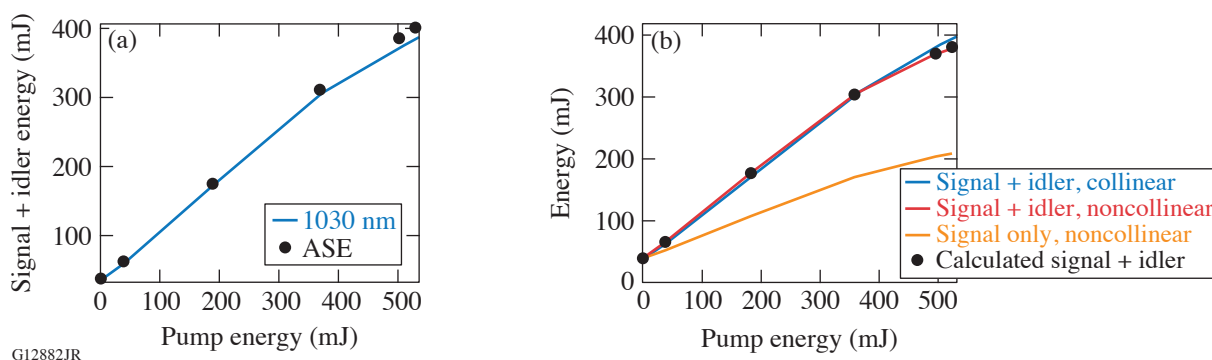
Figure 1
Amplified output energy after the power amplifier. (a) The curve corresponds to a monochromatic seed at 1030 nm and the solid black circles correspond to a spectrally broadband amplified spontaneous emission (ASE) seed. (b) The measured power-amplifier output energy is plotted for the combined signal and idler in collinear and noncollinear geometries (solid blue and red curves, respectively) and for the signal in a noncollinear geometry (solid orange curve). The energy of the combined signal and idler calculated from the signal energy is plotted with solid black circles.

amplifier operation at 530 mJ is 400 mJ, demonstrating a 70% conversion efficiency from the 2ω pump to 1ω waves considering the 30-mJ, 1ω input energy for this amplifier. Operation of the power amplifier in a collinear or slightly noncollinear geometry yields similar output energies for the combined signal and idler pulses [Fig. 1(b)]. The energy of the combined signal and idler waves calculated using the signal energy measured in a noncollinear geometry is in excellent agreement with the experimentally measured energy, showing that parasitic processes such as second-harmonic generation are not significant.[8]

The spectrum of the parametric fluorescence resulting from operation of the fully pumped OPA stages without a seed signal is shown in Fig. 2(a). The measured bandwidth, ~100 nm, is indicative of the large bandwidth that can be obtained for amplification around 1ω. Figure 2(b) shows the spectrum of the input seed signal and the spectrum of the combined signal and idler waves at the output. Because of energy conservation in the OPA pumped at 526.5 nm, amplification of signal photons at wavelengths below 1053 nm leads to the generation of idler photons at wavelengths above 1053 nm. The resulting waves have a spectral density extending over more than 60 nm, i.e., corresponding to a fractional bandwidth larger than 5% at 1ω.
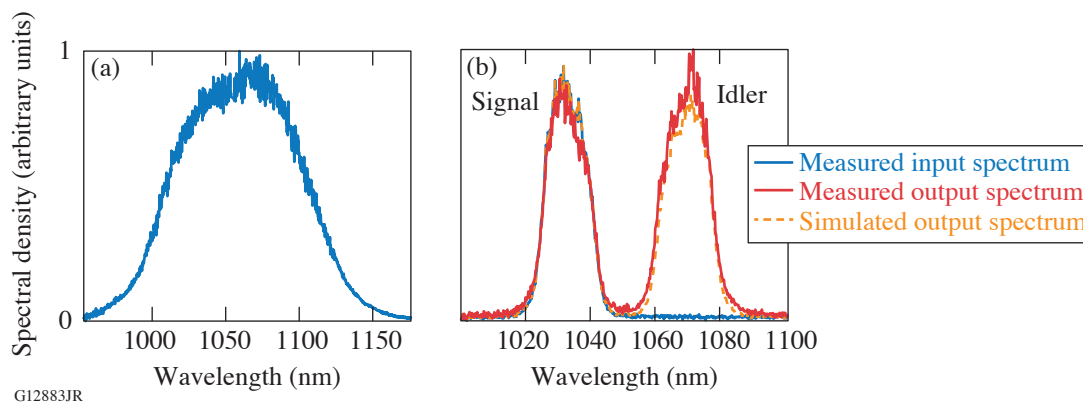
Figure 2
(a) Measured parametric fluorescence at the power-amplifier output in the absence of seed in the preamplifier; (b) input and output spectra of the power amplifier and simulated output spectrum for the ASE seed.

1. C. A. Haynam *et al.*, Appl. Opt. **46**, 3276 (2007).

2. J. L. Miquel, C. Lion, and P. Vivini, J. Phys.: Conf. Ser. **688**, 012067 (2016).

3. R. K. Follett *et al.*, Phys. Plasmas **26**, 062111 (2019).

4. G. Cerullo and S. De Silvestri, Rev. Sci. Instrum. **74**, 1 (2003).

5. I. Jovanovic *et al.*, Appl. Opt. **41**, 2923 (2002).

6. S. Obenschain *et al.*, Appl. Opt. **54**, F103 (2015).

7. V. Bagnoud *et al.*, Opt. Lett. **30**, 1843 (2005).

8. J. Bromage *et al.*, Opt. Express **19**, 16,797 (2011).

A Laser System Model for Enhanced Operational Performance and Flexibility on OMEGA EP

M. J. Guardalben, M. Barczys, B. E. Kruschwitz, M. Spilatro, L. J. Waxer, and E. M. Hill

Laboratory for Laser Energetics, University of Rochester

Introduction

The ability of high-energy laser systems to provide complex laser pulse shapes has growing importance in many research disciplines such as laser fusion,[1–4] high-energy-density physics,[5–8] laboratory astrophysics,[9–11] and laser conditioning of optical materials.[12] For example, x-ray diffraction of ramp-compressed crystalline solids can probe high-pressure phase transitions inaccessible with shock compression.[6] In such laser facilities, accurate, real-time predictions of laser performance are critical for maximizing experimental and operational effectiveness and flexibility. Several laser operations models that predict laser performance for high-energy laser systems have been reported.[13–22] Most of these models utilize optimization methods that comprise forward-propagation simulations with feedback to converge on the required on-target pulse power. This article reports on *PSOPS*—a MATLAB[23]-based semi-analytic model developed for the OMEGA EP[24] Laser System. *PSOPS* provides rapid and accurate predictions of OMEGA EP Laser System performance in both forward and backward directions, a user friendly interface, and rapid optimization capability between shots. The model's features have allowed real-time optimization of the laser system configuration in order to satisfy the demands of rapidly evolving experimental campaign needs and have enabled several enhancements to the accuracy and flexibility of laser system performance.

Functional Overview of *PSOPS*

The backward simulation capability of the model is used in the configuration of the system for a shot where the desired UV energy, pulse shape, expected beam profile, and beamline amplifier configuration are provided as inputs to the *PSOPS* model. The results are the required pulse shape at the input of the system, as well as the energies at each stage of the laser, from which the laser throttles and diagnostic configurations can be determined in a fast and robust manner.

During shot operations, *PSOPS* is used in the forward simulation direction to provide rapid predictions of laser-system performance using measured inputs to the amplifier chain. The measured input beam profile and real-time–measured input pulse shape are used with the expected beamline injected energy and previously measured beamline small-signal gain to predict the IR and frequency-converted UV performance at the end of the beamline. A front-end qualification shot is taken at the start of a shot day to confirm the expected injected energy and to measure the injected beam near-field distribution that is used as input to the *PSOPS* model.

Laser pulse shape, energy, and near-field beam profile are measured at several locations along the beam path. Diagnostic stages relevant to the *PSOPS* model and associated measurements are shown in Fig. 1. The output pulse shape of each beamline's regenerative amplifier is measured at a 5-Hz repetition rate using a photodiode-based pulse-stacking, pulse-shape monitor (PSM).[25] Calorimetrically calibrated charge-coupled–device (CCD) cameras (Scientific Instruments, model SI-800) are used to measure the beam's near-field profile and laser-beam energy at the beamline injection and amplified beamline output stages. A harmonic energy diagnostic (HED)[26] is used to measure the UV energy and the residual green and IR energy of the frequency-converted laser beam. Amplified IR and UV pulse shapes are measured using ROSS streak cameras.[27] These diagnostic measurements are used to calibrate the *PSOPS* model and also to determine the required stage energies and pulse shapes in both forward and backward directions when configuring for a shot.
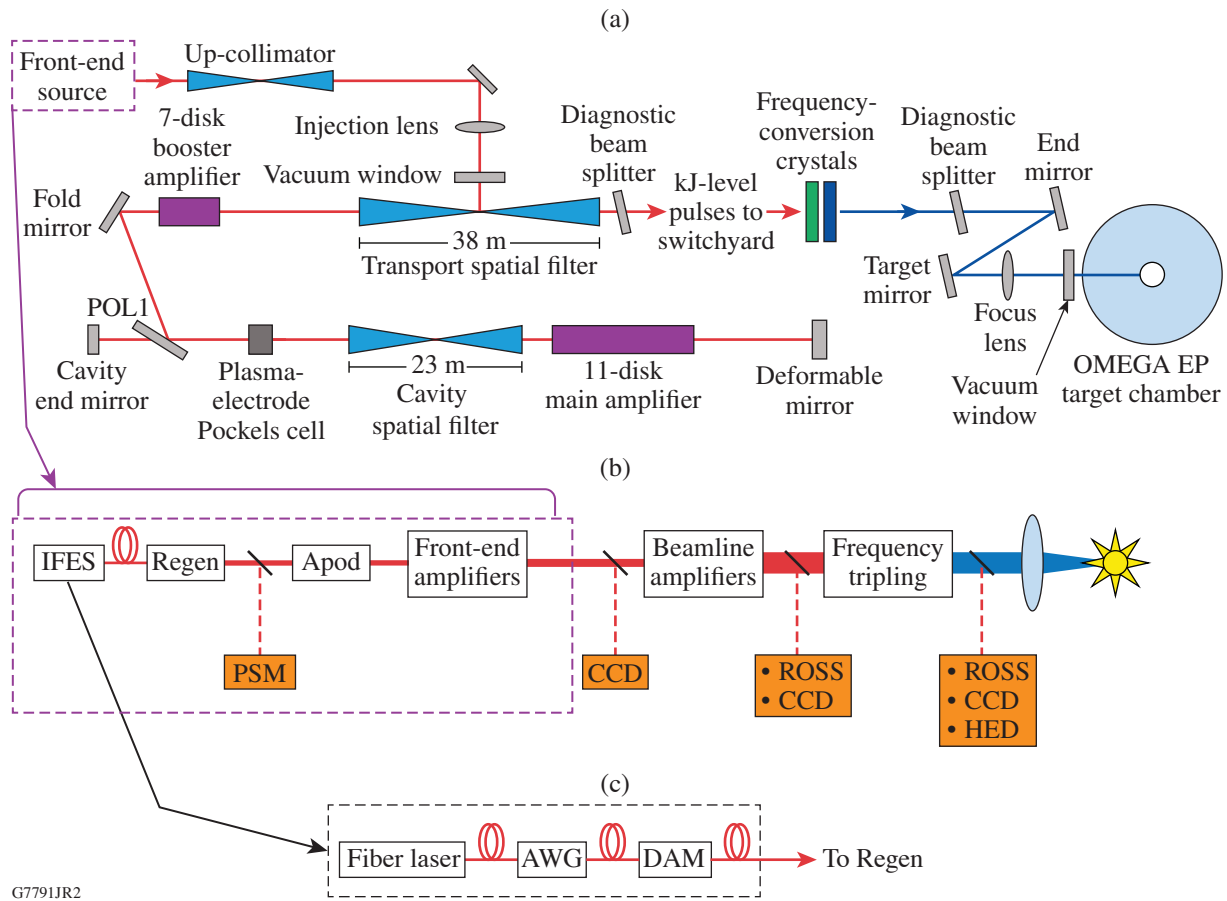
G7791JR2

Figure 1

(a) Configuration of an OMEGA EP beamline. (b) Block diagram of (a) showing locations of pulse-shape, beam-profile, and energy-measurement diagnostics used with the *PSOPS* model. PSM: pulse-shape monitor; Apod: beam-shaping apodizer; CCD: near-field charge-coupled–device camera; ROSS: Rochester optical streak system; and HED: harmonic energy diagnostic. (c) An integrated front-end system (IFES) produces temporally shaped, 1053-nm pulses from a single-frequency, continuous-wave (cw) fiber laser. Precisely shaped temporal pulses are formed using an arbitrary waveform generator (AWG) that drives a dual-amplitude modulator (DAM).

PSOPS Model Description

Analytic solutions to the four-level, coupled-rate, and energy-transport equations for a homogeneously saturating thin slab[28] are used in *PSOPS* to determine the time-dependent gain within each LHG-8, Nd-doped laser disk at discrete locations across the laser aperture. For multipass amplification in the forward propagation direction, the output intensity of disk k is given by

$$I_k(t,x,y) = \beta^2 \cdot G_k(t,x,y) I_{k-1}(t,x,y),\tag{1}$$

where

$$G_k(t,x,y) = \frac{1}{1 - \left\{1 - \left[G_0(x,y)\right]^{-1}\right\}\exp\left[-F_k(t,x,y)/F_{\mathrm{sat}}\right]},\tag{2}$$

$$F_k(t,x,y) = \int_{t_0}^{t} \beta \cdot I_{k-1}(t',x,y)\mathrm{d}t',\tag{3}$$

where G_0 is the small-signal gain of the laser disk, F_{sat} is the saturation fluence, and a per-disk-surface loss factor β is included in the model to account for passive losses. The integral in Eq. (3) is taken in the frame of the laser pulse from the starting time of the pulse, t_0, up to the time t within the pulse. Following the repeated application of Eqs. (1)–(3) through the entire beamline, frequency conversion to the third harmonic uses look-up tables from *MIXER* calculations.[29,30] For backward prediction starting with the UV beam profile, pulse shape, and energy, these tables provide the amplified IR intensity at the end of the beamline from which the beamline input intensity is recursively calculated using Eqs. (4)–(6):

$$I_k(t,x,y) = I_{k+1}(t,x,y)\Big/\beta^2 \cdot G_k(t,x,y),$$
(4)

$$G_k(t,x,y) = 1 + \big[G_0(x,y) - 1\big]\exp\big[-F_k(t,x,y)\big/F_{sat}\big],$$
(5)

$$F_k(t,x,y) = \int_{t_0}^{t}\big[I_{k+1}(t',x,y)\big/\beta\big]dt',$$
(6)

where $I_k(t,x,y)$ is the *input* intensity of the kth disk. The effective saturation fluence of the OMEGA EP beamline has been inferred from prior fits to gain-saturation data and takes into account an inhomogeneous broadening effect in the laser glass[31] and bottle-necking of the terminal level of the lasing transition for pulse widths close to the terminal-level lifetime τ_{10}, where $\tau_{10} \sim 0.25$ ns for Nd-doped phosphate laser glasses.[32,33]

Comparison of Experimental and Model Data

Spatial and temporal simulations in both forward and backward directions are in excellent agreement with measurements, as shown in Figs. 2 and 3.
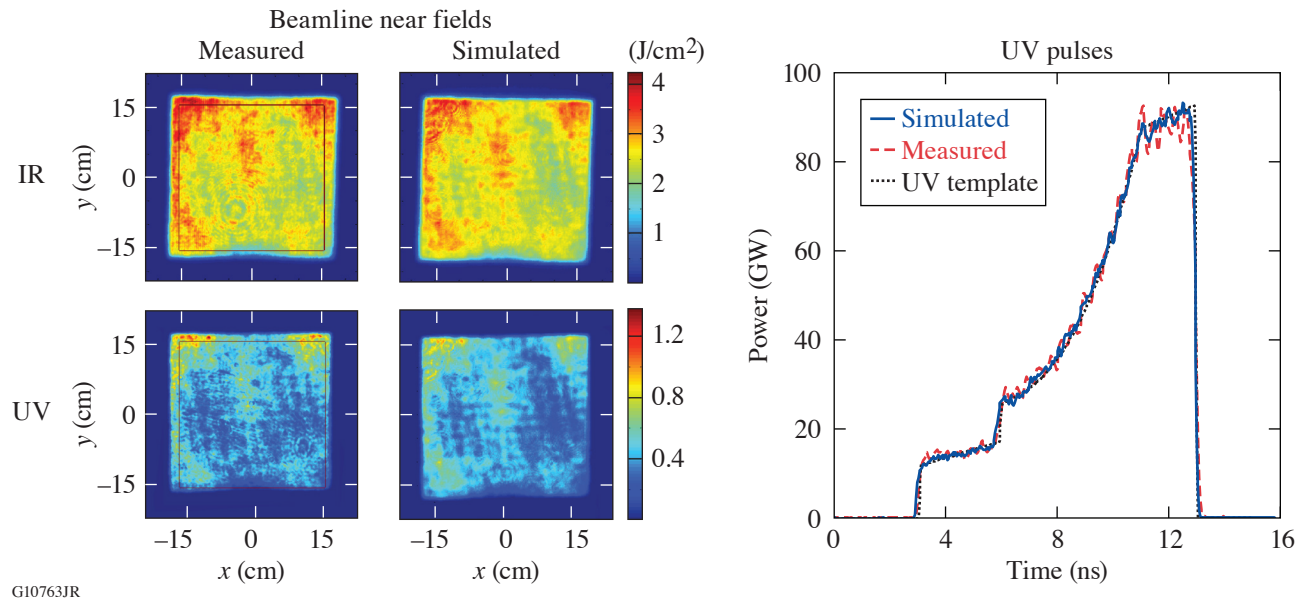

G10763JR

Figure 2

Comparison of *PSOPS* forward-simulated beam near fields, pulse shapes, and corresponding energies with measurements for Beamline 3, shot 20678. The forward simulation used the measured injected beam profile, pulse shape, and energy for shot 20678. IR: 3112 J measured; 3102 J simulated. UV: 453 J measured, 452 J simulated.

G12871JR
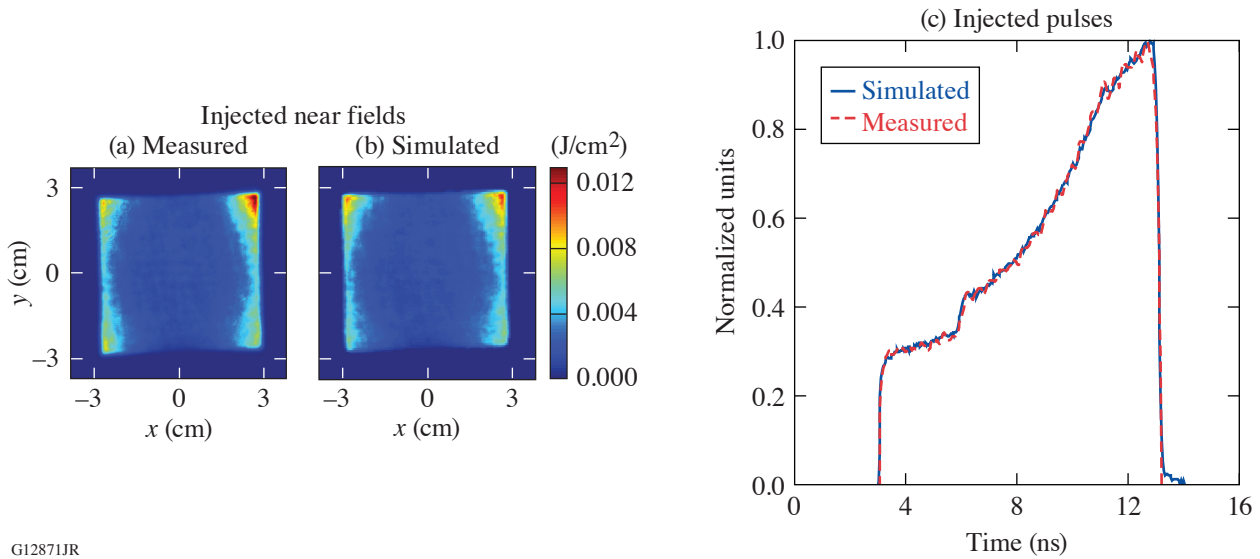
Figure 3

Comparison of *PSOPS* backward-simulated injected near-field beam profile, pulse shape, and energy with measurements for Beamline 3, shot 20678: (a) 79.5 mJ measured and (b) 76.9 mJ simulated. The backward simulation used the measured UV beam, pulse shape, and energy.

OMEGA EP Enhancements Enabled by *PSOPS*

1. Improvements to UV Energy and Pulse-Shape Accuracy

Drifts in system performance can lead to noticeable deviations between simulated and achieved pulse shapes and energies, which can be minimized with an agile system model such as *PSOPS*. For example, Fig. 4 shows how the injected pulse shape can be optimized for small changes in system performance. Figure 4(a) shows a pre-shot prediction on shot day that departs from the ideal pulse shape near the end of the pulse. Based on this prediction, the input pulse shape was modified to provide the compensated pre-shot prediction shown in Fig. 4(b). The post-shot UV simulation showed excellent agreement with the measurement [Fig. 4(c)].

G10757JR

Figure 4

Predicted and requested UV pulse shapes showing how day-to-day changes in laser system performance are compensated using *PSOPS* predictions: (a) initial; (b) compensated; and (c) post-shot UV pulse simulation and measurement. On-target UV energy: 775 J requested, 751 J measured, 752 J simulated.

2. Improvements to Experimental Flexibility

PSOPS has also enhanced laser facility flexibility by enabling users to adjust requested UV pulse shapes and energies between laser shots, within a predefined range that is determined uniquely for each experimental campaign. The allowed range of energy and pu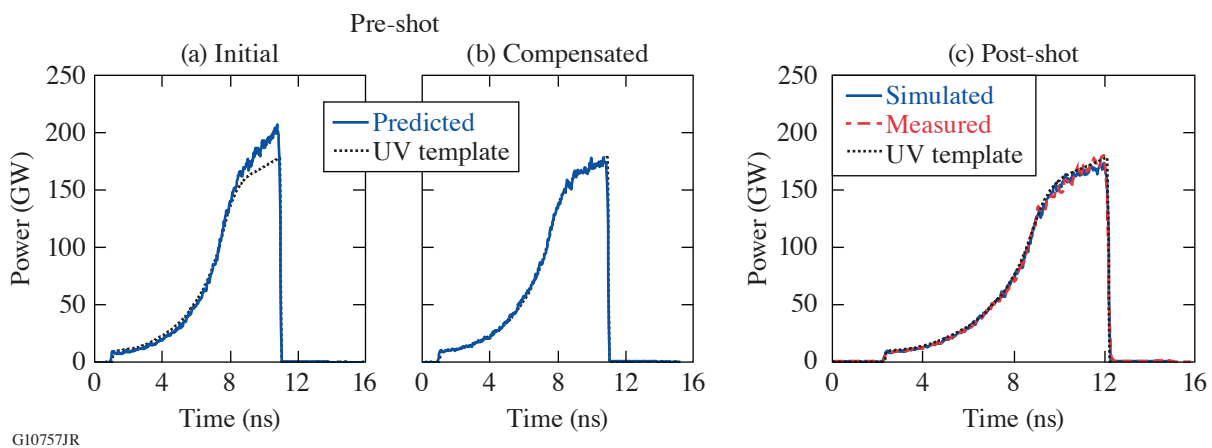lse-shape modification is assessed with respect to the laser system's fluence limits, the range of energy and pulse shapes planned for the day, and the likelihood of maintaining each beamline's 90-min shot cycle. In the example shown in Fig. 5, different energies were desired while maintaining the original normalized design pulse shape that produced 500 J of UV on-target energy. This request was accommodated in each case by adjusting the front-end pulse shape and throttles per the *PSOPS* pre-shot prediction.

G10758JR2
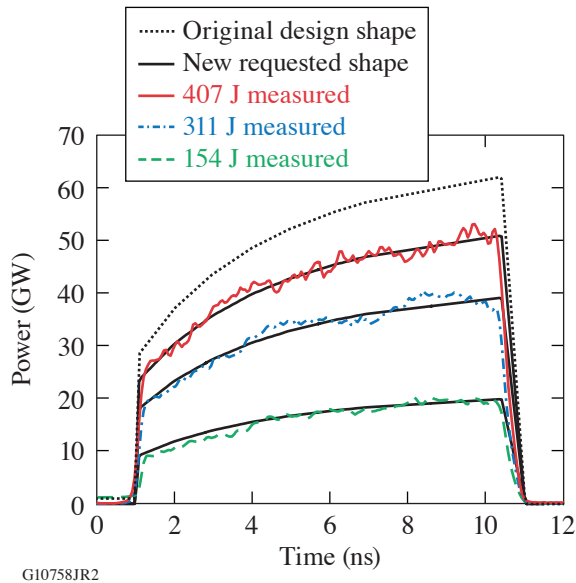
Figure 5
Example showing facility flexibility enabled by *PSOPS*. Based on a user's real-time analysis of experimental data, different energies were requested while maintaining the original normalized design pulse shape that produced 500-J on-target energy. The measured UV on-target energies are shown in the label.

3. Increased Effective Pulse-Duration Range

Currently, OMEGA EP can accommodate single-beamline pulse widths of up to 10 ns. However, improved system modeling in conjunction with precision timing allow the technique of pulse stitching to achieve up to a 4× increase in effective pulse duration. With pulse stitching, as illustrated in Fig. 6, pulse shapes from different beamlines can be precisely combined on target to form

G12943JR
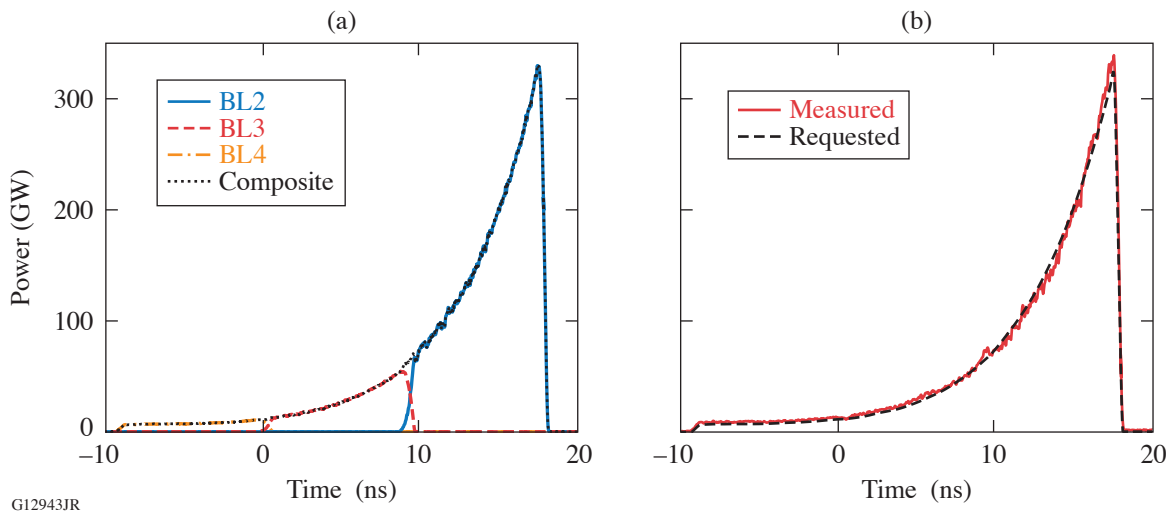
Figure 6
(a) Pre-shot prediction and (b) post-shot measurement of approximately 27-ns composite pulse shape formed by incoherent addition of the individual beamline pulse shapes and beam-to-beam timing (shot 31182).

a single composite pulse shape. In Fig. 6, the composite 27-ns ramped pulse shape shown was formed by incoherent addition of the individual pulses, separated by the temporal delay between them. Prior to the shot, *PSOPS* is used to predict the composite pulse given the specified beam-to-beam temporal delay [Fig. 6(a)]. The measured composite pulse shown in Fig. 6(b) was formed using the individual-beamline pulse-shape measurements and the measured beam-to-beam UV pulse timing.

4. Improved System Alignment

PSOPS has been used as a tool to optimize the alignment of beam-shaping apodizers[34] in the beamline front end. *PSOPS* predictions of the effect of small changes in beam centering and rotation on the amplified near-field beam uniformity can be used as a guide in the optimization of the apodizer alignment without requiring amplified shots. This has resulted in a better understanding of required tolerances for centering and rotation of both the beam-shaping apodizer and the apodized injected beam with respect to the gain profile of the beamline. As an example, Fig. 7 shows the measured effect that identifying and correcting a small error in apodizer alignment has on the amplified IR near-field beam. Using the measured injected near-field beam, *PSOPS* forward simulations were used to predict the amplified beamline output near-field profile and to correct the apodizer's alignment with respect to the gain profile of the beamline within a 10-min shot cycle. A 0.49-mm shift of the apodizer resulted in significantly improved beamline output near-field contrast and peak-to-mean fluence, as shown in Fig. 7(b). Contrast is defined as the standard deviation of the fluence divided by the mean fluence value. By limiting near-field beam fluence, fluence-limited damage may be avoided, leading to enhanced energy performance. In addition, these simulations have demonstrated that small adjustments to apodizer alignment are often sufficient to correct near-field beam nonuniformity in lieu of designing and manufacturing new apodizers.
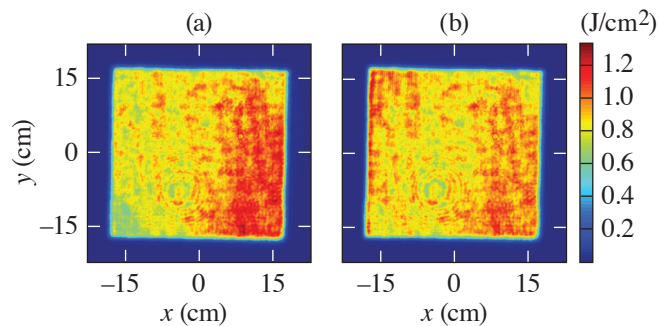
Figure 7
Measured Beamline 3 amplified IR output near-field profile (a) before moving the beam-shaping apodizer (contrast = 13.1%, peak-to-mean = 1.46:1) and (b) after moving the apodizer by 0.49 mm (contrast = 9.4%, peak-to-mean = 1.43:1). Contrast is defined in the text. The apodizer adjustment was guided by *PSOPS* simulations.

G12875JR

Summary

PSOPS is a semi-analytic model that is used on OMEGA EP to predict pulse shapes, stage energies, and near-field beam profiles in both forward and backward directions and has enabled accurate and rapid optimization of the laser system's performance within a small fraction of the OMEGA EP 90-min shot cycle. *PSOPS* is the key enabler of an automated capability to compute and specify the laser system's stage energies and corresponding system configurations prior to each OMEGA EP shot based upon evolving on-target pulse shape and energy requirements. The ability to calibrate the model between laser shots accounts for day-to-day system drifts without loss of shot time. Several facility enhancements have been enabled by *PSOPS*, such as improvements to UV energy and pulse-shape accuracy, improvements to experimental flexibility, increased effective pulse-duration range, and improved system alignment. An upgrade to the model currently in progress accounts for the spectral dependence of beamline gain and saturation fluence for shots that require spectrally tunable UV on-target irradiation to mitigate cross-beam energy transfer.[35]

1. S. X. Hu *et al.*, Phys. Plasmas **25**, 082710 (2018).

2. D. Cao *et al.*, Phys. Plasmas **25**, 052705 (2018).

3. J. Trela *et al.*, Phys. Plasmas **25**, 052707 (2018).

4. A. Bose *et al.*, Phys. Plasmas **25**, 062701 (2018).

5. M. Millot *et al*., Nature **569**, 251 (2019).

6. D. N. Polsin *et al*., Phys. Plasmas **25**, 082709 (2018).

7. D. N. Polsin *et al*., Phys. Rev. Lett. **119**, 175702 (2017).

8. M. C. Gregor *et al*., Phys. Rev. B **95**, 144114 (2017).

9. D. E. Fratanduono *et al*., Phys. Rev. B **97**, 214105 (2018).

10. R. F. Smith *et al*., Nat. Astron. **2**, 452 (2018).

11. F. Coppari *et al*., Nat. Geosci. **6**, 926 (2013).

12. K. R. P. Kafka, S. Papernov, and S. G. Demos, Opt. Lett. **43**, 1239 (2018).

13. M. J. Shaw *et al*., Opt. Eng. **43**, 2885 (2004).

14. M. J. Shaw *et al*., Proc. SPIE **5178**, 194 (2004).

15. R. A. Sacks *et al*., J. Phys.: Conf. Ser. **112**, 032024 (2008).

16. M. Shaw *et al*., J. Phys.: Conf. Ser. **112**, 032022 (2008).

17. D. I. Hillier, D. N. Winter, and N. W. Hopps, Appl. Opt. **49**, 3006 (2010).

18. B. J. Le Garrec and O. Nicolas, J. Phys.: Conf. Ser. **112**, 032019 (2008).

19. D. Hu *et al*., Chin. Opt. Lett. **13**, 041406 (2015).

20. K. T. Vu *et al*., Opt. Express **14**, 10,996 (2006).

21. W. Shaikh *et al*., *Central Laser Facility Annual Report 2005/2006*, 199, Rutherford Appleton Laboratory, Chilton, Didcot, Oxon., England (2005).

22. K. P. McCandless *et al*., in *Proceedings of the 14th International Conference on Accelerator & Large Experimental Physics Control Systems (ICALEPCS 2013)*, edited by C. Marshall, J. Fisher, and V. R. W. Schaa (The Joint Accelerator Conferences Website, Geneva, Switzerland, 2014), pp. 1426–1429.

23. MATLAB® R2013b, The MathWorks Inc., Natick, MA 01760-2098.

24. J. H. Kelly *et al*., J. Phys. IV France **133**, 75 (2006).

25. J. R. Marciante, W. R. Donaldson, and R. G. Roides, IEEE Photonics Technol. Lett. **19**, 1344 (2007).

26. *LLE Review Quarterly Report* **63**, 110, Laboratory for Laser Energetics, University of Rochester, Rochester, NY, LLE Document No. DOE/SF/19460-91 (1995).

27. W. R. Donaldson *et al*., Rev. Sci. Instrum. **73**, 2606 (2002).

28. A. E. Siegman, in *Lasers* (University Science Books, Mill Valley, CA, 1986), Chap. 10.

29. R. S. Craxton, Opt. Commun. **34**, 474 (1980).

30. R. S. Craxton, IEEE J. Quantum Electron. **QE-17**, 1771 (1981).

31. D. M. Pennington, D. Milam, and D. Eimerl, Proc. SPIE **3047**, 630 (1997).

32. C. Bibeau, J. B. Trenholme, and S. A. Payne, IEEE J. Quantum Electron. **32**, 1487 (1996).

33. C. Bibeau and S. A. Payne, 119, Lawrence Livermore National Laboratory, Livermore, CA, Report UCRL-LR-105820-95 (1996).

34. C. Dorrer and J. Hassett, Appl. Opt. **56**, 806 (2017).

35. B. E. Kruschwitz *et al*., Proc. SPIE **10898**, 1089804 (2019).

Toward the Reduction of Transverse Stimulated Raman Scattering in KDP/DKDP Crystals

H. Huang, T. Z. Kosc, S. G. Demos, and T. J. Kessler

Laboratory for Laser Energetics, University of Rochester

Transverse Raman generation and amplification in KDP/DKDP limit the laser power level in laser fusion systems. To properly understand the propagation and amplification of light in a birefringent crystal, a full vector model of the pump and scattering fields is required. We present a ray-tracing approximation that enables one to calculate the Raman fluence at the surface of an arbitrary crystal and pump polarization configurations. This allows one to determine the optimal configuration that minimizes the fluence peaks at the crystal edge.

Raman photons can be generated by the strong laser field (the pump) in a piece of thin crystal placed perpendicular to the path of the pump (Fig. 1). Depending on the crystal symmetry and orientation, such a signal may have significant accumulated gain when traveling parallel to the plate due to the long length of travel inside the crystal. Such transverse Raman rays have the potential to gain more energy than those parallel to the pump direction that have less distance for amplification.
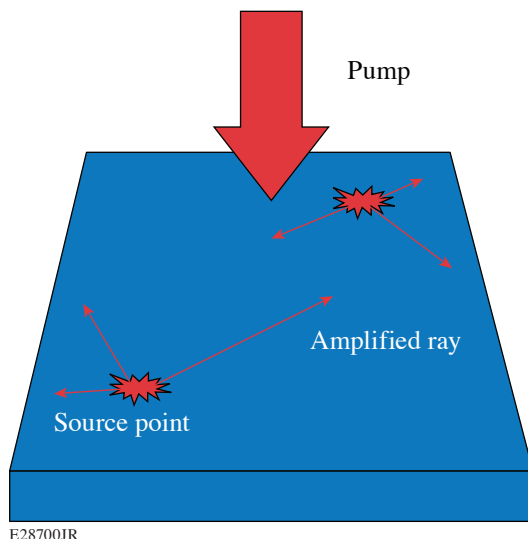
Figure 1
The pump laser excites spontaneous Raman photons in a laser crystal. The Raman is amplified as it propagates in the crystal.

E28700JR

The distribution of the transverse stimulated Raman scattering (TSRS) fluence at the crystal surface is not uniform. It depends on the pump laser and crystal configurations. The fluence at a surface point is the sum of all the amplified rays that arrive at this location. To calculate such fluence requires ray tracing of each such ray over the path from the spontaneous emission source point to the surface point. This requires a rigorous treatment of the ray propagating in a birefringence crystal.

The starting point of our modeling is to break each ray into the normal modes of electromagnetic waves, i.e., the o and e polarizations; similarly the pump is also broken into o and e polarizations. The Raman gain can therefore be treated as the combination of interactions between these normal modes.

An efficient code was developed following the picture of basic physics shown in Fig. 2. We were able to calculate the fluence distribution at the crystal surface for any laser and crystal configuration, including the crystal thickness and beveled-edge angle. From these calculations we can estimate the maximum laser intensity without damaging the crystal and mount, providing a guideline for the optimized crystal configuration. For example, in Fig. 3 we can see the worst-case intensity depends on the pump polarization. By selecting the correct crystal cut direction, the worst-case intensity at the crystal plate edge can be reduced.

E28703JR
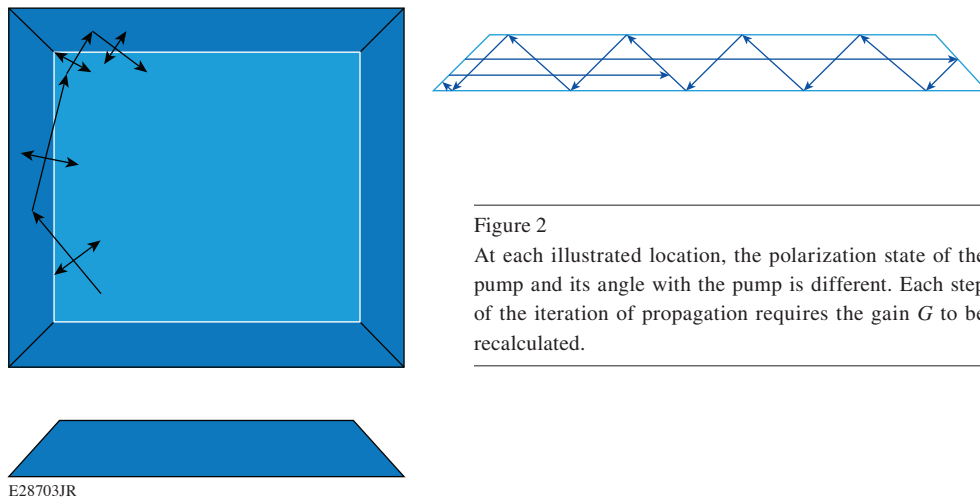
Figure 2
At each illustrated location, the polarization state of the pump and its angle with the pump is different. Each step of the iteration of propagation requires the gain G to be recalculated.

(a)   (b)

Pump polarization

Pump polarization

E28705JR
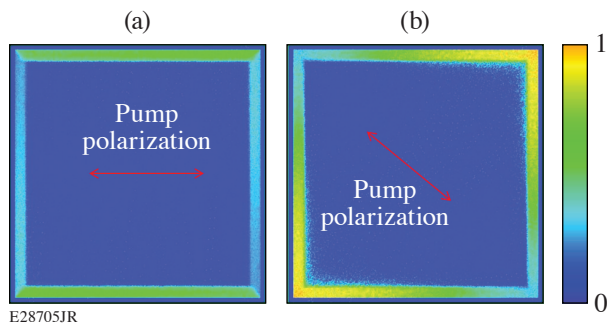
Figure 3
These plots show that the Raman distribution at the crystal surface depends on the pump polarization. (a) Pump polarization normal to the optic axis. (b) Pump polarization at an angle to the optical axis.

In summary, TSRS in laser crystal is a phenomenon we cannot completely avoid but we can find solutions to reduce the worst-case fluence at the crystal edge to avoid component damage. The key to finding such solutions is to distribute the Raman energy incoherently over polarizations and directions. The ray-tracing methods we developed provide a better understanding about how the evolution of polarization states in the crystal affect the TSRS and are a versatile tool to optimizing the design of KDP/DKDP optics including the distributed polarization rotator.

Investigation of Parameters Governing Damage Resistance of Nematic Liquid Crystals for High-Power or Peak-Intensity Laser Applications

T. Z. Kosc, A. A. Kozlov, S. Papernov, K. R. P. Kafka, S. G. Demos, and K. L. Marshall

Laboratory for Laser Energetics, University of Rochester

The damage resistance of saturated and unsaturated liquid crystals (LC's) under a wide range of laser excitation conditions, including 1053-nm pulse durations between 600 fs and 1.5 ns and nanosecond pulse excitation at 351 nm and 532 nm, has been investigated. This multiwavelength investigation probed the correlation between the electronic structure of each material and its laser-induced damage behavior by altering the excitation photon energy. The laser-induced damage threshold at all wavelengths and pulse durations was consistently higher in saturated materials than in their unsaturated counterparts.

The electronic excitation pathways in LC materials are generally known and involve a singlet ground state (S_0) and excited singlet (S_1, S_2,...S_n) and triplet states. The time scale of the transition from the singlet states to the corresponding triplet states during relaxation, or intersystem crossing, is typically >1 ns, which has been confirmed for several unsaturated LC compounds.[1,2] Because the excitation leading to laser-induced damage (breakdown) occurs during the laser pulse, transitions with lifetimes longer that the pulse duration (in our case ~1 ns) have no (or minimal) effect on laser-damage mechanisms. Consequently, we consider only the transitions between the singlet states. The accordingly modified Jablonski energy diagram in Fig. 1 describes the electronic structure in LC materials involving singlet ground state (S_0) and excited singlet (S_1, S_2,...S_n), where the energy levels are defined as multiples of the energy of a 1ω photon used in this study.

	Number of photons required to bridge the lowest excited state S_1		
Wavelength (photon energy)	351 nm (3.35 eV)	527 nm (2.36 eV)	1053 nm (1.18 eV)
Unsaturated	1	2	3
Saturated	2	2	4

G12806JR
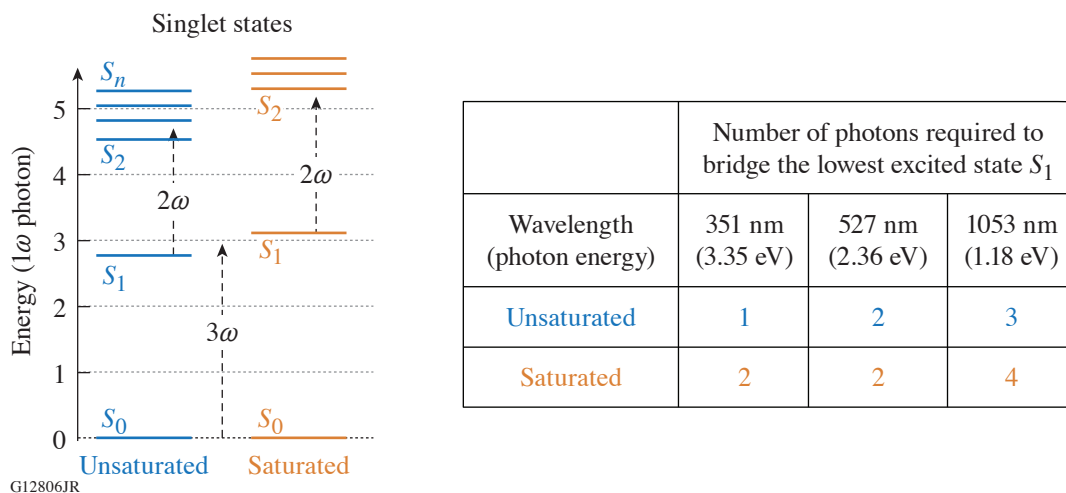
Figure 1
A schematic depiction of the electronic transitions leading to laser-induced breakdown in LC materials is presented by a modified Jablonski energy diagram involving a singlet ground state (S_0) and excited singlet states (S_1, S_2,...S_n). The energy levels are referenced as multiples of a 1053-nm photon (1ω). The UV transmission edge for each material (saturated < 351 nm < unsaturated) provides insight into the order of photon absorption required to bridge the energy gap from $S_0 \longrightarrow S_1$.

The relative difference in the measured laser-induced–damage threshold (LIDT) at different wavelengths is illustrated in Fig. 2 showing the N-on-1 LIDT results for both saturated and unsaturated materials at all wavelengths. Comparison of the 351-nm and 527-nm results shows a difference between LIDT values of ~5× for unsaturated materials and only of ~1.5× for saturated materials. This behavior can be anticipated from the order of absorption required for electrons to undergo the $S_0 \longrightarrow S_1$ transition. Specifically, unsaturated materials require both linear absorption at 351 nm and two photon absorption at 527 nm, while for saturated materials, two-photon absorption is necessary to populate the first excited state at both wavelengths. This key difference in the electronic excitation process is reflected in the corresponding difference in the LIDT values.
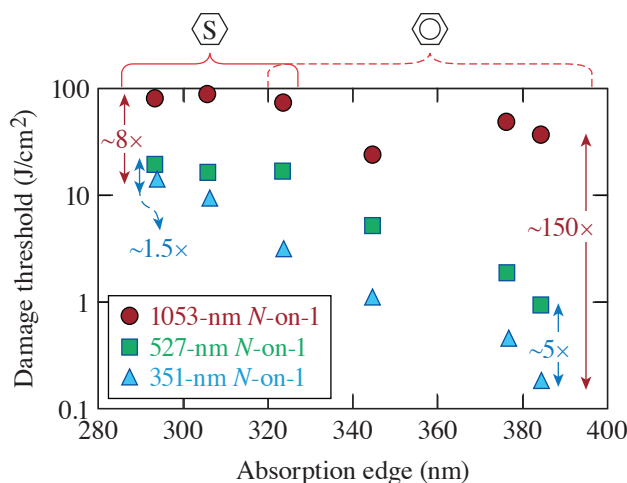

G12393JR

Figure 2

The N-on-1 LIDT values for nanosecond pulses at all three wavelengths (and 1-ns pulses) as a function of each material's absorption edge allows direct comparison of the relative differences in LIDT. The LC's investigated and their apsorption edge, as defined by $T = 98\%$, include: 1550C (294 nm), MLC-2037 (306 nm), ZLI-1646 (324 nm)PPMeOB/PPPOB (345 nm), 5CB (377 nm), and E7 (385 nm). Brackets identify saturated, unsaturated, and mixed materials. The symbols S and ○ are used to designate saturated and unsaturated materials, respectively.

Comparing LIDT results obtained under 351-nm and 1053-nm excitation, the difference in LIDT for unsaturated materials is ~150×, but only ~8× for saturated materials. The dramatic variation in LIDT differences for the two material types is arguably related to the different order of the absorption process required for the $S_0 \longrightarrow S_1$ transition. The order changes from linear absorption to a three-photon absorption process in unsaturated materials, while for saturated materials, a nonlinear process is required at both wavelengths (two-photon and four-photon processes for 351-nm and 1053-nm excitation, respectively). These results demonstrate the importance of the electronic structure of each material on the observed damage threshold and as a function of photon energy.

In summary, the experimental data suggest that key components in the laser-induced damage mechanisms in LC's involve a complex interplay of both multiphoton absorption and excited-state absorption, where their relative contributions vary with wavelength. Future work will concentrate on extending and applying these findings to both glassy and polymer LC materials systems and developing improved passive and active devices that offer polarization, phase, and intensity control for high-peak-power and average-power laser applications.

1. R. Sander, V. Herrmann, and R. Menzel, J. Chem. Phys. **104**, 4390 (1996).

2. G. E. O'Keefe *et al.*, Liq. Cryst. **21**, 225 (1996).

Glancing-Angle–Deposited Silica Films for Ultraviolet Wave Plates

S. MacNally, C. Smith, J. Spaulding, J. Foster, and J. B. Oliver

Laboratory for Laser Energetics, University of Rochester

Glancing-angle deposition (GLAD) is a coating process where the incident vapor condenses on a substrate oriented at a high incidence angle θ relative to the substrate normal, forming microscopic nuclei (experimental setup is shown in Fig. 1). Self-shadowing occurs at this high angle, shaping the nuclei into individual columns that tilt toward the vapor source.[1] These anisotropic structures create birefringence in the film, allowing for the creation of wave plates when depositing a film of the proper thickness.
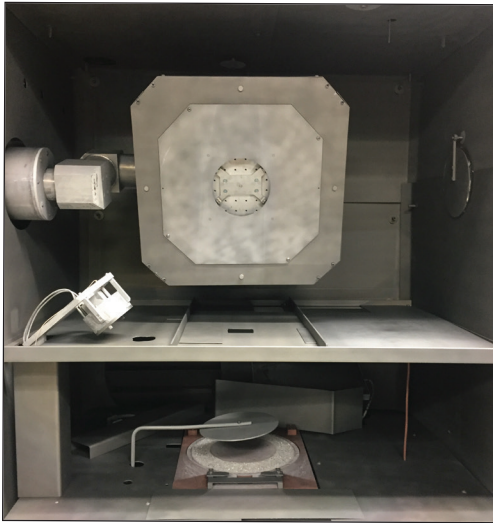
Figure 1
Angstrom Engineering GLAD stage mounted in a 1.2-m vacuum chamber. Each coating deposition included a 100-mm-diam fused-silica substrate or two 50-mm-diam substrates: a silicon wafer and a fused-silica witness sample. Substrates remain in the center of the stage as it flips to the programmed $\pm\theta$. An electron-beam gun is mounted directly below the aperture, and an Inficon Crystal 12 sensor is mounted on the side to measure the deposition rate/thickness.

G12902JR

With a lack of shadowing in the substrate tilt-axis direction, there is a progressive fanning of the column cross section along with a chaining together of adjacent columns, which can lead to greater light scattering in the film. To reduce this column broadening and limit scatter, an all-silica, multilayer GLAD structure was implemented. Alternating layers of birefringent and dense SiO$_2$ were deposited during a single-coating deposition by alternating the substrate angle (0° for the dense layers and 73° for the birefringent layers). The number of birefringent and dense groupings was based on the desired retardance value for a quarter- or half-wave plate at a wavelength of 351 nm. Dense layers provide a base for the growth of a new birefringent layer and were inserted throughout the coating at intervals less than 400 nm since the width of individual silica columns was found to increase only beyond that thickness.[2] An antireflective coating was then added as a final layer in the design, which consisted of a single GLAD layer deposited at 82°.

The refractive indices and thickness of each layer in the design had to be precisely calibrated with a Woollam variable-angle spectroscopic ellipsometer (VASE®) since these values change with substrate deposition angle and deposition time.[3] Scanning electron microscope (SEM) and spectrophotometer measurements were also used to corroborate the index and thickness data.

Photometric performance was evaluated using a 351-nm laser and a 4-in. integrating sphere with a silicon detector. The quarter-wave plate exhibited a reflectance of 3.9% and a transmittance of 95.8%, yielding a loss of 0.3%, while the half-wave plate exhibited a reflectance of 4.2% and a transmittance of 95.3%, yielding a loss of 0.5%. Both reflectance measurements include the uncoated back surface of the substrate. This multilayer design helped to decrease scatter loss compared to previous SiO_2 single-layer coating runs (with an optical scatter loss of 10% to 15%) (Ref. 4). SEM and spectrophotometer measurements for a multilayer quarter-wave plate are shown in Fig. 2.
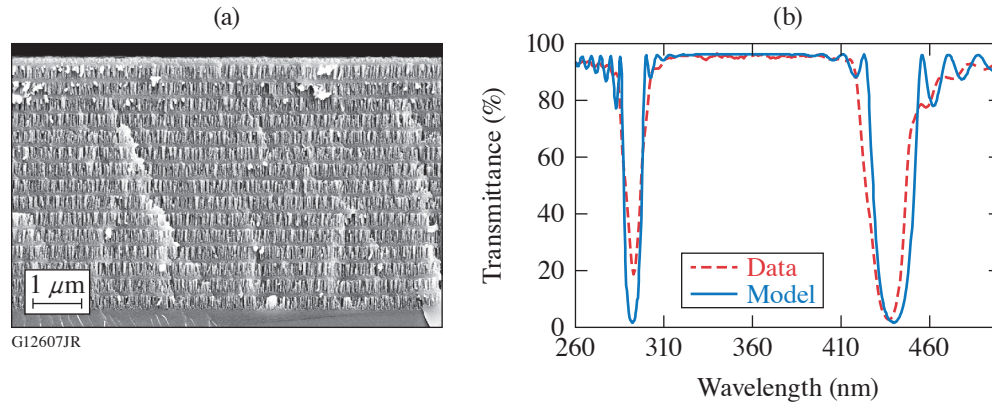
Figure 2
(a) SEM image of a 31-layer quarter-wave–plate coating. (b) Theoretical transmittance through the quarter-wave design with back-side reflection (solid blue curve) overlaid with spectrophotometer data (dashed red curve).

The multilayer design also helped to limit scatter loss over time. Eight months after deposition, the scatter detected in single-layer quarter- and half-wave–plate samples increased 16% and 48%, respectively, while the scatter increase in multilayer wave plates remained under 1% (as shown in Fig. 3).
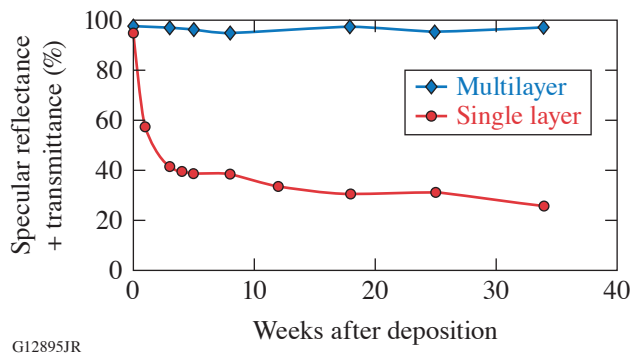
Figure 3
Scatter measurements for a single-layer and multilayer half-wave plate. Eight months after deposition, multilayer scatter has remained approximately the same and single-layer scatter has increased 48%.

Retardance was measured with a Hinds Instruments Exicor® 450XT Mueller Matrix Polarimeter and found to be uniform across all 50-mm and 100-mm samples. The wave plates also exhibited a high laser-induced–damage threshold (LIDT). The LIDT for a multilayer quarter-wave–plate coating, performed on polished fused silica processed with an "advanced mitigation process," was found to be 12.51 ± 0.51 J/cm^2 in a 1:1 testing protocol and 36.31 ± 3.74 J/cm^2 in an N:1 testing protocol. This is an improvement from previous silica single-layer LIDT measurements (~11 J/cm^2 in both a 1:1 and N:1 testing protocol).[4]

In the future, we hope to deposit these multilayer wave plates on larger substrates (up to ~400 mm in diameter), while maintaining the same low-loss, high-LIDT, wide-design bandwidth achieved with this current experiment.

1. M. M. Hawkeye, M. T. Taschuk, and M. J. Brett, *Glancing Angle Deposition of Thin Films: Engineering the Nanoscale*, Wiley Series in Materials for Electronic & Optoelectronic Applications (Wiley, Chichester, United Kingdom, 2014), pp. 6,7, 53–60, 237–240.

2. L. Grinevičiūtė *et al*., Phys. Stat. Sol. A **214**, 1770175 (2017).

3. C. Smith, S. MacNally, and J. B. Oliver, "Modeling of Serially Bi-Deposited Glancing-Angle–Deposition Coatings," to be published in Applied Optics.

4. J. B. Oliver *et al*., Opt. Express **22**, 23,883 (2014).

Stress Compensation by Deposition of a Nonuniform Corrective Coating

J. B. Oliver, B. Charles, and J. Spaulding

Laboratory for Laser Energetics, University of Rochester

Thin-film stresses distort the surface flatness of a coated optic in a convex or concave manner for compressive or tensile films, respectively. While traditional evaporated optical coatings typically lead to the formation of low-magnitude tensile stresses, more-energetic processes such as ion-beam sputtering,[1] magnetron sputtering,[2] and plasma-ion–assisted deposition[3] generally form highly compressive films with significant distortion of the optical surface. Such stress-induced curvature can be mitigated by using thicker substrates, coating the back surface of the optic to yield an equivalent deformation in the opposite direction,[4] or by prefiguring the optic surface to counteract the effects of the film stress.[5] These modifications can be costly, while process modifications to alleviate highly compressive stresses often lead to porous, environmentally unstable films.

A unique approach was developed to prefigure the optic surface by depositing a radially nonuniform film using the same deposition process as the optical coating. The corrective coating is deposited beneath the functional optical coating, on the same surface of the substrate, with a thickness profile designed using finite-element analysis to correct for the anticipated surface-flatness deformation resulting from the eventual optical coating deposition from the as-fabricated flat substrate surface. This approach is depicted in Fig. 1.

G12542JR
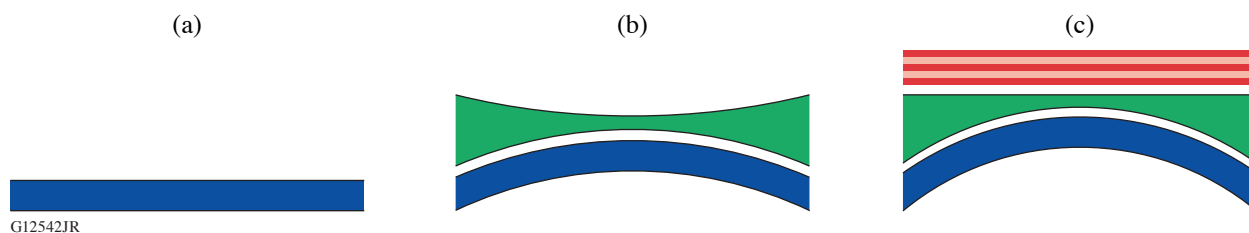
Figure 1

Mitigation of a high compressive film stress by deposition of a gradient compensation layer is illustrated, with (a) the as-fabricated flat substrate; (b) the addition of a compressive, radially graded layer leading to a concave surface, even though the substrate has been deflected in a convex manner; and (c) the combination of the gradient compensation layer and the optical coating leading to a nominally flat coated surface.

This method was used to compensate the stress-induced deformation of a 3.3-μm-thick optical coating on a 100-mm-diam $\times$ 3-mm-thick fused-silica substrate. The coating was deposited using plasma-ion–assisted electron-beam evaporation, with alternating layers of hafnium dioxide and silicon dioxide. The calculated compensation layer consisted of a gradient-thickness silica layer with zero physical thickness at the optic center and increasing in a cubic manner to a thickness of approximately 6.7 μm at the edge. The graded coating was fabricated by depositing the corrective layer directly on the substrate through a mask centered on the rotating optic. The mask blocked all deposition flux from reaching the center of the optic, then gradually increased the open space and corresponding thickness, in a cubic manner, until the full thickness was reached at the optic edge. For the purposes of this proof-of-concept demonstration, the chamber was then vented, the mask removed, and the system evacuated once again in order to deposit the multilayer (non-graded) optical coating. Surface-flatness measurements were taken at each stage of

the deposition process to quantify the changes from the individual process steps. To implement this in a production process, the mask insertion/removal would be automated while the chamber remains under vacuum.

Surface-flatness measurements were performed using a Zygo Verifire 633-nm interferometer of the uncoated substrate, the substrate with the gradient compensation layer, and the finished component after deposition of both the compensation layer and the multilayer mirror. To improve surface-flatness measurement accuracy, the non-graded mirror coating was designed and fabricated with a center wavelength of 633 nm to reduce errors resulting from nonuniformity of the reflected phase of the coating. After process qualification and the development of a suitable compensation profile to yield a flat coated surface, the deformation from any uniform coating deposition could be compensated. The measurement of the uncoated substrate was removed from that of the stress-compensation layer and the overall component to evaluate only the impact of this stress-compensation approach. An additional control substrate was also included in the multilayer deposition to evaluate the anticipated deformation without the use of the compensating layer. The results are shown in Fig. 2.
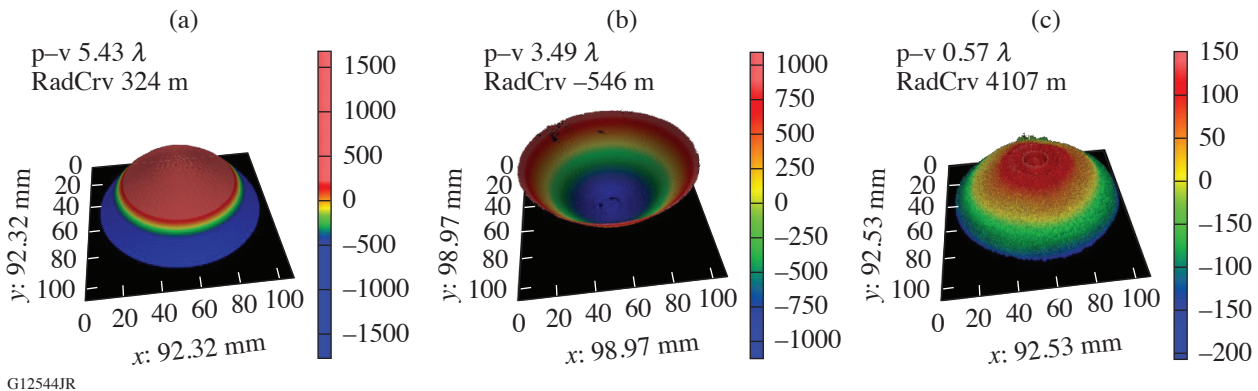
Figure 2
Change in the surface figure of a 100-mm-diam, 3-mm-thick fused-silica substrate as a result of coating with an all-dielectric mirror coating with or without a silica stress-compensation layer (as-fabricated surface flatness subtracted from all subsequent measurements). (a) The control (mirror coating only) surface figure, at 5.4 waves of deviation from flat ($\lambda = 633$ nm). (b) After coating with the silica compensation layer, the surface is 3.5 waves concave. (c) Once the high reflector coating is deposited, the combination of the two coatings results in a nominally flat optic, with the change in surface flatness ~10% of that resulting from the high reflector alone. A slightly thicker compensation layer could further improve the surface flatness. p–v: peak to valley.

The surface deformation of the coated optic with the corrective layer is reduced by nearly 90% relative to that of the coated control substrate without the graded corrective layer [Fig. 2(a) at 5.43 waves versus Fig. 2(c) at 0.57 waves at 633 nm]. It is also clear that a slight increase in the thickness of the corrective layer would further improve the surface flatness, since Fig. 2(c) is still dominated by a spherical-like term with a low edge and a high center (as would result from a compressive film stress, which is the compensation the gradient layer would provide). This stress-mitigation approach significantly reduces the deformation of an optic coated with a compressively stressed film while allowing deposition on a single substrate surface. As demonstrated, a cubic-thickness gradient silica layer can reduce the surface deformation of a compressively stressed optical coating by an order of magnitude.

1. G. W. DeBell, Proc. SPIE **5991**, 599116 (2005).

2. M. Scherer *et al.*, Proc. SPIE **5963**, 596319 (2005).

3. J. B. Oliver *et al.*, Appl. Opt. **50**, C19 (2011).

4. M. Bischoff *et al.*, Appl. Opt. **53**, A212 (2014).

5. S. Gensemer and M. Gross, Opt. Express **23**, 31,171 (2015).

Design and Alignment of an All-Spherical Unobscured, Four-Mirror Image Relay for an Ultra-Broadband Subpetawatt Laser

E. M. Schiesser,[1,2] S.-W. Bahk,[1] J. Bromage,[1,2] and J. P. Rolland[2]

[1]Laboratory for Laser Energetics, University of Rochester
[2]Institute of Optics, University of Rochester

LLE is developing an ultra-broadband optical parametric chirped-pulse–amplified laser system.[1] This laser, the Multi-Terawatt Optical Parametric Amplifier Line (MTW-OPAL),[2] is designed to produce 7.5-J, 15-fs pulses with a 200-nm bandwidth from 810 nm to 1010 nm through multiple stages of noncollinear optical parametric amplifiers (NOPA's). Image relays between NOPA's preserve the beam quality and sequentially magnify the beam size according to its amplified energy level to keep the maximum fluence below the damage threshold. The final relay after the last NOPA stage (referred to as NOPA5 since it is the fifth amplifier) requires an all-reflective, unobscured optical relay to avoid introducing additional longitudinal chromatic aberration, also known as radial group delay (RGD).[3–5] RGD refers to the fact that refractive image relays delay the pulse in the center of the beam with respect to the pulse in the outer edge of the beam as the center beam goes through thicker material in the lens. This RGD is of the order of hundreds of femtoseconds so it is significantly larger than the ideal 15-fs design pulse width and would greatly reduce the focused intensity. The final all-reflective image relay, also referred to as an achromatic image relay (AIR), removes the longitudinal chromatic aberrations and RGD by avoiding lenses in favor of using mirrors. The AIR for NOPA5 performs two roles: it acts as a beam expander to create a 90×90-mm beam from the 45×45-mm output from NOPA5, and it relays the NOPA5 (N5) output to the fourth grating (G4) in the grating compressor chamber (GCC). These two roles must be achieved simultaneously; consequently, two sets of conjugate planes must be simultaneously realized: the "far-field" (FF) collimation planes and the "near-field" (NF) pupil imaging planes. This simultaneous dual-conjugate imaging case has been investigated for two refractive elements and four refractive elements by Wang *et al*.[6]

In optical design, there is often a trade-off between complexity and performance. Off-axis conic sections are the most obvious choice for unobscured, small-FOV (field-of-view) designs like the AIR, as we have previously reported.[7] However, it is important to understand if we can achieve our goals with simpler spherical optics since this reduces complexity and therefore the cost. Instead of field-bias or aperture offset as in an off-axis conic design, one can tilt the optical components to avoid obscuration. Buchroeder[8,9] details many examples of tilted component telescopes, some of which have only spherical components. These designs use tilted components to avoid obscuration, but the relative tilts must be chosen to balance the resulting aberrations. Steven and Dubra[10] describe the design of a two-mirror relay using tilted spherical components.

The design detailed in the present work is a four-mirror all-spherical design that tilts the mirrors to avoid obscuration. We show the theoretical basis for the correction of field-constant coma and field-constant astigmatism using two of the mirror tilts. We then show the alignment of the design in a test-bed setup.

There are nine first-order parameters for this four-mirror system: the input and output working distances, the three distances between the mirrors, and the four radii of curvature of each mirror. The magnification constraint, NF imaging requirement, and FF collimation requirement determine three of these variables. The other six variables are available to meet the layout and space requirements. To meet those requirements, the five distances are specified within a certain range based on the space constraints in the GCC, leaving only one truly free variable: the curvature of the first mirror. This variable is constrained by the stay-out zone created by the damage threshold of the mirrors, which constrains the size of the beam on the mirrors.

With the first-order parameters determined, the next step was to create an unobscured configuration. To do so, we can tilt the components appropriately; however, tilting spherical components results in aberrations. Buchroeder showed that these types of designs, known as tilted-component telescopes, can correct the aberrations caused by the tilts by appropriately tuning the tilts of the mirrors.[8,11] In addition, Rogers showed the same using the nodal aberration theory (NAT) for two and three mirrors for extended fields of view.[12] Because the FOV for the AIR is small at 0.14°, we can achieve the required correction while maintaining enough freedom in the design to keep the AIR within the space constraints of the GCC.

Given the minimum tilt angle of M1 required to remove the obscuration of M2, we can use the theoretical framework of NAT to predict the M3 and M4 tilts necessary to correct the field-constant astigmatism and field-constant coma induced from the tilts of M1 and M2. The system of equations involves two NAT aberration terms composed in terms of the sigma vectors of each surface. The sigma vectors are then related to the tilts of each surface. Because of the quadratic dependence of field-constant astigmatism on the sigma vector, there are two solutions; however, only one solution is unobscured, shown in Fig. 1. The angles from the theoretical analysis were ultimately optimized to balance the aberrations and reduce the overall rms wavefront error.

G12859JR

Figure 1
The final layout of the AIR mirrors, showing the ray path from the central field point.

An alignment plan for the AIR has been developed and tested. The alignment procedure consists of two stages: course alignment and fine alignment. The course alignment stage uses the arm of a precision coordinate-measuring machine (CMM) to place precision-machined pinhole jigs. The CMM arm is a FARO Gage Plus, from which we achieved of the order of 100-μm placement accuracy of the pinholes.[13] Passing a pencil beam from an alignment laser diode through the pinholes establishes a line that serves as the optical axis. Since the mirrors are spherical, guiding the pencil beam through the pinholes using tip/tilt and z travel on each mirror can be used to position the center of curvature close to the nominally designed position. All four mirrors can be coarsely aligned sequentially with this method. Tolerance analysis assuming 100-μm accuracy in the mirror placement of the AIR design shows that the coarse alignment using the pinholes is adequate to position the mirrors accurately enough such that fine alignment of M4 tip, tilt, and defocus can correct any residual defocus and astigmatism still present after course alignment. Additionally, M3 tip/tilt can be used to correct residual coma, if necessary.

To test the feasibility of the alignment plan and to troubleshoot possible difficulties before the final alignment in the GCC, we developed a test bed to replicate the *in-situ* alignment before the final system is aligned at LLE. The essential components of the test bed are a 532-nm laser diode, a custom wavefront sensor,[14] a polarizing beam splitter, a beam expander, and several planar mirrors.

The NOPA5 crystal outputs a 45×45-mm collimated beam. To replicate this in the test bed, we use two beam expanders as shown in Fig. 2: The first is a $4\times$ beam expander that focuses the output of a laser diode into a 25-μm pinhole used as a spatial filter. The resulting Gaussian beam is then collimated and truncated using a square apodizer before passing through a polarizing beam splitter (PBS). The second beam expander then enlarges the beam to 45×45 mm. A quarter-wave plate at the focus of the $10\times$ beam expander rotates the polarization of the return beam from vertical to horizontal to reduce spurious reflections from PBS. Additionally, an adjustable iris is used to create a pencil beam for the course alignment step. The return beam reflects off the PBS interface to a wavefront sensor and a blank mirror substrate with a wedge acting as a second beam splitter. The second return beam is directed into a focusing lens and charge-coupled–device camera used to maintain alignment.

The subsequent wavefront after the course alignment routine using the pinholes is shown in Fig. 3(a). The dominant aberration in the wavefront after the course alignment step appears to be defocused. Figure 4 shows the peak-to-valley (p–v) and rms

G12861JR
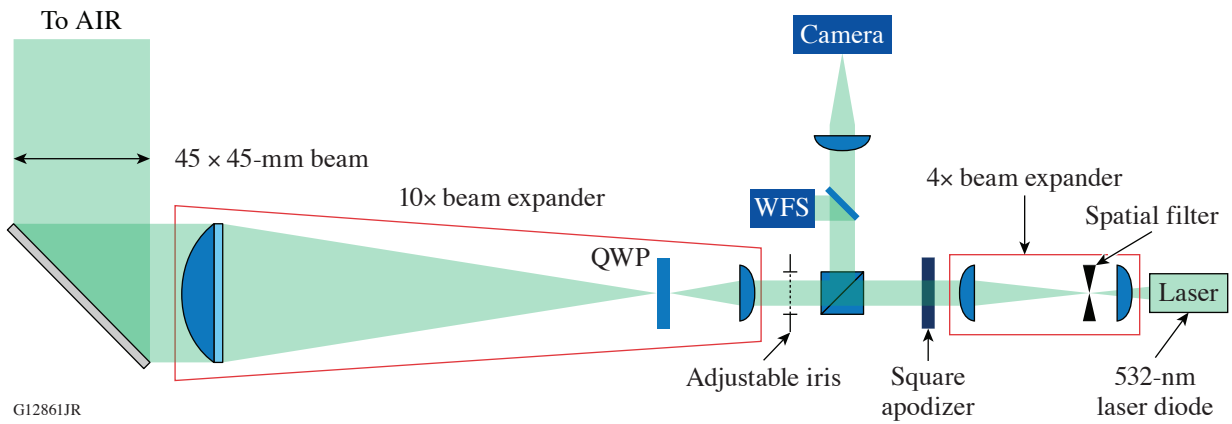
Figure 2
The test-bed components to produce a 45 × 45-mm beam and to measure the return wavefront. QWP: quarter-wave plate; WFS: wavefront sensor.

G12864JR
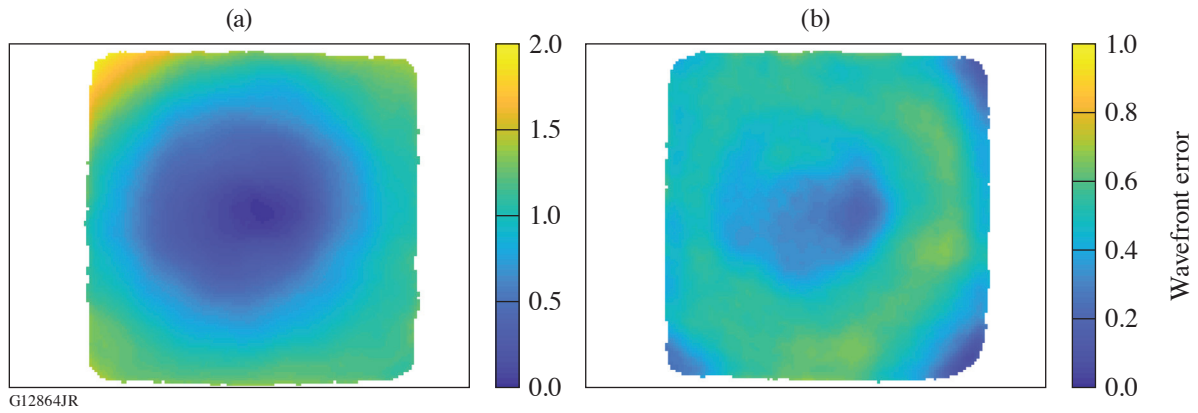
Figure 3
The double-pass wavefront given in waves at 532 nm for (a) after the course alignment step and (b) after the fine alignment steps. Note that the color scale ranges from [0,2] waves for (a) and from [0,1] waves for (b).

G12866JR
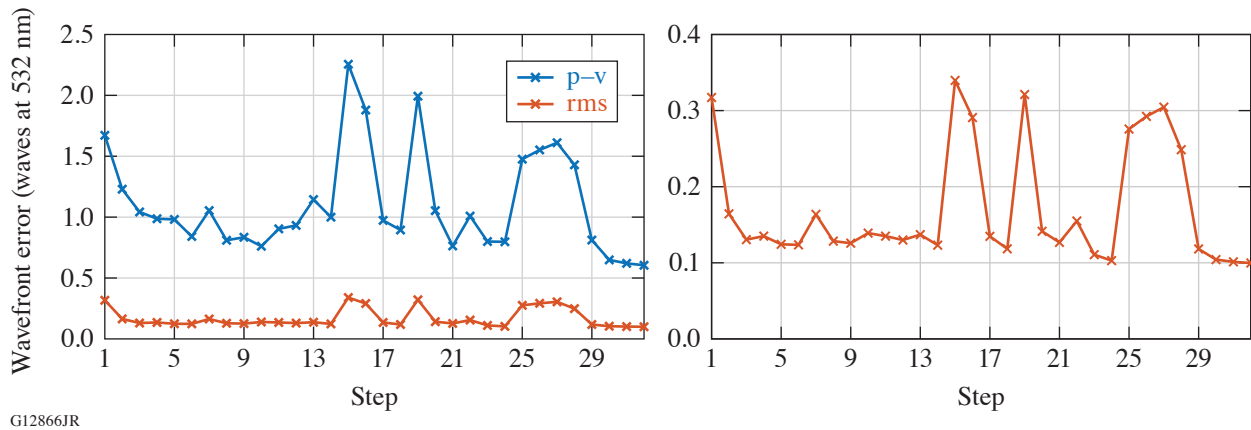
Figure 4
(a) The p–v and rms values of the wavefront at each step; (b) the rms WFE values of the wavefront at each step.

wavefront error (WFE) of the wavefront at each step in the fine alignment process. This defocus was more than predicted by the tolerances of the CMM coarse alignment stage—a clue to another issue that will be addressed later.

Figure 3(b) shows the measured wavefront error after fine alignment. There is residual spherical aberration, as predicted by the ray-tracing model. Additionally, there is still some coma (Z7/8) present and higher-order modes are also becoming dominant. Since we reached the desired p–v and rms WFE targets, however, we stopped the alignment process. With the aid of the program used to decompose the wavefront and predict the adjustments, the fine alignment routine can be completed in less than 1 h. After completing fine alignment, the resulting wavefront p–v at 532 nm was 0.61 waves and the rms WFE was 0.10 waves in double pass. Applying the reduction factor of 3.42 to the measured wavefronts in Fig. 3, we have 0.176 waves p–v and 0.029 waves rms. Therefore, we can expect a wavefront p–v of less than 0.2 waves and rms WFE of less than 0.05 waves at 910 nm at the output of the AIR using this method.

After the wavefront was aligned, the magnification of the beam was measured. Minimizing magnification error is important for laser systems with large beams. For the AIR, the magnification was required to be –2.00±2%. To measure the magnification in the test bed, a mask with holes was placed at the object plane and the distance between the images of the holes was measured in the image. The relative distance between the holes was measured.

The result was a magnification of –2.13±2%, which is a +7.5% change from the required value of –2.00±2%. At first, this error was suspected to be caused by uncertainties in the alignment process. However, the course and fine alignment processes were repeated multiple times to test this suspicion, and the magnification was remeasured each time. The measured value of the magnification varied by less than 1% between alignments. To bring the magnification back into spec, the position of another mirror besides M4 must be adjusted; however, the same space constraints in the design process also restrict us here: M2 is already very close to the GCC wall. Although there is some room to move M1, moving it would require changing the input angle of the beam from N5, which is not ideal. M3, being the only mirror left, is the best candidate to move. To test how far was required, the location of M3 was moved by 75 mm toward M2 to shorten the focal length of the M3/M4 pair in the model with the measured radii, which reduced the magnification by 3.5%. This adjustment reduced the output working distance to the image plane (G4) by 75 mm. This change was reproduced in the test bed, and the magnification was remeasured to be 2.07, bringing the magnification error down from 7.5% to 3.5%. Based on the model, to bring the magnification error down another 3.5%, we could move the M3 mirror by another 75 mm. Since the test-bed optics likely do not have exactly the same radii as the *in-situ* AIR optics, this final M3 mirror adjustment was not performed on the test bed. The actual compensation will be based on the measurements of the *in-situ* AIR mirrors.

The design of an unobscured reflective laser relay comprising four tilted spherical mirrors has been described. We showed the theoretical basis for such a four-mirror design using first-order optical matrix methods and NAT. We then described the process of aligning the design in a test bed to demonstrate an effective alignment method for such a design. We were able to achieve a nominal design that met our specifications and also successfully align the design in a test-bed environment to achieve our target wavefront error of less than 0.25 waves p–v and 0.07 waves rms.

1. S.-W. Bahk, J. Bromage, and J. D. Zuegel, Opt. Lett. **39**, 1081 (2014).

2. J. Bromage *et al*., High Power Laser Sci. Eng. **7**, e4 (2019).

3. Z. Bor, Opt. Lett. **14**, 119 (1989).

4. Zs. Bor and Z. L. Horváth, Opt. Commun. **94**, 249 (1992).

5. H.-M. Heuck *et al*., Appl. Phys. B **84**, 421 (2006).

6. D. Y. Wang, D. M. Aikens, and R. E. English, Jr., Opt. Eng. **39**, 1788 (2000).

7. E. M. Schiesser *et al*., Opt. Lett. **43**, 4855 (2018).

8. R. A. Buchroeder, Appl. Opt. **9**, 2169 (1970).

9. R. A. Buchroeder, Optical Sciences Center, University of Arizona, Tucson, AZ, Optical Sciences Technical Report 68 (1971).

10. S. Steven, J. Bentley, and A. Dubra, Opt. Express **27**, 11205 (2019).

11. R. A. Buchroeder, "Titled Component Optical Systems," Ph.D. thesis, University of Arizona, 1976.

12. J. R. Rogers, Opt. Eng. **39**, 1776 (2000).

13. FARO Gage & Gage-PLUS, 20 February 2009, http://www.dirdim.com/pdfs/DDI_FARO_Gage.pdf.

14. S.-W. Bahk and C. Dorrer, in *Imaging and Applied Optics*, OSA Technical Digest (online) (Optical Society of America, Washington, DC, 2013), Paper CM3C.4.

Ellipsometric Modeling of Serially Bi-Deposited Glancing-Angle–Deposition Coatings

C. Smith, S. MacNally, and J. Oliver

Laboratory for Laser Energetics, University of Rochester

Glancing-angle–deposition (GLAD) coatings have been in development at LLE for a variety of applications. When produced using serial bi-deposition,[1] a birefringence is created due to the difference in coating density along perpendicular axes in the coating plane, as shown in Fig. 1. The higher-density direction corresponds to the coating flip axis, while the lower-density region is created due to the self-shadowing nature of the GLAD coating process.
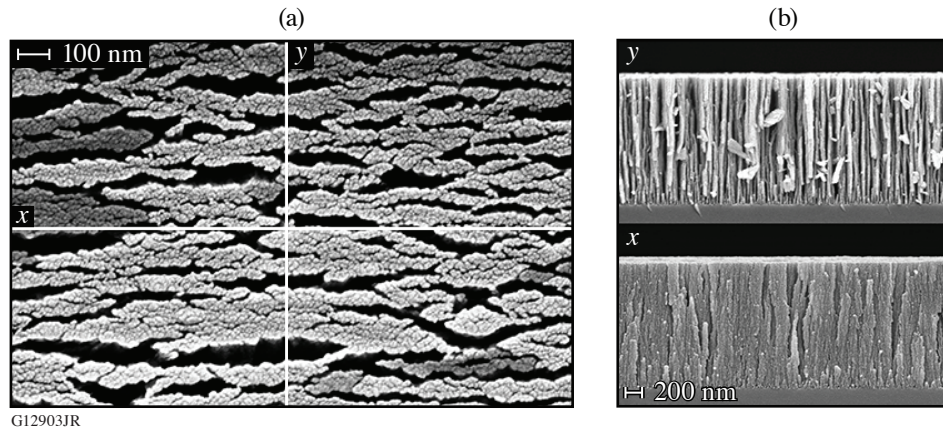
Figure 1

The birefringence of these coatings is achieved because of the microstructure produced in the GLAD serial bi-depostion process. The scanning electron micrograph of (a) the top view of the coating shows the directionality of the density difference, while (b) the side view shows the magnitude.

The birefringence created in this process makes ellipsometric modeling difficult due to the number of fit parameters, leaving unconstrained variables. Incorrect models produce unreliable dispersion curves, making coating design nearly impossible. In this work, a process was developed combining ellipsometric measurement techniques with well-established optical coating design methods to create precise index models. This enabled the development of complex optical coatings using only a single material.

In this experiment, a coating was designed using alternating GLAD and amorphous silica layers. To create these multilayer coatings, a methodical approach was taken. Short, single-layer GLAD coatings were created and measured on a Woollam VASE® ellipsometer in multiple orientations. This made precise characterization possible, resulting in high-quality dispersion curves. Due to the deposition process used in this experiment, the multilayer coating was presumed to have a slightly different density than the single-layer coatings. To correct for this, the single-layer dispersion curves were used to design a seven-layer calibration coating described by Baumeister.[2] This coating is highly sensitive to changes in optical thickness and is commonly used for material characterization or process corrections. When this coating was evaluated (Fig. 2) and optimized using the thin-film design software OptiRE, new dispersion curves were created that closely matched the measured performance.

(a) Spectral design versus measured data used to create the seven-layer coating; (b) SEM micrograph of the calibration coating.
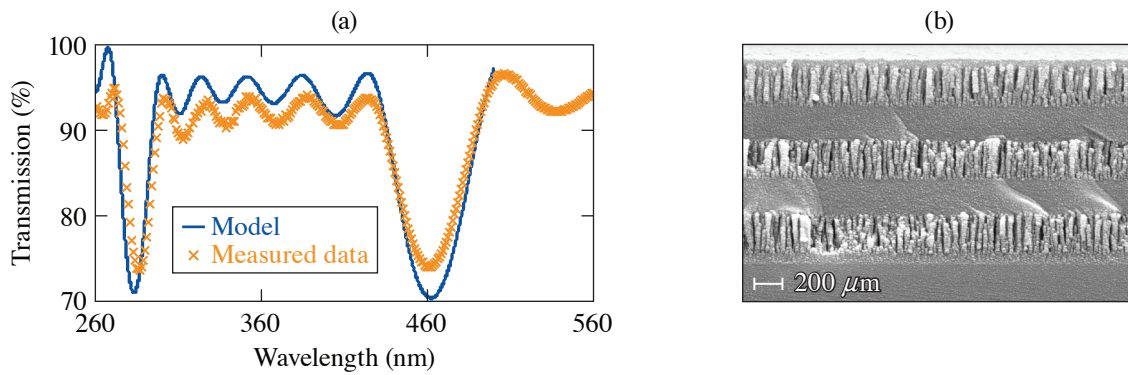
G12708aJR

Figure 2
(a) Spectral design versus measured data used to create the seven-layer coating; (b) SEM micrograph of the calibration coating.

Additionally, this experiment required an antireflective (AR) overcoat. A three-layer coating was designed to mimic the density of the final three layers of the multilayer. This coating was evaluated using the same techniques described above, and a dispersion curve for the final layer was found. Using these data, along with the data from the seven-layer coating, a 31-layer wave plate was created (Fig. 3).

This experiment used only three different coating parameters to alter the index of the material and create a final product with only three indices, but the technique described is sufficient for the design and production of a limitless number of indices using a single material. Future work will focus on expanding these capabilities.
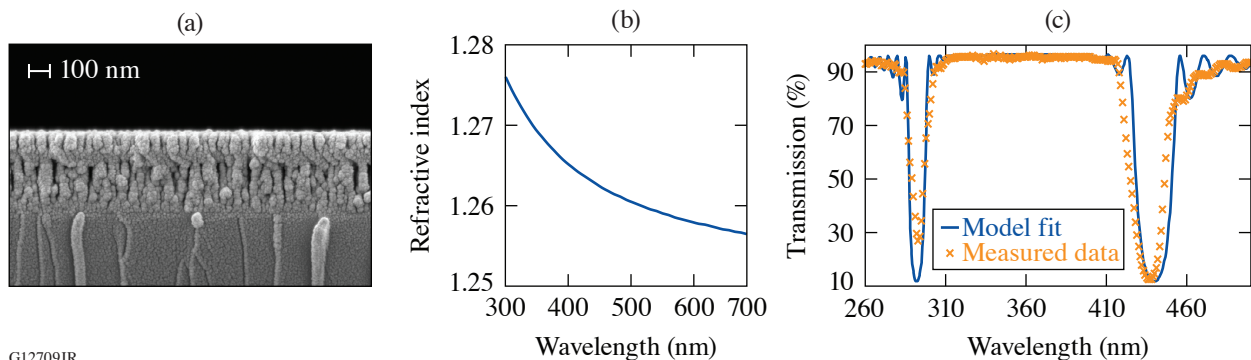
G12709JR

Figure 3
(a) A three-layer coating closely approximating the last three layers of the wave plate; (b) dispersion curve calculated for the final AR layer; (c) spectral measurement versus measured data used to create the 31-layer coating.

1. S. MacNally *et al.*, in *Optical Interference Coatings Conference (OIC) 2019*, OSA Technical Digest (OIC) 2019 (Optical Society of America, 2019), Paper MD.2.

2. P. Baumeister, *Optical Coating Technology* (SPIE Optical Engineering Press, 2004), pp. 9-56–9-57.

Modeling Variable-Impedance, Magnetically Insulated Transmission Lines

R. B. Spielman and A. B. Sefkow

Laboratory for Laser Energetics, University of Rochester

The design of very-low-inductance, magnetically insulated transmission lines (MITL's) is a critical part of building low-inductance vacuum transmission lines and load configurations. It becomes more difficult to build low-impedance (low-inductance), constant-impedance MITL's when the MITL's must operate at high voltage. This is due to the increase in the fraction of the electrical current carried in vacuum electron flow in the MITL's at high voltage. Vacuum electron flow can be lost at downstream locations with impedance mismatches and at vacuum convolutes. We describe the design of a variable-impedance, disk MITL that allows us to reduce the inductance of disk MITL's. In this design, the impedance of the MITL at a radius of $r = 150$ cm is at 1.5 Ω, while the impedance of the MITL at a radius of $r = 30$ cm is 2 Ω. The impedance transition between these two radial locations can be done many ways but this summary uses a simple linear change in gap from the outer 1.5-Ω MITL to the inner 2.0-Ω MITL. Two-dimensional, electromagnetic (EM) particle-in-cell (PIC) simulations of this variable-impedance MITL will show electron flow and losses.

Our variable-impedance MITL is a conical disk MITL that starts at a radius of $r = 150$ cm and proceeds inward to a radius of $r = 30$ cm (see Fig. 1). The initial geometric impedance is 1.5 Ω (at 150 cm) with a gap of dz = 3.76 cm. The final geometric impedance is 2 Ω (at 30 cm) with a gap of dz = 1 cm. The inductance of this variable-impedance, disk MITL is 6.52 nH, a reduction of 1.55 nH when compared with an 8.07-nH, 2-Ω disk MITL. We now clearly see the reason for a variable-impedance MITL—lower inductance leading to higher efficiencies. The 2-Ω MITL design was described by Spielman and Reisman,[1] where a Z-flow model was used to quantify the vacuum electron flow at peak MITL voltage. The circuit code *Screamer*[2] was used to model
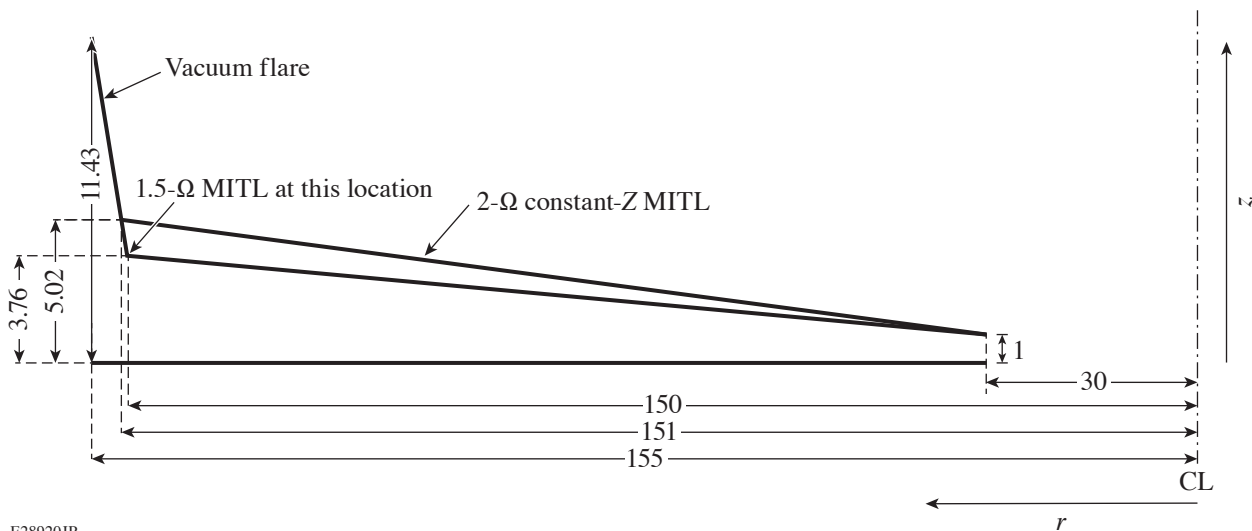

Figure 1

We show a schematic of a conical-disk MITL having a constant, 2-Ω impedance MITL profile and a similar conical-disk MITL having a variable, 1.5-Ω to 2-Ω impedance MITL profile. The figure shows a slice of the MITL at a single rotational angle around the marked center line. All units are in cm. CL: center line.

the qualitative MITL performance in Ref. 1. Herein, we model electron losses that will occur in a well-behaved, superinsulated variable-impedance disk MITL operating with equilibrium, vacuum electron flow. While we know that *any* variable-impedance MITL will have losses,[3] we assert that the real question is the magnitude of such losses.

The analytic approach to modeling electron losses in a variable-impedance MITL is based on the Z_{flow} model for MITL's described by Ottinger *et al.*[4] We assume as a worst case that any change in vacuum electron flow in excess of the retrapping current seen in the constant, the 2-Ω impedance case is lost at each segment transition. A 2-Ω MITL, as modeled here, has a slowly dropping vacuum electron flow moving inward due the nonmatched load. This forces retrapping of some of the vacuum electron flow. In reality, these loss currents are not at the discrete segment boundaries but are distributed over the entire MITL. The peak vacuum flow in the variable-impedance case is ~4% of the total anode current (in the outer MITL segment). The loss currents range from 3.4 kA on the outer segment to 6.2 kA on the inner segment. Importantly, the increase in total current due to the reduced inductance exceeds the increase in vacuum flow by 3×.

This particular impedance profile (linear in gap, not linear in Z) is not the optimum profile for pushing electron losses radially outward, where they have less impact due to the larger surface area. Various impedance profiles are possible and some of these have lower inductance than others. It is important to note that these predicted variable-impedance loss currents are significantly lower than the current losses seen during the setup of magnetic insulation.[1] It should be obvious that a variable-impedance MITL with a larger change in impedance (e.g., 1 Ω to 2 Ω) would suffer larger electron losses. Eventually, the losses in a variable-impedance MITL due to large impedance changes would approach the current losses seen during the setup of magnetic insulation and possibly result in MITL failure due to anode heating.

A 2-D EM PIC code can provide a more-quantitative picture of the electron losses in a variable-impedance MITL. For numerical accuracy, the number of macroparticles must be kept large (poor run time). The *LSP* code[5] is used to model the electron flow in the MITL's.

In *LSP*, the voltage waveforms generated in *Screamer* calculations are used as input to the simulation. The physical geometry of the MITL is as described earlier in Fig. 1. *LSP* invokes a unipolar, Child–Langmuir emission model that starts electron emission from the cathode at 200 kV/cm. An adaptive particle management routine is used to maintain about 100 particles per cell, resulting in a few million total macroparticles in the calculation. Radial resolution is ~1000 μm and axial resolution is ~100 μm.

We first ran a simulation with a constant-impedance 2-Ω MITL. In this case we do not expect losses in the constant-impedance section of the MITL. Figure 2 shows a snapshot of the electron density in the simulation at 100 ns, the time where the voltage is maximum and the current has reached half its peak. The Z-flow MITL theory predicts this MITL is perfectly insulated at peak voltage with no electron losses. The dz thickness of the vacuum sheath will decrease slightly as one moves from larger to smaller radius. The simulation is then rerun with identical electrical parameters except for the geometric boundary change of the variable-impedance disk MITL. The MITL impedance varies from 1.5 Ω at R = 150 cm and 2 Ω at R = 30 cm. For comparison, Fig. 3 shows the analogous snapshot of the variable-impedance MITL simulation at 100 ns.

One can now compare the two simulations. First, the small vortices that form in Fig. 2 appear to be influenced by the stairstep profile found on the MITL anode. Use of a surface-conformal meshing technique in these simulations would allow full clarification of this point. An examination of the electron flow in Fig. 3 shows similar vortices that are larger in amplitude and shorter in wavelength than those in Fig. 2. One can see that the thickness of the electron sheath at large radius is thicker in Fig. 3 than in Fig. 2. This is expected since the lower-impedance MITL modeled in Fig. 3 should have the larger sheath. Examination of multiple time steps of both simulations shows that these vortices have rotational flow (counterclockwise). It is interesting to note that the thickness of the electron sheath between the vortices is as expected in Fig. 3. The higher impedance at smaller radius results in the same electron sheath thickness as the constant 2-Ω case.

Importantly, there are no increased electron losses to the anode at the time of peak voltage in the variable-impedance case. This is true even though we have used a poor impedance profile with radius, where the use of a geometric straight line has greater dZ/dr at smaller radius and so should develop more losses at smaller radii. More-favorable dZ/dr profiles would reduce or eliminate the dZ/dr at small radius and push the changes in Z to larger radii, where losses are significantly less consequential.
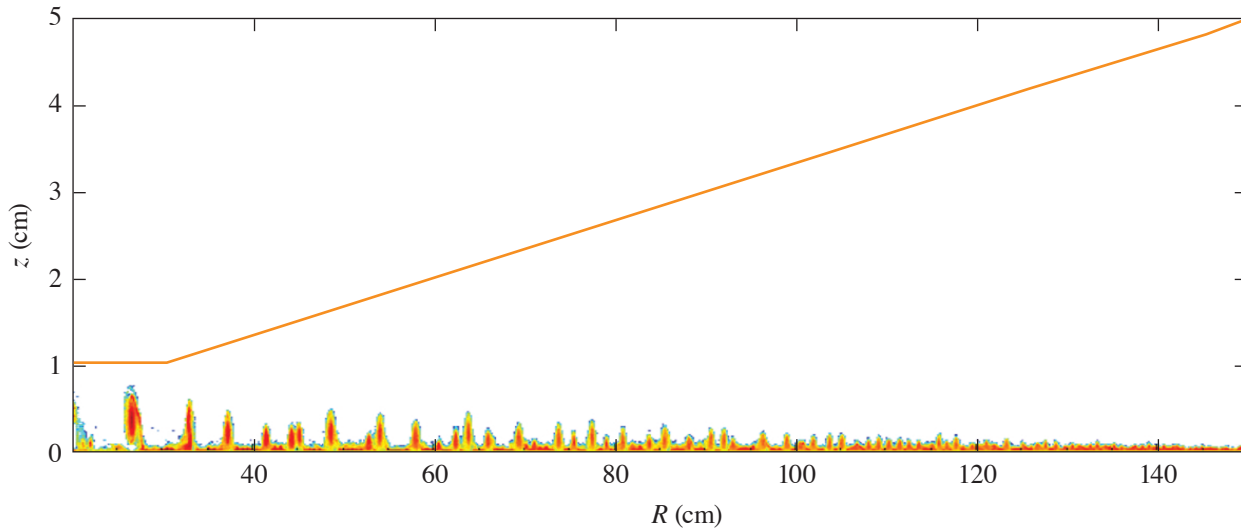
E28921JR

Figure 2
A snapshot of constant-impedance (2-Ω) MITL performance at $t = 100$ ns, where the simulation is at peak voltage and 0.5× maximum current.
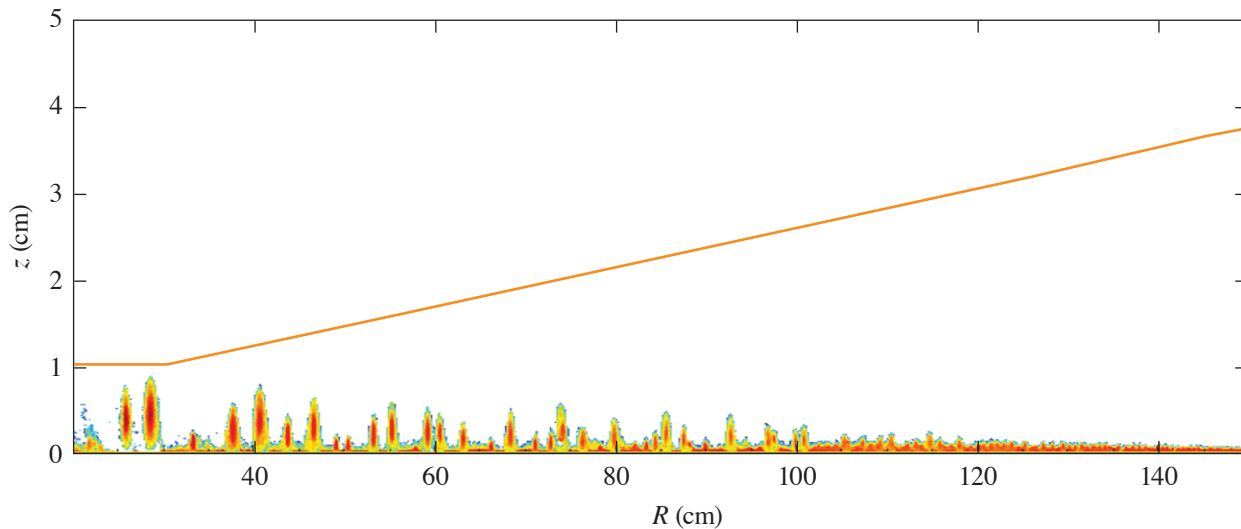
E28922JR

Figure 3
A snapshot of variable-impedance (1.5-Ω to 2-Ω) MITL performance at $t = 100$ ns, where the simulation is at peak voltage and 0.5× maximum current.

1. R. B. Spielman and D. B. Reisman, Matter Radiat. Extremes **4**, 027402 (2019); **4**, 049901(E) (2019).

2. R. B. Spielman and Y. Gryazin, in *2015 IEEE Pulsed Power Conference (PPC)* (IEEE, Piscataway, NJ, 2015).

3. T. D. Pointon and M. E. Savage, in *2005 IEEE Pulsed Power Conference* (IEEE, Piscataway, NJ, 2005), pp. 151–154.

4. P. F. Ottinger *et al.*, in *17th IEEE International Pulsed Power Conference*, edited by R. D. Curry (IEEE, Piscataway, NJ, 2009), pp. 1176–1179.

5. D. V. Rose *et al.*, Phys. Rev. Spec. Top., Accel. Beams **18**, 030402 (2015).

LLE's Summer High School Research Program

R. S. Craxton

Laboratory for Laser Energetics, University of Rochester

During the summer of 2019, 14 students from Rochester-area high schools participated in the Laboratory for Laser Energetics' Summer High School Research Program. This was the 31st year of the program, which started in 1989. The goal of the program is to excite a group of high school students about careers in the areas of science and technology by exposing them to research in a state-of-the-art environment. Too often, students are exposed to "research" only through classroom laboratories, which have prescribed procedures and predictable results. In LLE's summer program, the students experience many of the trials, tribulations, and rewards of scientific research. By participating in research in a real environment, the students often become more excited about careers in science and technology. In addition, LLE gains from the contributions of the many highly talented students who are attracted to the program.

The students spent most of their time working on their individual research projects with members of LLE's technical staff. The projects were related to current research activities at LLE and covered a broad range of areas of interest including experimental diagnostic development, computer modeling of implosion physics, cryogenic target characterization, experimental design, irradiation uniformity, physical chemistry, and optical materials characterization (see Table I).

The students attended weekly seminars on technical topics associated with LLE's research. Topics this year included laser physics, fusion, fission, pulsed power, holography, and LLE's cryogenic target program. The students also received safety training, learned how to give scientific presentations, and were introduced to LLE's resources, especially the computational facilities.

The program culminated on 28 August with the "High School Student Summer Research Symposium," at which the students presented the results of their research to an audience including parents, teachers, and LLE staff. The students' written reports will be made available on the LLE Website and bound into a permanent record of their work that can be cited in scientific publications.

Three hundred and ninety-one high school students have now participated in the program. This year's students were selected from just over 40 applicants.

At the symposium LLE presented its 23rd annual William D. Ryan Inspirational Teacher Award to Mrs. Rebecca Berardino, a mathematics teacher at Barker Road Middle School in Pittsford. This award is presented to a teacher who motivated one of the participants in LLE's Summer High School Research Program to study science, mathematics, or technology and includes a $1000 cash prize. Teachers are nominated by alumni of the summer program. Mrs. Berardino was nominated by Margaret Rudnick, a participant in the 2018 program. Margaret wrote, "Mrs. Berardino is the single most instrumental person that caused me to fall in love with the intricacies of complex problems, ultimately leading me to pursue a STEM-related field in college and probably as a career." When Margaret encountered Mrs. Berardino in seventh grade, she was shocked to find that Mrs. Berardino refused to give her the answers she wanted but told her to work out the problem for herself: "I still vividly remember the panic I felt when Mrs. Berardino said, 'I'm not going to feed you the answer with a silver spoon.'" Margaret had no choice but to persevere. After "an inordinate amount of approaches and thought processes," she came to the answer on her own: "I had never experienced that moment of sincere joy and triumph after mentally crawling to the top of a mountain…This moment changed my life." After

Mrs. Berardino's classes, Margaret was inspired to sign up for the most rigorous science and math classes available and "constantly seek the excitement of advanced learning…I realized that I absolutely do not want to be fed with a silver spoon." Other students in Mrs. Berardino's class were also inspired: "She opened our eyes to the wonder of not just mathematics, but the world, making sure to enrich our theoretical learning with cool examples of math in nature." Margaret concluded by saying, "So much of my love for science is owed to Mrs. Berardino, and looking back, her amazing classes are the part of middle school I remember the best."

Table I: High School Students and Projects—Summer 2019.

Name	High School	Supervisor	Project Title
Henry Berger	Brighton	C. J. Forrest	Design of a Single-Hit Neutron Spectrometer for Long-Duration Fusion Reactions
Adelyn Carney	Webster Schroeder	H. G. Rinderknecht	Optimization of X-Ray Prepulse Geometry for Imprint Mitigation in Directly Driven Implosions
Ji-Mi Jang	Pittsford Mendon	T. Z. Kosc	Micro Raman Spectroscopy of Silica and Hafnia Laser Damage Sites
Christopher "Jude" Kukla	Pittsford Mendon	F. J. Marshall and S. T. Ivancic	Evaluation of Fresnel Zone Plate X-Ray Imagers for Inertial Confinement Fusion Applications
Michele Lin	Attica	M. McCluskey	A Comparative Study of the Effects of Methanol and Ethanol Solutions on the Bulk Etch Rate of CR-39
Anthony Mazzacane	Pittsford Mendon	P. B. Radha, O. M. Mannion, and S. Miller	Using *IRIS3D* to Simulate the Effects of Smoothing by Spectral Dispersion on Cryogenic Implosions
George Morcos	Rush Henrietta	K. L. Marshall	Glassy Liquid Crystals Based on Natural Products for High-Peak-Power Laser Optics
Adam Mroueh	Pittsford Sutherland	D. Broege	Schlieren Diagnostic for the Imaging of Thermal Turbulence
Ka-Hyun Nam	Brighton	C. Fagan and W. T. Shmayda	Comparative Analysis of Oxygen Uptake in Nickel and Copper-Zinc Beds
Simon Narang	Pittsford Sutherland	M. D. Wittman and D. Bredesen	Application for Filling Cryogenic Targets at an Arbitrary Viewing Angle
Max Neiderbach	Geneseo	M. Sharpe, V. Anand, and R. Peck	Enhancements to the Calorimetric Measurement System on the OMEGA Laser
Stephen Rosa	Eastridge	W. T. Shmayda and M. D. Sharpe	Investigations of the Hydrogen-Palladium and Deuterium-Palladium Systems
William Wang	Pittsford Sutherland	R. S. Craxton	Development of a Beam Configuration for the SG4 Laser to Support both Direct and Indirect Drive
Hanna Wiandt	Pittsford Mendon	R. S. Craxton	Optimization of the Uniformity of 12-Quad Targets for the National Ignition Facility

FY19 Q4 Laser Facility Report

J. Puth, M. Labuzeta, and D. Canning

Laboratory for Laser Energetics

During the fourth quarter of FY19, the Omega Facility conducted 421 target shots on OMEGA and 201 target shots on OMEGA EP for a total of 622 target shots (see Tables I and II). OMEGA averaged 11.1 target shots per operating day, averaging 95.7% Availability and 95.4% Experimental Effectiveness.

OMEGA EP was operated extensively in Q4 FY19 for a variety of user experiments. OMEGA EP averaged 8.0 target shots per operating day, averaging 96.4% Availability and 93.8% Experimental Effectiveness.

Table I: OMEGA Laser System target shot summary for Q4 FY19.

Program	Laboratory	Planned Number of Target Shots	Actual Number of Target Shots
ICF	LLE	143	155
	LANL	22	24
	LLNL	16.5	15
	NRL	11	7
ICF Subtotal		192.5	201
HED	LLE	22	21
	LANL	44	46
	LLNL	33	35
HED Subtotal		99	102
CEA	CEA	11	14
LBS	LLE	33	38
	LLNL	27.5	35
	Oxford	11	8
LLE Calibration	LLE	0	23
Grand Total		374	421

Table II: OMEGA EP Laser System target shot summary for Q4 FY19.

Program	Laboratory	Planned Number of Target Shots	Actual Number of Target Shots
ICF	LLE	24.5	32
	LANL	14	22
ICF Subtotal		38.5	54
HED	LLE	28	32
	LANL	7	8
	LLNL	42	42
HED Subtotal		77	82
CEA	CEA	7	11
LBS	LANL	7	5
	LLE	14	17
	LLNL	7	14
	Oxford	3.5	7
LLE Calibration	LLE	7	11
Grand Total		161	201

Publications and Conference Presentations

— Publications —

A. Antikainen and G. P. Agrawal, "Soliton Supermode Transitions and Total Red Shift Suppression in Multi-Core Fibers," Opt. Lett. **44**, 4159 (2019).

S. Bucht, D. Haberberger, J. Bromage, and D. H. Froula, "Methodology for Designing Grism Stretchers for Idler-Based Optical Parametric Chirped-Pulse-Amplification Systems," J. Opt. Soc. Am. B **36**, 2325 (2019).

D. Cao, R. C. Shah, S. P. Regan, R. Epstein, I. V. Igumenshchev, V. Gopalaswamy, A. R. Christopherson, W. Theobald, P. B. Radha, and V. N. Goncharov, "Interpreting the Electron Temperature Inferred from X-Ray Continuum Emission for Direct-Drive Inertial Confinement Fusion Implosions on OMEGA," Phys. Plasmas **26**, 082709 (2019).

M. Chorel, S. Papernov, A. A. Kozlov, B. N. Hoffman, J. B. Oliver, S. G. Demos, T. Lanternier, É. Lavastre, L. Lamaignère, N. Roquin, B. Bousquet, N. Bonod, and J. Néauport, "Influence of Absorption-Edge Properties on Subpicosecond Intrinsic Laser-Damage Threshold at 1053 nm in Hafnia and Silica Monolayers," Opt. Express **27**, 16,922 (2019).

A. Colaïtis, R. K. Follett, J. P. Palastro, I. Igumenshchev, and V. Goncharov, "Adaptive Inverse Ray-Tracing for Accurate and Efficient Modeling of Cross Beam Energy Transfer in Hydrodynamics Simulations," Phys. Plasmas **26**, 072706 (2019).

C. N. Danson, C. Haefner, J. Bromage, T. Butcher, J.-C. F. Chanteloup, E. A. Chowdhury, A. Galvanauskas, L. A. Gizzi, J. Hein, D. I. Hillier, N. W. Hopps, Y. Kato, E. A. Khazanov, R. Kodama, G. Korn, R. Li, Y. Li, J. Limpert, J. Ma, C. H. Nam, D. Neely, D. Papadopoulos, R. R. Penman, L. Qian, J. J. Rocca, A. A. Shaykin, C. W. Siders, C. Spindloe, S. Szatmári, R. M. G. M. Trines, J. Zhu, P. Zhu, and J. D. Zuegel, "Petawatt and Exawatt Class Lasers Worldwide," High Power Laser Sci. Eng. **7**, e54 (2019).

J. DeGroote Nelson, T. Z. Kosc, and P. C. Nelson, "The Optics Suitcase: Educational Outreach Tool for Inspiring Careers in Light," Proc. SPIE **11143**, 111432N (2019).

S. G. Demos, J. C. Lambropoulos, R. A. Negres, M. J. Matthews, and S. R. Qiu, "Dynamics of Secondary Contamination from the Interaction of High-Power Laser Pulses with Metal Particles Attached on the Input Surface of Optical Components," Opt. Express **27**, 23,515 (2019).

C. Dorrer, "Spatiotemporal Metrology of Broadband Optical Pulses," IEEE J. Sel. Top. Quantum Electron. **25**, 3100216 (2019).

G. Duchateau, S. X. Hu, A. Pineau, A. Kar, B. Chimier, A. Casner, V. Tikhonchuk, V. N. Goncharov, P. B. Radha, and E. M. Campbell, "Modeling the Solid-to-Plasma Transition for Laser Imprinting in Direct-Drive Inertial Confinement Fusion," Phys. Rev. E **100**, 033201 (2019).

T. Filkins and J. Katz, "Design of a Free-Space Image-Relay Optical Time Domain Reflectometer to Measure Fiber-Optic Time Delays at Inertial Confinement Fusion Relevant Wavelengths," Proc. SPIE **11114**, 1111417 (2019).

C. J. Forrest, A. Deltuva, W. U. Schröder, A. V. Voinov, J. P. Knauer, E. M. Campbell, G. W. Collins, V. Yu. Glebov, O. M. Mannion, Z. L. Mohamed, P. B. Radha, S. P. Regan, T. C. Sangster, and C. Stoeckl, "Deuteron Breakup Induced by 14-MeV Neutrons from Inertial Confinement Fusion," Phys. Rev. C **100**, 034001 (2019).

L. Guazzotto and R. Betti, "Two-Fluid Burning-Plasma Analysis for Magnetic Confinement Fusion Devices," Plasma Phys. Control. Fusion **61**, 085028 (2019).

A. J. Howard, D. Turnbull, A. S. Davies, P. Franke, D. H. Froula, and J. P. Palastro, "Photon Acceleration in a Flying Focus," Phys. Rev. Lett. **123**, 124801 (2019).

I. V. Igumenshchev, A. L. Velikovich, V. N. Goncharov, R. Betti, E. M. Campbell, J. P. Knauer, S. P. Regan, A. J. Schmitt, R. C. Shah, and A. Shvydky, "Rarefaction Flows and Mitigation of Imprint in Direct-Drive Implosions," Phys. Rev. Lett. **123**, 065001 (2019).

J. L. Kline, S. H. Batha, L. R. Benedetti, D. Bennett, S. Bhandarkar, L. F. Berzak Hopkins, J. Biener, M. M. Biener, R. Bionta, E. Bond, D. Bradley, T. Braun, D. A. Callahan, J. Caggiano, C. Cerjan, B. Cagadas, D. Clark, C. Castro, E. L. Dewald, T. Döppner, L. Divol, R. Dylla-Spears, M. Eckart, D. Edgell, M. Farrell, J. Field, D. N. Fittinghoff, M. Gatu Johnson, G. Grim, S. Haan, B. M. Haines, A. V. Hamza, E. P. Hartouni, R. Hatarik, K. Henderson, H. W. Herrmann, D. Hinkel, D. Ho, M. Hohenberger, D. Hoover, H. Huang, M. L. Hoppe, O. A. Hurricane, N. Izumi, S. Johnson, O. S. Jones, S. Khan, B. J. Kozioziemski, C. Kong, J. Kroll, G. A. Kyrala, S. LePape, T. Ma, A. J. Mackinnon, A. G. MacPhee, S. MacLaren, L. Masse, J. McNaney, N. B. Meezan, J. F. Merrill, J. L. Milovich, J. Moody, A. Nikroo, A. Pak, P. Patel, L. Peterson, E. Piceno, L. Pickworth, J. E. Ralph, N. Rice, H. F. Robey, J. S. Ross, J. R. Rygg, M. R. Sacks, J. Salmonson, D. Sayre, J. D. Sater, M. Schneider, M. Schoff, S. Sepke, R. Seugling, V. Smalyuk, B. Spears, M. Stadermann, W. Stoeffl, D. J. Strozzi, R. Tipton, C. Thomas, R. P. J. Town, P. L. Volegov, C. Walters, M. Wang, C. Wilde, E. Woerner, C. Yeamans, S. A. Yi, B. Yoxall, A. B. Zylstra, J. Kilkenny, O. L. Landen, W. Hsing, and M. J. Edwards, "Progress of Indirect Drive Inertial Confinement Fusion in the United States," Nucl. Fusion **59**, 112018 (2019).

N. Lemos, P. King, J. L. Shaw, A. L. Milder, K. A. Marsh, A. Pak, B. B. Pollock, C. Goyon, W. Schumaker, A. M. Saunders, D. Papp, R. Polanek, J. E. Ralph, J. Park, R. Tommasini, G. J. Williams, H. Chen, F. V. Hartemann, S. Q. Wu, S. H. Glenzer, B. M. Hegelich, J. Moody, P. Michel, C. Joshi, and F. Albert, "X-Ray Sources Using a Picosecond Laser Driven Plasma Accelerator," Phys. Plasmas **26**, 083110 (2019).

C. K. Li, V. T. Tikhonchuk, Q. Moreno, H. Sio, E. D'Humières, X. Ribeyre, Ph. Korneev, S. Atzeni, R. Betti, A. Birkel, E. M. Campbell, R. K. Follett, J. A. Frenje, S. X. Hu, M. Koenig, Y. Sakawa, T. C. Sangster, F. H. Seguin, H. Takabe, S. Zhang, and R. D. Petrasso, "Collisionless Shocks Driven by Supersonic Plasma Flows with Self-Generated Magnetic Fields," Phys. Rev. Lett. **123**, 055002 (2019).

C. Mailliet, E. Le Bel, L. Ceurvorst, S. F. Khan, D. Martinez, Th. Goudal, N. Izumi, D. Kalantar, P. Di Nicola, J. M. Di Nicola, I. Igumenshchev, V. T. Tikhonchuk, B. Remington, V. A. Smalyuk, L. Masse, and A. Casner, "Long-Duration Direct Drive Hydrodynamics Experiments on the National Ignition Facility: Platform Development and Numerical Modeling with CHIC," Phys. Plasmas **26**, 082703 (2019).

C. A. McCoy, M. C. Marshall, D. N. Polsin, D. E. Fratanduono, P. M. Celliers, D. D. Meyerhofer, and T. R. Boehly, "Hugoniot, Sound Velocity, and Shock Temperature of MgO to 2300 GPa," Phys. Rev. B **100**, 014106 (2019).

S. C. Miller, J. P. Knauer, C. J. Forrest, V. Yu. Glebov, P. B. Radha, and V. N. Goncharov, "Fuel-Shell Interface Instability Growth Effects on the Performance of Room Temperature Direct-Drive Implosions," Phys. Plasmas **26**, 082701 (2019).

B. W. Plansinis, W. R. Donaldson, and G. P. Agrawal, "A Time-to-Frequency Converter for Measuring the Shape of Short Optical Pulses," Rev. Sci. Instrum. **90**, 083106 (2019).

B. S. Rice, J. Ulreich, and M. J. Shoup III, "Prediction of Deuterium–Tritium Ice-Layer Uniformity in Direct-Drive Confinement Fusion Target Capsules," in *Proceedings of NAFEMS World Congress 2019* (NAFEMS, Glasgow, Scotland 2019).

E. Ruskov, V. Yu. Glebov, T. W. Darling, F. J. Wessel, F. Conti, J. C. Valenzuela, H. U. Rahman, and F. N. Beg, "Gated Liquid Scintillator Detector for Neutron Time of Flight Measurements in a Gas-Puff Z-Pinch Experiment," Rev. Sci. Instrum. **90**, 073505 (2019).

R. V. Shapovalov, G. Brent, R. Moshier, M. Shoup, R. B. Spielman, and P.-A. Gourdain, "Design of 30-T Pulsed Magnetic Field Generator for Magnetized High-Energy-Density Plasma Experiments," Phys. Rev. Accel. Beams **22**, 080401 (2019).

H. Sio, O. Larroche, S. Atzeni, N. V. Kabadi, J. A. Frenje, M. Gatu Johnson, C. Stoeckl, C. Li, C. J. Forrest, V. Glebov, P. J. Adrian, A. Bose, A. Birkel, S. P. Regan, F. H. Séguin, and R. D. Petrasso, "Probing Ion Species Separation and Ion Thermal Decoupling in Shock-Driven Implosions Using Multiple Nuclear Reaction Histories," Phys. Plasmas **26**, 072703 (2019).

H. Sio, C. Li, C. E. Parker, B. Lahmann, A. Le, S. Atzeni, and R. D. Petrasso, "Fuel-Ion Diffusion in Shock-Driven Inertial Confinement Fusion Implosions," Matter Radiat. Extremes **4**, 055401 (2019).

C. Stoeckl, C. J. Forrest, V. Yu. Glebov, S. P. Regan, T. C. Sangster, W. U. Schröder, A. Schwemmlein, and W. Theobald, "A Platform for Nuclear Physics Experiments with Laser-Accelerated Light Ions," Nucl. Instrum. Methods Phys. Res. B **453**, 41 (2019).

M. Stoeckl and A. A. Solodov, "Refining Instrument Response Functions with 3-D Monte Carlo Simulations of Differential Hard X-Ray Spectrometers," Nucl. Instrum. Methods Phys. Res. A **931**, 162 (2019).

J. Strehlow, P. Forestier-Colleoni, C. McGuffey, M. Bailly-Grandvaux, T. S. Daykin, E. McCary, J. Peebles, G. Revet,

S. Zhang, T. Ditmire, M. Donovan, G. Dyer, J. Fuchs, E. W. Gaul, D. P. Higginson, G. E. Kemp, M. Martinez, H. S. McLean, M. Spinks, H. Sawada, and F. N. Beg, "The Response Function of Fujifilm BAS-TR Imaging Plates to Laser-Accelerated Titanium Ions," Rev. Sci. Instrum. **90**, 083302 (2019).

Forthcoming Publications

A. S. Davies, D. Haberberger, J. Katz, S. Bucht, J. P. Palastro, R. K. Follett, and D. H. Froula, "Investigation of Picosecond Thermodynamics in a Laser-Produced Plasma Using Thomson Scattering," to be published in Plasma Physics and Controlled Fusion.

C. Fagan, M. Sharpe, W. T. Shmayda, and W. U. Schröder, "Thin-Alumina Film as a Tritium Adsorption Inhibitor for Stainless-Steel 316," to be published in Fusion Science and Technology.

C. Fagan, M. Sharpe, W. T. Shmayda, and W. U. Schröder, "Tritium Retention in Hexavalent Chromate-Conversion–Coated Aluminum Alloy," to be published in Fusion Science and Technology.

S. R. Fairchild, Y. Liu, J. Palastro, and J. Peñano, "Laser Filamentation and Applications: Introduction," to be published in the Journal of the Optical Society of America B.

P. Franke, D. Turnbull, J. Katz, J. P. Palastro, I. A. Begishev, J. Bromage, J. L. Shaw, R. Boni, and D. H. Froula, "Measurement and Control of Large Diameter Ionization Waves of Arbitrary Velocity," to be published in Optics Express.

D. Haberberger, A. Shvydky, J. P. Knauer, S. X. Hu, S. T. Ivancic, J. Carroll-Nellenback, D. Cao, V. V. Karasiev, A. V. Maximov, V. N. Goncharov, and D. H. Froula, "Density Measurements of the Inner Shell Release," to be published in Physical Review Letters.

A. M. Hansen, D. Turnbull, J. Katz, and D. H. Froula, "Mitigation of Self-Focusing in Thomson Scattering Experiments," to be published in Physics of Plasmas.

S. X. Hu, R. Epstein, W. Theobald, H. Xu, H. Huang, V. N. Goncharov, S. P. Regan, P. W. McKenty, R. Betti, E. M. Campbell, and D. S. Montgomery, "Direct-Drive Double-Shell Implosion: A Platform for Burning-Plasma Physics Studies," to be published in Physical Review E.

T. Z. Kosc, A. A. Kozlov, S. Papernov, K. R. P. Kafka, K. L. Marshall, and S. G. Demos, "Investigation of Parameters Governing Damage Resistance of Nematic Liquid Crystals for High-Power or Peak-Intensity Laser Applications," to be published in Scientific Reports.

J. F. Myatt, J. G. Shaw, R. K. Follett, D. H. Edgell, D. H. Froula, and V. N. Goncharov, "*LPSE*: A 3-D Wave-Based Model of Cross-Beam Energy Transfer in Laser-Irradiated Plasmas," to be published in the Journal of Computational Physics.

J. M. Ngoko Djiokap, A. V. Meremianin, N. L. Manakov, L. B. Madsen, S. X. Hu, and A. F. Starace, "Molecular Symmetry-Mixed Dichroism in Double Photoionization of H_2," to be published in Physical Review Letters.

C. E. Parker, J. A. Frenje, O. H. W. Siegmund, C. J. Forrest, V. Yu. Glebov, J. D. Kendrick, C. W. Wink, M. Gatu Johnson, T. J. Hilsabeck, S. T. Ivancic, J. Katz, J. D. Kilkenny, B. Lahmann, C. K. Li, F. H. Séguin, C. M. Sorce, C. Trosseille, and R. D. Petrasso, "Response of a Lead-Free Borosilicate-Glass Microchannel Plate to 14-MeV Neutrons and γ Rays," to be published in Review of Scientific Instruments.

R. Paul, S. X. Hu, and V. V. Karasiev, "Crystalline Phase Transitions and Vibrational Spectra of Silicon up to Multiterapascal Pressures," to be published in Physical Review B.

E. M. Schiesser, S.-W. Bahk, J. Bromage, and J. P. Rolland "Design and Alignment of an All-Spherical Unobscured Four-Mirror Image Relay for an Ultra-Broadband Subpetawatt Laser," to be published in Applied Optics.

M. Sharpe, C. Fagan, and W. T. Shmayda, "Distribution of Tritium in the Near Surface of Type 316 Stainless Steel," to be published in Fusion Science and Technology.

W. T. Shmayda, C. R. Shmayda, and J. Torres, "Tritium Extraction from Water," to be published in Fusion Science and Technology.

R. Sobolewski, "Optical Detectors and Sensors," to be published in the *Handbook of Superconducting Materials*.

D. Turnbull, A. Colaïtis, A. M. Hansen, A. L. Milder, J. P. Palastro, J. Katz, C. Dorrer, B. E. Kruschwitz, D. J. Strozzi, and

D. H. Froula, "Impact of the Langdon Effect on Cross-Beam Energy Transfer," to be published in Nature Physics.

H. Wen, A. V. Maximov, R. Yan, J. Li, C. Ren, and F. S. Tsung, "Three-Dimensional Particle-in-Cell Modeling of Parametric Instabilities Near the Quarter-Critical Density in Plasmas," to be published in Physical Review E.

Conference Presentations

V. N. Goncharov, "High-Energy-Density Physics Research at the Laboratory for Laser Energetics," presented at JOWOG 37, Aldermaston, UK, 8–11 July 2019.

———

A. S. Davies, J. Katz, S. Bucht, D. Haberberger, J. P. Palastro, J. L. Shaw, D. Turnbull, R. Boni, I. A. Begishev, S.-W. Bahk, J. Bromage, A. Sorce, J. Konzel, B. Cuffney, J. D. Zuegel, D. H. Froula, W. Rozmus, J. D. Sadler, R. Trines, R. Bingham, and P. A. Norreys, "Investigation of Electron Plasma Waves and Picosecond Thermodynamics in a Laser-Produced Plasma Using Thomson Scattering," presented at the 46th European Physical Society Conference on Plasma Physics, Milan, Italy, 8–12 July 2019.

———

D. H. Froula, "Lessons from Glenzer: Measuring Electron Distribution Functions with Thomson Scattering," presented at the Workshop on High-Energy-Density Physics, Rostock, Germany, 12 July 2019.

———

M. S. Wei, H. G. Rinderknecht, J. D. Zuegel, J. Bromage, P. M. Nilson, S. X. Hu, D. H. Froula, F. Albert, B. M. Hegelich, M. Roth, and E. M. Campbell, "Frontiers in High-Energy-Density and Relativistic Plasma Physics Enabled by EP-OPAL: A Multibeam Ultrahigh-Intensity Laser User Facility," presented at the First Community Workshop for High Energy, College Park, MD, 16–17 July 2019.

———

H. G. Rinderknecht, J. D. Zuegel, J. Bromage, M. S. Wei, P. M. Nilson, S. X. Hu, D. H. Froula, F. Albert, B. M. Hegelich, M. Roth, and E. M. Campbell, "Frontiers in High-Energy-Density and Relativistic Plasma Physics Enabled by EP-OPAL: A Multibeam Ultrahigh-Intensity Laser User Facility," presented at the Discovery Plasma Science Community Planning Workshop, Madison, WI, 23–25 July 2019.

———

The following presentations were made at High-Energy-Density Science Summer School, La Jolla, CA, 28 July–10 August 2019:

A. Kish and A. B. Sefkow, "Preliminary Work Toward an Investigation of Burn-Wave Propagation in Magnetized Cylindrical Targets."

T. T. Simpson, D. H. Froula, J. Vieira, and J. P. Palastro, "Nonlinear Self-Focusing of Flying Focus Pulses."

J. Wilson, V. N. Goncharov, C. Dorrer, A. Shvydky, and J. P. Palastro, "Broadband Smoothing of Laser Pulses for Imprint Reduction in Direct-Drive Inertial Confinement Fusion."

———

M. S. Wei, "LaserNetUS–OMEGA EP Laser System and Experimental Capability," presented at LaserNetUS, Virtual Meeting, 29 July 2019.

———

G. W. Collins, "Extreme Matters: Pressure to Explore Planets and Revolutionary Materials," presented at the 27th Interna-

tional Conference on High Pressure Science and Technology (AIRAPT27), Rio de Janeiro, Brazil, 4–9 August 2019.

———————

L. S. Leal, A. V. Maximov, R. Betti, A. B. Sefkow, and V. Ivanov, "*HYDRA* Modeling of Laser-Ablated Plasma in Megagauss Magnetic Fields," presented at the Tenth Workshop on Fundamental Science with Pulsed Power and User Meeting, Albuquerque, NM, 11–14 August 2019.

———————

R. B. Spielman and E. M. Campbell, "OMEGA-Z: A 15-TW Pulsed-Power Facility for High-Energy-Density Physics," presented at the Z Fundamental Science Program Workshop, Albuquerque, NM, 11–14 August 2019.

———————

T. Filkins, J. Katz, and S. T. Ivancic, "Design of an Image-Relay Optical Time-Domain Reflectometer to Measure Fiber-Optic Time Delays at Inertial Confinement Fusion Relevant Wavelengths," presented at SPIE Optical Engineering and Applications, San Diego, CA, 11–15 August 2019.

———————

K. L. Marshall, D. J. Batesky, J. U. Wallace, L. Garrett, T. Z. Kosc, S. Papernov, B. N. Hoffman, and J. Shojaie, "UV-Transmissive Glassy Liquid Crystals Employing Chiral Synthons Based on Natural Products," presented at SPIE Optics and Photonics, Liquid Crystals XXIII, San Diego, CA, 11–15 August 2019 (invited).

———————

The following presentations were made at the International Workshop on Optical Thomson Scattering, Rochester, NY, 13–14 August 2019:

A. S. Davies, J. Katz, S. Bucht, D. Haberberger, J. P. Palastro, J. L. Shaw, D. Turnbull, R. Boni, I. A. Begishev, S.-W. Bahk, J. Bromage, A. Sorce, J. Konzel, R. Cuffney, J. D. Zuegel, D. H. Froula, and W. Rozmus, "Investigation of Electron Plasma Waves and Picosecond Thermodynamics in a Laser-Produced Plasma Using Thomson Scattering."

R. K. Follett, J. A. Delettrez, D. H. Edgell, R. J. Henchen, J. Katz, J. F. Myatt, and D. H. Froula, "Subtleties to Fitting Thomson-Scattering Spectra."

A. M. Hansen, D. Turnbull, J. Katz, A. L. Milder, J. P. Palastro, D. Mastrosimone, and D. H. Froula, "Phase Plates in Thomson-Scattering Experiments."

J. Katz, "Lessons Learned from the Implementation and Operation of the OMEGA Thomson Scattering System."

A. L. Milder, J. Katz, R. Boni, D. Nelson, J. P. Palastro, K. Daub, R. K. Follett, and D. H. Froula, "Measurements of Arbitrary Distribution Functions Using Angularly Resolved Thomson Scattering."

H. G. Rinderknecht, H. S. Park, J. S. Ross, P. A. Amendt, D. P. Higginson, S. C. Wilks, R. K. Follett, D. Haberberger, J. Katz, D. H. Froula, N. M. Hoffman, G. Kagan, B. Keenan, A. Simakov, L. Chacon, and E. Vold, "Imaging Thomson Scattering: Measuring Plasma Conditions in a Strong Shock."

———————

H. G. Rinderknecht, D. H. Froula, S. X. Hu, P. M. Nilson, and J. D. Zuegel, "Frontiers in Physics Enabled by EP-OPAL: A Multibeam Ultra-Intense Laser User Facility," presented at ExHILP 2019, Stanford, CA, 3–6 September 2019.

———————

J. D. Zuegel, "The Brightest Light Initiative (BLI): A Path Forward for Ultra-Intense Ultrafast Lasers in the U.S.," presented at Frontiers in Optics, Washington, DC, 15–19 September 2019.

———————

The following presentations were made at the 41st Tritium Focus Group Meeting, Augusta, GA, 17–19 September 2019:

D. Bassler, "Making an Optimal Hafnium Oxide Film as a Hydrogen Diffusion Barrier."

C. Fagan, M. Sharpe, W. T. Shmayda, and W. U. Schröder, "Distribution of Tritium in the Near Surface of 316 Stainless Steel."

M. Sharpe and W. T. Shmayda, "Measurement of Palladium Hydride Isotherms Between 130 K and 393 K Using Pure H_2, Pure D_2, and HD Mixtures."

———————

The following presentations were made at the U.S.–Japan Workshop on Theory and Simulations of High Energy Density Physics with Extreme Fields, Osaka, Japan, 21–22 September 2019:

D. H. Froula, S.-W. Bahk, I. A. Begishev, R. Boni, J. Bromage, A. Davies, R. K. Follett, D. Haberberger, A. Howard, G. Jenkins, J. Katz, T. J. Kessler, L. Nguyen, J. P. Palastro, D. Ramsey, J. L. Shaw, D. Turnbull, N. Vafaei-Najafabadi, J. Vieira, and F. Quéré, "Flying Focus: Spatiotemporal Control of Intensity for Laser-Based Applications."

H. G. Rinderknecht, M. S. Wei, J. P. Palastro, G. Bruhaug, A. Arefiev, T. Wang, T. Toncian, H. J. Quevedo, T. Ditmire, and J. Williams, "Megatesla Magnetic Fields and Efficient Gamma-Ray Generation Using Microstructured Targets: Preparations for Experiments at TPW."

———————

The following presentations were made at Laser Damage 2019, Boulder, CO, 22–25 September 2019:

B. N. Hoffman, A. A. Kozlov, J. B. Oliver, T. J. Kessler, A. L. Rigatti, S. G. Demos, A. Shestopalov, and N. Liu, "Damage Morphology and Damage-Initiation Mechanisms in Multilayer Dielectric Gratings at Different Pulse Durations."

K. R. P. Kafka, S. G. Demos, and B. N. Hoffman, "Short-Pulse Laser Irradiation of Microparticle Contamination on Reflective Optics."

A. A. Kozlov, D. Canning, B. N. Hoffman, B. E. Kruschwitz, A. L. Rigatti, and L. J. Waxer, "Review of Decade-Long Monitoring Damage Resistance of Multilayer Dielectric Gratings Inside the Vacuum Compressor Chamber on OMEGA EP."

L. Lamaignère, A. Ollé, M. Chorel, N. Roquin, A. A. Kozlov, B. N. Hoffman, J. B. Oliver, L. Gallais, and S. G. Demos, A. Melninkaitis, "Round-Robin Measurements of Optical Monolayer Laser-Induced–Damage Threshold in the Subpicosecond Range."

J. B. Oliver, "Coatings for Large-Aperture Laser Systems."

A. A. Shestopalov, N. Liu, B. N. Hoffman, A. A. Kozlov, and S. G. Demos, "Chemical Composition, Structure Morphology, Contaminant Cleaning and Laser-Induced–Damage Threshold in Coarse Fused-Silica Gratings."

J. U. Wallace, K. L. Marshall, T. Z. Kosc, D. J. Batesky, B. N. Hoffman, S. Papernov, L. Garrett, J. Shojaie, and S. G. Demos, "Laser-Induced–Damage Behavior of Novel Glassy Liquid Crystal Materials at 1 ns and Multiple Wavelengths."

———————

A. Milder, J. Katz, R. Boni, D. Nelson, J. P. Palastro, A. M. Hansen, D. Turnbull, P. Franke, S. T. Ivancic, J. L. Shaw, K. Daub, R. K. Follett, D. H. Froula, H. Le, M. Sherlock, and W. Rozmus, "Novel Techniques and Uses of Collective Thomson Scattering," presented at Laser Aided Plasma Diagnostics 2019, Whitefish, MT, 22–26 September 2019.

———————

The following presentations were made at 11th International Conference on Inertial Fusion Science and Applications, Osaka, Japan, 22–27 September 2019:

A. R. Christopherson, R. Betti, S. Miller, V. Gopalaswamy, D. Cao, and O. M. Mannion, "Theory of Ignition and Burn Propagation in Inertially Confined Plasmas."

D. H. Froula, C. Dorrer, E. M. Hill, J. Bromage, T. J. Kessler, J. D. Zuegel, R. K. Follett, L. Nguyen, A. A. Solodov, J. P. Palastro, D. Turnbull, D. H. Edgell, J. G. Shaw, A. M. Hansen, A. L. Milder, J. Katz, R. Boni, V. N. Goncharov, M. Sherlock, H. Le, D. J. Strozzi, P. Michel, L. Divol, J. F. Myatt, W. Rozmus, J. Bates, A. Schmitt, J. Weaver, A. Colaïtis, L. Yin, and B. Albright, "A Path to an Expanded Inertial Confinement Fusion Design Space Through a Better Understanding and Mitigation of Laser–Plasma Instabilities."

F. García Rubio, R. Betti, and H. Aluie, "The Effect of Self-Generated Magnetic Fields on the Ablative Rayleigh–Taylor Instability Dynamics."

V. N. Goncharov, "Progress Toward the Demonstration of Burning Plasma in the U.S. Inertial Confinement Fusion Program."

V. Gopalaswamy, R. Betti, J. P. Knauer, A. Lees, D. Patel, A. R. Christopherson, K. M. Woo, O. M. Mannion, Z. L. Mohammed, F. J. Marshall, C. Stoeckl, V. Yu. Glebov, S. P. Regan, R. C. Shah, D. H. Edgell, D. Cao, V. N. Goncharov, I. V. Igumenshchev, P. B. Radha, T. J. B. Collins, T. C. Sangster, E. M. Campbell, M. Gatu Johnson, R. D. Petrasso, C. K. Li, and J. A. Frenje, "Statistically Guided Design of Direct-Drive Inertial Confinement Fusion Experiments."

S. X. Hu, R. Epstein, W. Theobald, V. N. Goncharov, S. P. Regan, P. W. McKenty, R. Betti, E. M. Campbell, H. Xu, H. Huang, and D. S. Montgomery, "Direct-Drive Double-Shell (D^{3}S) Implosion: A Platform for Burning-Plasma Studies."

P. B. Radha, M. J. Rosenberg, A. Shvydky, A. A. Solodov, R. Betti, E. M. Campbell, T. J. B. Collins, R. S. Craxton, V. N. Goncharov, J. A. Marozas, F. J. Marshall, S. P. Regan, T. C. Sangster, and D. Turnbull, "Direct-Drive Physics at the National Ignition Facility."

S. P. Regan, V. N. Goncharov, T. C. Sangster, R. Betti, E. M. Campbell, K. A. Bauer, T. R. Boehly, M. J. Bonino, D. Cao, A. R. Christopherson, G. W. Collins, T. J. B. Collins, R. S. Craxton, D. H. Edgell, R. Epstein, C. J. Forrest, R. K. Follett, D. H. Froula, V. Yu. Glebov, V. Gopalaswamy, D. R. Harding, S. X. Hu, I. V. Igumenshchev, S. T. Ivancic, D. W. Jacobs-Perkins, R. T. Janezic, J. H. Kelly, T. J. Kessler, J. P. Knauer, T. Z. Kosc, O. M. Mannion, J. A. Marozas, F. J. Marshall, P. W. McKenty, Z. L. Mohamed, S. F. B. Morse, P. M. Nilson, J. P. Palastro, D. Patel, J. L. Peebles, P. B. Radha, H. G. Rinderknecht, M. J. Rosenberg, S. Sampat, W. Seka, R. C. Shah, J. R. Rygg, J. G. Shaw, W. T. Shmayda, M. J. Shoup III, A. Shvydky, A. A. Solodov, C. Sorce, C. Stoeckl, W. Theobald, D. Turnbull, J. Ulreich, M. D. Wittman, K. M. Woo, J. D. Zuegel, J. A.

Frenje, M. Gatu Johnson, R. D. Petrasso, M. Karasik, S. P. Obenschain, A. J. Schmitt, T. J. Hilsabeck, K. Englehorn, J. D. Kilkenny, J. D. Hares, A. K. L. Dymoke-Bradshaw, P. Bell, A. Carpenter, D. K. Bradley, S. Nagel, G. Rochau, and L. Claus, "Multidimensional Effects on Hot-Spot Formation in OMEGA DT Cryogenic Implosions."

H. Rinderknecht, C. J. Forrest, J. P. Knauer, W. Theobald, S. P. Regan, R. Simpson, and J. A. Frenje, "Knock-On Deuteron Imaging to Diagnose Hot-Spot Fuel and ρR Symmetry in Directly Driven Inertial Confinement Fusion Implosions."

M. Zaghoo, T. R. Boehly, J. R. Rygg, P. M. Celliers, S. X. Hu, and G. W. Collins, "Breakdown of Fermi Degeneracy in Shocked Deuterium."

––––––––––

J. D. Zuegel, "Laboratory for Laser Energetics," presented at the Visit of the Honorable Carl Heastie, Speaker of the NYS Assembly, Rochester, NY, 23 September 2019.

––––––––––

M. S. Wei, "Opportunities for U.S.–ELI Collaborations: Laboratory for Laser Energetics Perspective," presented at the U.S.–ELI Joint Workshop, Washington, DC, 25 September 2019.

––––––––––

R. Betti, "Status and Prospects for Nuclear Fusion with Lasers," presented at FisMat 2019, Catania, Italy, 30 September–4 October 2019 (invited).